Luís Filipe da Silva Ribeiro

Segmentation of Aberrant Crypt Foci using Computational Vision

Master Thesis

Master in Biomedical Engineering
Faculty of Engineering, University of Oporto

Oporto, October 21, 2013

Segmentation of Aberrant Crypt Foci using Computational Vision

Dissertation submitted to obtain the Master's degree in Biomedical Engineering

Author: Luís Filipe da Silva Ribeiro

meb11006@fe.up.pt
BSc in Medical Computation and Instrumentation Engineering
Polytechnic Institute of Porto (2011)

Tutor: João Manuel RS Tavares

tavares@fe.up.pt
Associate Professor of the Mechanical Engineering Department
Faculty of Engineering, University of Oporto

Master in Biomedical Engineering
Faculty of Engineering, University of Oporto

Oporto, October 21, 2013

"Be who you are and say what you feel,
because those who mind don't matter
and those who matter don't mind"

-Dr. Seuss

Acknowledgments

I greatly acknowledge Professor João Manuel R.S. Tavares for the support granted to this work. His patience and accurate insights helped me become more technical in the academic field.

I also would like to thank the Engineering Faculty of Oporto University for the the opportunity to demonstrate my strengths, competencies and prove myself worthy in achieving a Master's degree.

I have a debt of gratitude to all my friends, who always believed in me and in my abilities, without them this would be a lot harder.

Last but not least, to my family and girlfriend, thank you for everything you have done for me, the unconditional support given throughout my life and for shaping me into the person I am today.

To all, my most sincere appreciation.

Abstract

Colorectal cancer is a type of cancer that develops in the large intestine (colon) or the rectum. As it affects both these areas it called colorectal cancer, one of the most common malignancies in the world. In Portugal, colorectal cancer ranks first in terms of mortality among the five most predominant types of cancer (lung, breast, colorectal, stomach and prostate). However, contrary to what happens with other diseases, colorectal cancer can be avoided.

In this context, the aberrant crypt foci may have a crucial and decisive role. The aberrant crypt foci are groups of crypts (small wells in the epithelium of the colon) aberrant (not normal), which are supposed to be the precursors of colorectal cancer. In fact, according to endoscopic studies and animal experiments, aberrant crypt foci precede the onset of adenomas. Thus, if proven, this means that aberrant crypt foci may have to be considered as part of the adenoma-carcinoma sequence.

This dissertation aims to study and develop computational methodologies that allow the detection and segmentation of aberrant crypt foci in endoscopy images.

Keywords

Aberrant Crypt Foci, Deformable Models, Image Segmentation, Level Sets, Medical Imaging.

Resumo

O cancro colo-retal é um tipo de cancro que se desenvolve no intestino grosso (colón) ou no reto (extremidade do reto). Como afeta simultaneamente estas áreas é designado por cancro colo-retal, sendo um dos tumores malignos mais frequentes no mundo. Em Portugal, o cancro colo-retal está em primeiro lugar em termos de mortalidade entre os cinco tipos mais importantes de cancro (pulmão, mama, colo-retal, estômago e próstata). Contudo, ao contrário do que acontece com outras doenças, é possível evitar o cancro colo-retal.

Neste contexto, os focos de criptas aberrantes podem ter um papel crucial e determinante. Os focos de criptas aberrantes são grupos de criptas (pequenos poços, no epitélio do colón) aberrantes (não normais), que se supõem serem os percursores do cancro colo-retal. De fato, de acordo com estudos endoscópicos e experiencias animais, os focos de criptas aberrantes precedem a eclosão dos adenomas. Assim, se este facto for comprovado, isto significa que os focos de criptas aberrantes terão que ser considerados parte da sequência adenoma-carcinoma.

Com esta dissertação pretende-se estudar e desenvolver metodologias computacionais que permitam a deteção e segmentação de focos de criptas aberrantes em imagens de endoscopia.

Palavras-chave

Focos de Criptas Aberrantes, Imagem Médica, Segmentação de Imagem, Modelos Deformáveis, *Level Sets*.

Contents

List of Figures

List of Tables

Abbreviations

ACF	Aberrant Crypt Foci
ACWE	Active Contours Without Edges
CT	Computerized Tomography
DNA	Deoxyribonucleic Acid
FIT	Fecal Immunological Test
gFOBT	Guaiac Fecal-Occult Blood Test
GUI	Graphical User Interface
HSV	Hue, Saturation and Value
PDE	Partial Differential Equations
RGB	Red, Blue and Green
ROI	Region of Interest

Chapter 1

Introduction

1.1 Background

Colorectal cancer is one of the most frequent types of malignancies in the world and one of the leading causes of death. Unlike other tumors, it is possible to prevent colorectal cancer. This is due to the long time that elapses between the appearance of adenomas (benign epithelial tumor) until its evolution to carcinoma, allowing benign lesions to be identified and removed Figueiredo et al. (2008).

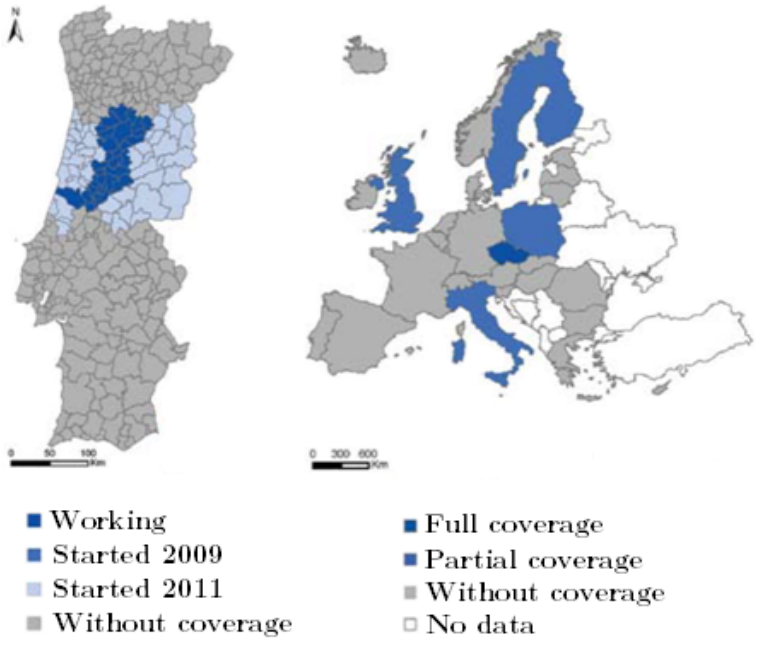

Fig. 1.1: Colorectal cancer screening programs in Portugal and Europe (adapted from Couceiro et al. (2009)).

At an European level there have been taken measures to maintain the fight against cancer in the health policy agenda. Despite advances, cancer remains a major public

challenge. It was diagnosed around 3.2 million people and 1.7 million perished, just in Europe. It is a disease that affects not only patients but also, indirectly, their families and society. This is reflected in the ever-higher spending on public health and that is an area that can not be overlook Gouveia et al. (2008).

In Portugal, colorectal cancer was, in 2005, accounted for 14.6% of all deaths from cancer. Its early detection reduces the incidence, but this requires a wider screening and that represents an investment Pinto et al. (2010).

The national screening program for colorectal cancer has thirty-one health centers in the central region as a pilot. This regional health administration foresees a phased enlargement to the entire region, Fig 1.1. Among European countries, only the Czech Republic has a screening program for colorectal cancer with nationwide coverage Couceiro et al. (2009).

Technological innovation of diagnostic tools will enable faster results, making it possible to perform more tests, wich increases the number of people screened. The early detection reduces mortality rate and will be beneficial at an economic and social plan in the near future.

It is of great interest to research and develop complementary diagnostic techniques, in addition to the current ones, to streamline and standardize processes, for an automatic detection of aberrant crypt foci that could later lead to colorectal cancer. This thesis main objective is the development of some of these processes in form of computational algorithms for segmentation and analysis of medical images.

1.2 Objectives

The main objective is the segmentation of aberrant crypt foci through acquired images of endoscopy techniques using computational vision. However, this work will be facilitated if there is a prior knowledge to physiological level thereof, as well as the anatomy and biology of the large intestine.

To help ongoing research is also a goal of this thesis, although the fundamental role of this thesis is to help those who are affected by colorectal cancer.

1.3 Thesis Organization

The thesis is arranged in five main chapters: the 1.Introduction where the context is explained as well as objectives and motivations. In 2.Aberrant Crypt Foci, all the biology behind the Aberrant Cryp Foci is deconstructed. The chapter 3.Computational Image Processing & Analysis explains procedures and algorithms that will be used further

in 4.Implementations, also introduces and drills from the digital image to segmentation techniques, as well as state-of-the-art algorithms. I discuss the results of the followed approach in 5.Results & Discussion. The last chapter is 6.Conclusion & Future Work, where I put my final Thesis considerations.

1.4 Contributions

The main contributions of this project can be highlighted as:

- Overview the current screening situation of the colorectal cancer, mainly at national and european level.
- The anatomic, physiological and histological study of aberrant crypt foci to a better understanding of the structures to be analyzed and to enhance the physiological relevance of them.
- Comparison of the different diagnostic techniques performed to the detection of aberrant crypt foci and colorectal cancer.
- The study of biomedical imaging enhancement and segmentation was significant to know the wide variety of algorithms that can be used in medical images and to assess the characteristics of each one, as well as the state-of-the-art algorithms used in detection of endoscopic lesions.
- Development of feature extraction algorithms that could be useful to regions of interest or regions that have no relevant data.
- Development of different segmentation techniques and adaptation of commonly used segmentation algorithms in order to meet the aberramt crypt foci specifications. These algorithms can also be adapted to other problems.
- Analyze the evolution that the dataset undergoes from image preprocessing, feature extraction to segmentation and the discussion of this process.

Chapter 2

Aberrant Crypt Foci

2.1 Colorectal Biology

The colon and rectum are part of the human digestive system, Fig. 2.1. This extends from the upper end, the mouth, to the anus. It is responsible for the provision of water, electrolytes and nutrients to the body and is composed of various organs and structures. Understanding its operation, anatomy, physiology and histology, will facilitate the understanding of the mechanisms involved in colorectal cancer and in the detection of aberrant crypt foci.

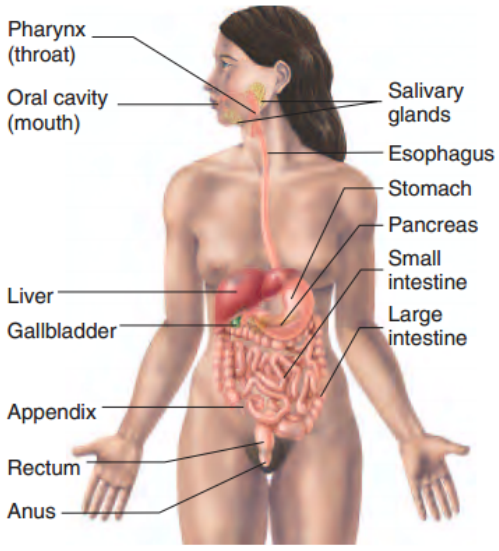

Fig. 2.1: Human digestive system and its organs (adapted from Seeley et al. (2004)).

2.1.1 Anatomy & Physiology

The colon is the portion of the digestive tract which begins at the ileocecal junction and ends in the anus. It comprises the cecum, colon, rectum and anal canal. In the colon, chyme is transformed into feces through water absorption, salts and mucus secretion. The cecum is where the small intestine and the bulk unite at the ileocecal junction and, also, where the appendix can be found Seeley et al. (2004).

Colon measures about 1.5 to 1.8m in length and is divided into four parts: the ascending colon, transverse, descending and sigmoid. The mucosal lining of the colon is composed of cylindrical epithelium that does not form villi as in the small intestine, but has many tubular glands, known as crypts Seeley et al. (2004).

The rectum is a muscular tube that begins at the termination of the sigmoid colon and ends in the anal canal. It is internally lined by epithelium and its simple muscular layer is relatively thick compared to the rest of the digestive tract Seeley et al. (2004).

The anal canal corresponds to the last 2 to 3cm of the gut. The smooth muscle layer is even thicker than the rectum, forming the internal anal sphincter at the top, and terminating the anal canal the external sphincter, which consists of skeletal muscle, Fig. 2.2.

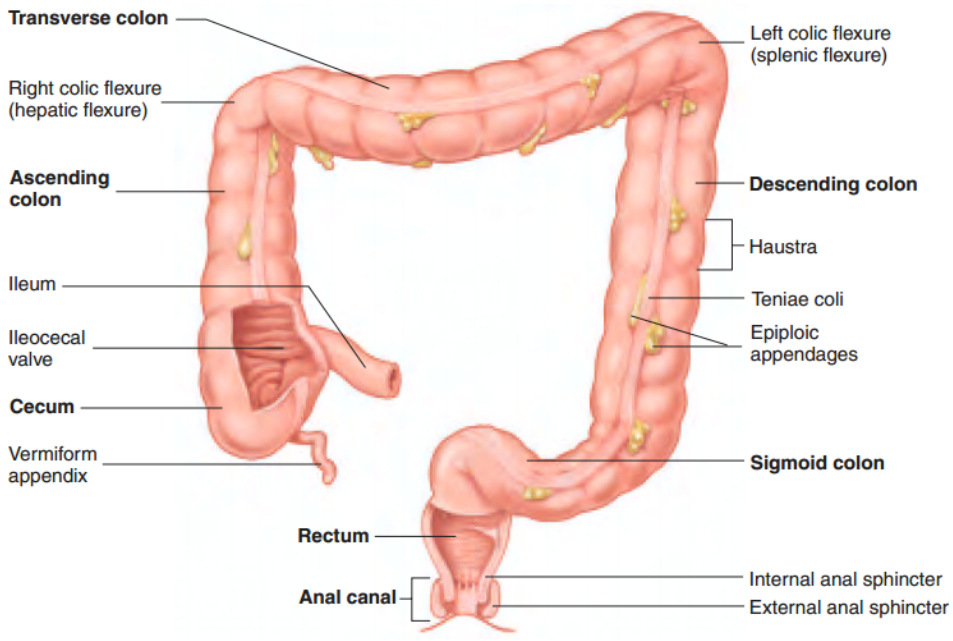

Fig. 2.2: Large intestine and its structures (adapted from Seeley et al. (2004)).

2.1.2 Histology

The main layers of the digestive system present in the intestine, can be seen in Fig. 2.3.

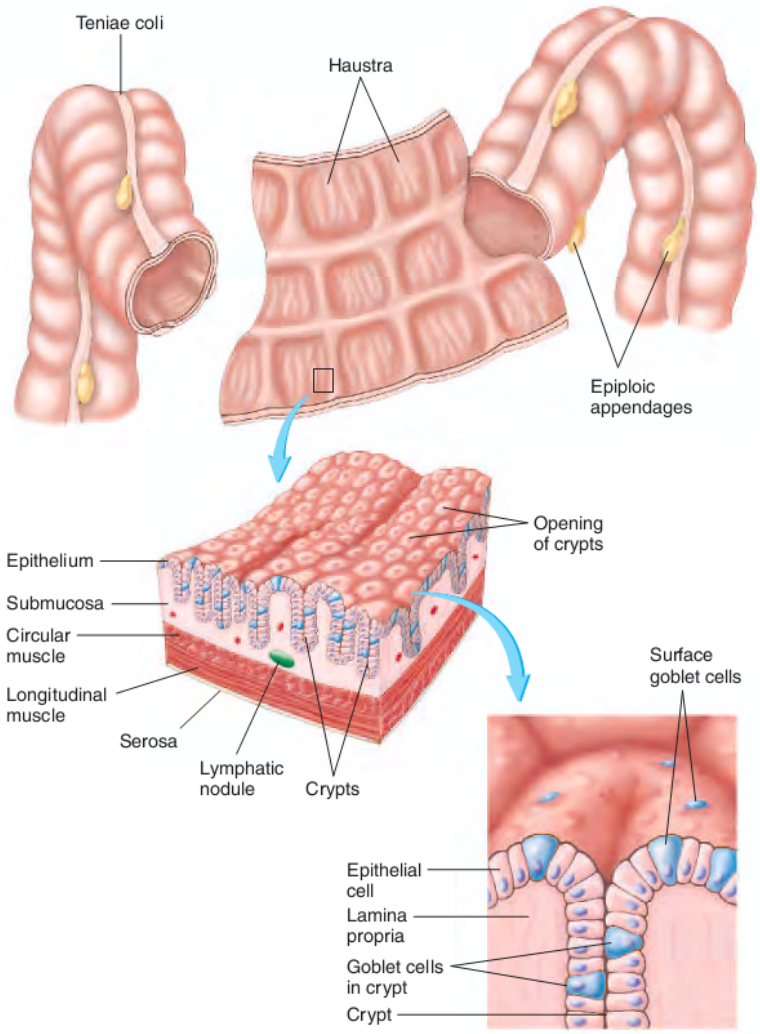

Fig. 2.3: Histology of the large intestine (adapted from Seeley et al. (2004)).

The innermost tunic is the mucosa and is composed of three layers: (1) cylindrical simple mucous epithelium, (2) lamina propria, layer of lax connective tissue and (3) muscularis mucosae, a thin layer of smooth muscle Tortora and Derrickson (2009).

The mucosa contains numerous intestinal glands, straight tubular designated Lieberkühn crypts. Submucosa is composed of a thick layer of connective tissue containing nerves, blood vessels and small glands. Muscular coat is composed of smooth muscle arranged in two layers, an inner circular and outer longitudinal one. The adventitia layer or serosa stems in the structure. Serous when the portions of the digestive tract are directed into the peritoneal cavity, with a simple squamous epithelium and a thin layer of connective tissue. Adventitial when the outermost layer of the gut tissue has its origin in connective tissue Guyton and Hall (2000).

2.2 Colorectal Cancer

There are over a hundred different types of cancer. The cancer affects the basic unit of life, the cell, and occurs when cells grow in an abnormal manner and without any kind of order. Like all organs of the body, the large intestine, which comprises the colon and rectum are composed of various cell types. When the growth is abnormal masses of tissue are formed, called nodules or tumors. Benign tumors are not cancer and can be removed and, in most cases, do not appear again. Malignant tumors, in contrast, can invade and damage tissues of surrounding organs. Cancer cells can enter the bloodstream or lymphatic system and affect distant organs from the primary tumor. This phenomenon is called metastasis. When this happens, the new metastasized tumor is the same kind as the primary cancer cell growth. That is, if a colorectal cancer metastasize to the liver it continues to be designated as colorectal cancer Thorup (1996).

The process of carcinogenesis begins with the proliferation of epithelial cells genetically altered, creating clusters of abnormal cells. The resulting niches are called aberrant crypt foci and represent the initial phase of dysplasia, abnormal cell known as maturation. The continued expansion and proliferation of aberrant crypt foci, Fig 2.4, leads to the appearance of polyps, also called adenomas Makinen (2007).

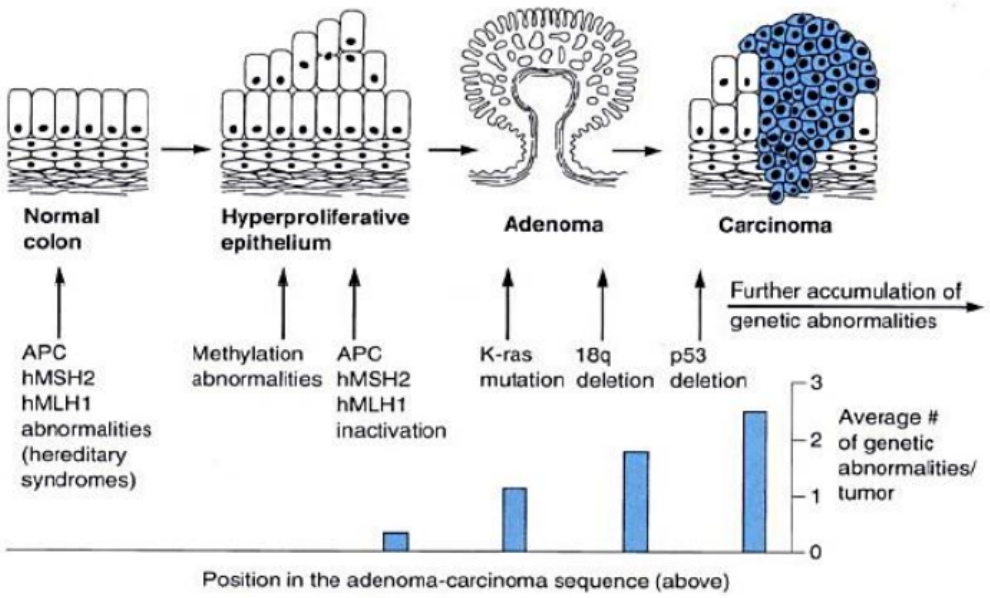

Fig. 2.4: Colorectal carcinogenesis (adapted from Sá (2008)).

Benign tumors are mainly known as polyps. These bodies do not invade or migrate throughout the body. They can be removed through endoscopic techniques. If not removed they are likely to become malignant, or carcinomas. most of the cancers are originated thereby Sá (2008).

The onset of colorectal cancer depends on many factors related to lifestyle in conjunction with genetic predispositions Sá (2008).

Risk Factors

Several factors influence the development of colorectal cancer, such as food, environmental, and even hereditary diseases that may trigger colorectal cancer. The incidence is similar in both gender and increases from the age of forty. Although, is from fifty years on that the number increases exponentially, about 90% of the detected cases Sá (2008).

Long-term studies indicate that the risk increases with higher body mass index. Since that is related to poor eating habits, such as low vegetable and fibers consumption and excessive of carbohydrates and red meat. The incidence of colorectal cancer decreases 20% with the adoption of a balanced diet such as the mediterranean. Physical inactivity is transversal in health and affects not only the incidence of colorectal cancer but also other cancers, diseases and complications, stroke, hypertension, diabetes, heart disease, among others Sá (2008).

The risk is even greater when there is a personal history of adenomatous polyps in the family. The number and size of polyps greater than one inch, increases the risk of developing colorectal cancer, as well as inflammatory bowel diseases such as Ulcerative Colitis or Crohn's disease Sá (2008).

It is also necessary to consider the hereditary history, because 15 to 25% of colorectal cancers are hereditary. The familial adenomatous polyposis syndrome and the hereditary colorectal cancer non-associated with polyposis are autosomal disorders. In this case occurs a mutation in DNA repair sequence. There is a peak incidence between forty and fifty years of age. Familial adenomatous polyposis is characterized by the development of multiple adenomatous polyps and based on a mutation in the adenomatous polyposis coli gene. Most of the patients, more than 90%, develops polyps since its thirty-five years Sá (2008).

2.3 Aberrant Crypt Foci as biomarkers of Colorectal Cancer

It is thought that the aberrant crypt foci have a key role in the adenoma-carcinoma sequence of colorectal cancer. Were first discovered by Bird in 1987 when running laboratory tests in rodents. In this study the colon of rodents was examined under a microscope after being stained with methylene blue. This was followed by several studies that focused on the possibility of the aberrant crypt foci being precursors of neoplasms, Fig 2.5. The

results were promising and aberrant crypt foci were considered biomarkers of colorectal cancer. From this consideration on, interventions and therapeutic methods have been changed to halt or reverse the onset or growth of aberrant crypt foci in order to prevent cancer of the colon and rectum Wargovich et al. (2010).

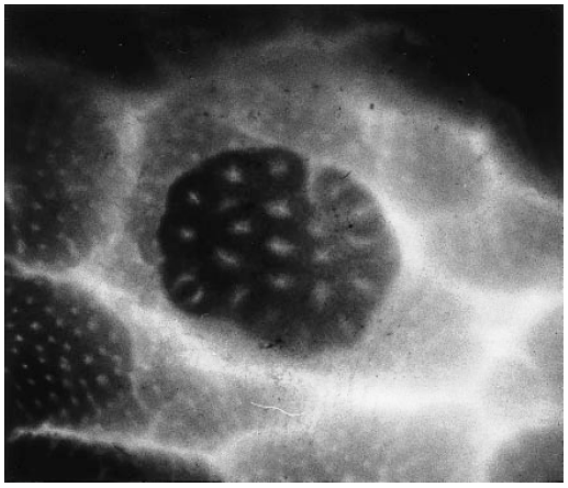

Fig. 2.5: Aberrant crypt foci containing 25 visible cyprts (adapted from Gregorio et al. (1997)).

Studies show that the number of aberrant crypt foci is higher in patients with carcinomas than those with adenomas, same goes for the size of aberrant crypt foci, higher in patients diagnosed with colorectal cancer. The presence of aberrant crypt foci is most prevalent from forty years of age, at which colonoscopy should be performed regularly since this age Gregorio et al. (1997); Takayama et al. (1998); Alrawi et al. (2006).

2.3.1 ACF Histology

There is no fixed number of aberrant crypt for its classification on a focus aberrant crypt, but, on average, is about 5 to 35 crypts, Fig 2.6. The aberrant crypt lumen have elliptical and must be at least twice as large when compared with normal crypts Gupta et al. (2007).

There are three types of aberrant crypt foci, those presenting dysplasia, those who do not (microadenomas) and those having hyperplasia Roncucci et al. (1997); Kukitsu et al. (2008).

Outbreaks that have normal mucosa and epithelial lining unchanged, and merely finds an increase in the size of the crypts are the foci without dysplasia. In foci with dysplasia, both the crypts cells are altered. Have less ability to mucus production, in addition to increase in size, Fig 2.7. The crypt hyperplasia also present dysplasia Otori et al. (1995); Rodriguez et al. (2007); Shpitz et al. (2003).

(a) (b)

Fig. 2.6: Relation bwtween thickness of normal crypts (blue) and aberrant ones (dark blue) (a) Histology of an aberrant crypt foci with dysplasia (b) (adapted from Gupta et al. (2007)).

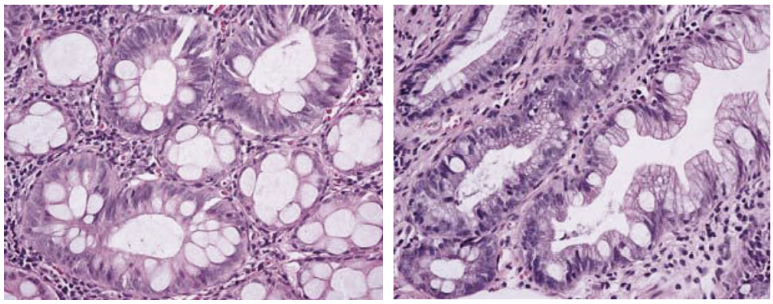

(a) (b)

Fig. 2.7: Aberrant crypt foci with dysplasia (a) and with both dysplasia and hyperplasia (b) (adapted from Rodriguez et al. (2007)).

2.3.2 Genetic Mutations in ACF

Colorectal cancer is the result of several genetic mutations. Knowing that aberrant crypt foci are precursors of this cancer, it should also experience some of these mutations. In humans, mutations of K-RAS gene was identified in 73% of aberrant crypt foci. This mutation is rare in familial adenomatous polyposis Pinto (2010).

Mutation of the familial adenomatous polyposis gene in polyps is common, but more difficult to identify the mutation when compared with K-RAS. Mutations of p53 are seen as an event that occurs in the final stages of carcinogenesis, but was not detected in aberrant crypt foci Pretlow and Pretlow (2005); Hamilton and Aaltonen (2000).

2.4 Diagnostic Methods

From all points of view, the main goal in healthcare is to prevent diseases. However, this is not always possible. Primary phases are responsible for preventing the disease from occurring, often supplemented outside the health system, working directly in the community. The secondary, is to detect the disease early, even when there are no symptoms. The tertiary level is palliative care and increasing the quality of life time Colditz et al. (2000).

The best example of primary prevention is advising the population to adopt healthier lifestyles. Approximately 50% of colorectal cancers are preventable Colditz et al. (2000).

The secondary is chemoprevention and screening. The chemoprevention is defined as a prophylactic medication that can reduce the likelihood of developing the disease. Ursodeoxycholic acid has antineoplastic activity in animal models of colorectal carcinogenesis. Existing clinical trials showed similar effects to man. Several studies suggest that hormone replacement therapy after menopause can reduce the risk of colorectal cancer. The anti-inflammatory drugs, aspirin and others prevent the development of adenomas in the colon Colditz et al. (2000).

2.4.1 Fecal Tests

Fecal Occult Blood

Is able to detect the presence of blood in the stool, which can only be viewed microscopically. The presence of blood in the stool is a finding without specification, however, it may come from colon cancer or large polyps. When checking for the presence of blood, the patient should perform a colonoscopy to evaluate the entire colon and rectum in case of a positive result Maria (2009).

The gFOBT (Guaiac fecal-occult blood test) is the most common and the only test for which there is evidence of effectiveness. This test identifies the presence of hemoglobin in samples of human feces. The FIT (Fecal immunological test) uses an immunochemical method to identify the presence of occult blood in the stool. The spectrum of benefits and limitations is similar to gFOBT except with greater sensitivity Maria (2009).

Fecal DNA

Cells that integrate the process of carcinogenesis suffer DNA mutations during the adenoma-carcinoma sequence and because it is stable, it can be identified and isolated from the bacterial DNA present in feces. The construction of altered DNA databases facilitates the identification process. There is no specific mutation exclusive of all cancers or adenomas,

however, is currently being marketed a kit (PreGen-Plus) having a plurality of markers. Twenty of these markers serve for the identification of p53 genes, familial adenomatous polyposis and K-RAS. This test assesses the whole sample, not just a fragment thereof, as in gFOBT and FIT. In the presence of a positive result is also necessary to perform a colonoscopy Maria (2009).

2.4.2 Imagiology Tests

Barium Enema

Examination conducted from the coating of the mucosal surface with a positive contrast, usually barium, associated with a negative contrast air. It is completed by multiple abdominal radiographs in different positions. Barium is an inert substance, insoluble, with high radiopacity, low cost, but has the disadvantage of sedimentation which can cause constipation for a few days after the exam. Air is injected via a rectal catheter in order to distend the colon, allowing a detailed study of the mucosa. Requires a prior bowel preparation to a diet low in fiber and foods that speed up intestinal transit. Usually is necessary to use laxatives to empty the lower intestinal tract without the need of sedation. The advantage of this procedure is the possibility to evaluate the entire colon, enabling detection of almost all tumors and polyps, Fig 2.8. It is an alternative for patients whose colonoscopy is contraindicated or has failed Rubesin et al. (2000).

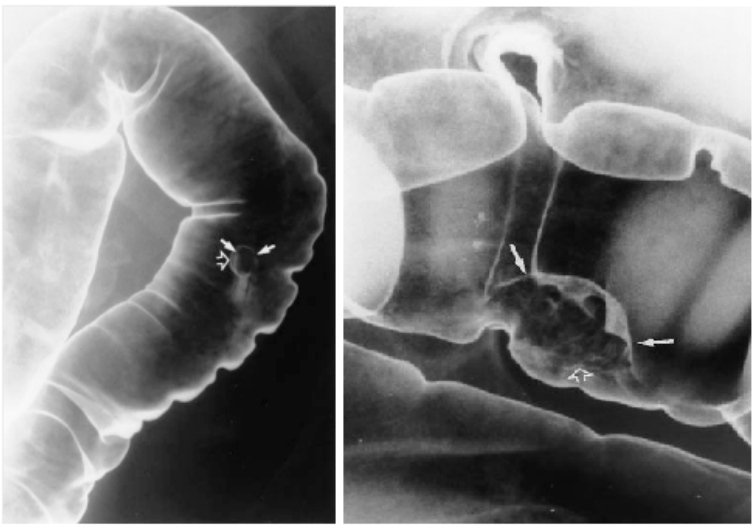

Fig. 2.8: Polyp detection with barium enema. Arrows point to an obstruction in the intestine (adapted from Rubesin et al. (2000)).

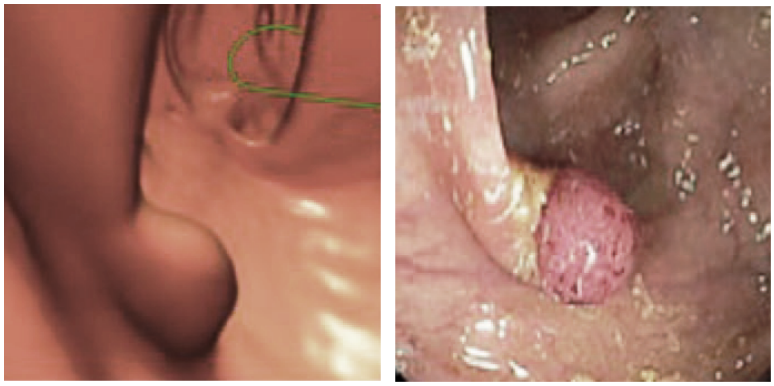

(a) (b)

Fig. 2.9: Detection of a polyp by virtual colonoscopy (a) the same lesion detected after in colonoscopy (b) (adapted from Cash et al. (2011)).

Virtual Colonoscopy

Imaging examination, non-invasive, capable of evaluating the colon and rectum. Similar to CT (Computerized Tomography), endowed with reconstruction algorithms that transform two-dimensional images into three-dimensional, to allow an interactive analysis. Allows 3D visualization of the colon and the identification of lesions, such as polyps or carcinomas, Fig 2.9. It is an exam that requires rigorous bowel preparation based also on a diet low in fiber and laxative with one to two days before. The presence of feces, fluid and smooth muscle spasms may hamper the detection of lesions. One drug is administered to relax intestinal smooth muscle. It is not necessary sedation and patient is required to perform apnea during short times for image acquisition. It is inserted into the anus a catheter for intestinal insufflation with air or carbon dioxide, in order to expand the colon, as in colonoscopy Cash et al. (2011).

There are not many records to compare to other options that enable complete traceability of the advantages of this technique as well as the limitations and risks Pickhardt et al. (2006).

2.4.3 Endoscopic Tests

Flexible Sigmoidoscopy

It is a real-time technique that allows direct visualization of the rectum and sigmoid colon. Uses a sigmoidoscope, a tube about 60cm long, whose end is equipped with a light, camera lens and a clamp to make biopsies or remove polyps. Is introduced via the anus until the splenic angle. Allows direct visualization of the mucosa and immediate intervention. If polyps are detected, it will be necessary to perform a colonoscopy, to examine the entire

colon, not just the sigmoid. No sedation is used which can lead to decreased acceptability due to discomfort caused by this invasive technique Brotherstone et al. (2007).

Colonoscopy

Colonoscopy is the gold standard for screening colorectal cancer. It is an invasive procedure, introducing a colonoscope, Fig 2.10, from the anus to the cecum, allowing the visualization of the entire colon, unlike the flexible sigmoidoscopy. Allows removal of the tissue for examination, biopsy and to remove polyps. The intestinal preparation required is very strict, dietary fiber, one to two days before, followed by ingestion of a wash solution to clean the intestinal tract. This preparation is essential to obtain valid results, if not the colonoscopy may even be discontinued and the whole preparation procedure repeated. The patient can choose from sedation or general anesthesia. The specificity of this technique is not static and new imaging techniques known as magnification chromocolonoscopy, continues to allow their superiority in the detection of neoplastic lesions Maillard et al. (2008); Taylor et al. (2003).

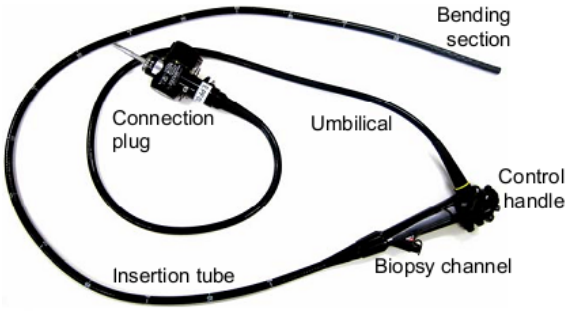

Fig. 2.10: Example of a colonoscope (adapted from Maillard et al. (2008)).

This technique is both time consuming, whether on the preparation days before examination, when using anesthesia, or even when the patient requiries recovery in the hospital. Beyond that, is required to be accompanied to be able to return home. It is, like the others, a technique that relies on the skill and expertise of the technician, is not automated. In Portugal, only medical gastroenterologists are qualified to perform endoscopic techniques after specialized training in the area Maillard et al. (2008); Taylor et al. (2003).

Colonoscopy also has its limitations, identification of benign or malignant polyps usually requires a biopsy followed by histological analysis. However, the combination of new techniques, such as magnification chromocolonoscopy and NBI (narrow band imaging) allows histology observation in vivo, Fig 2.11, as well as highlight damaged areas by contrast Emura et al. (2007).

The aberrant crypt foci are usually stained with methylene blue, a dye, because it is

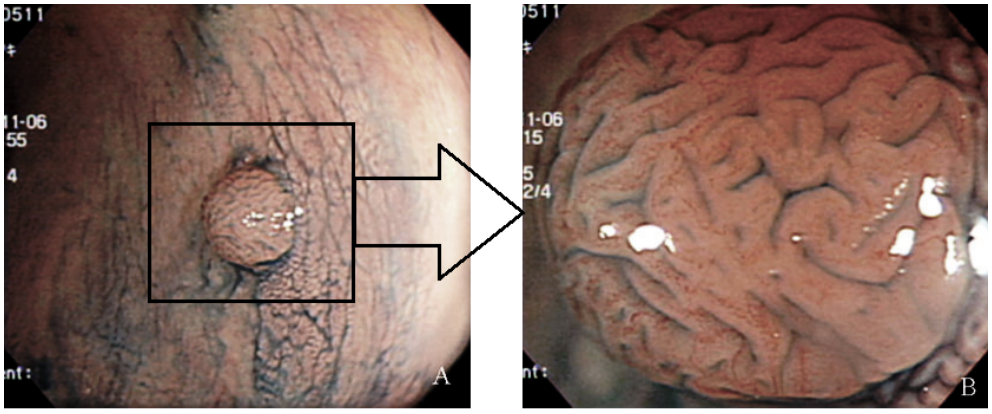

Fig. 2.11: Visualization of a round shape polyp. Zooming operation confirms adenoma (adapted from Emura et al. (2007)).

easily absorbed by the mucosal epithelium of the colon and rectum. Other colors may be used, Lugol's iodine, indigo carmine, congo red or phenol red Song et al. (2007); Kato et al. (2006); Kida et al. (2003).

Endoscopic Capsule

Colonoscopy and its different techniques are the best way of tracking diseases or injuries in the low intestinal tract (colon and rectum). However, it is an invasive procedure and has various associated costs either patient related or to the national healthcare services, that needs to give qualified trainning to doctors for such examination. There is also the need to examine the entire digestive tract and in this aspect the endoscopic capsule is a valuable alternative. It is a device of small dimensions, so it can be swallowed as a pill, Fig 2.12. It has batteries, a UHF antenna, LED lighting, lenses and a CMOS sensor. The capsule moves along the digestive tract by gravity and peristalsis Lima (2008).

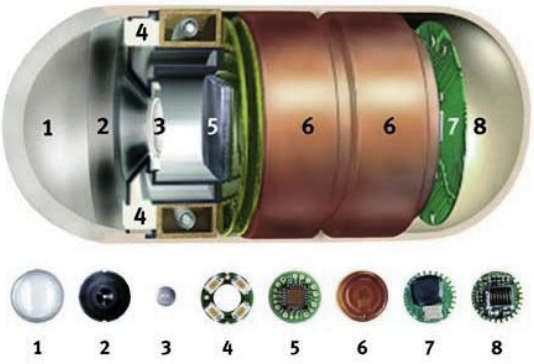

Fig. 2.12: Endoscopic capsule and its components: optical area (1); optical fixator (2); Lens (3); LEDs (4); CMOS sensor (5); batteries (6); microcontroller (7); antenna (8) (adapted from Lima (2008)).

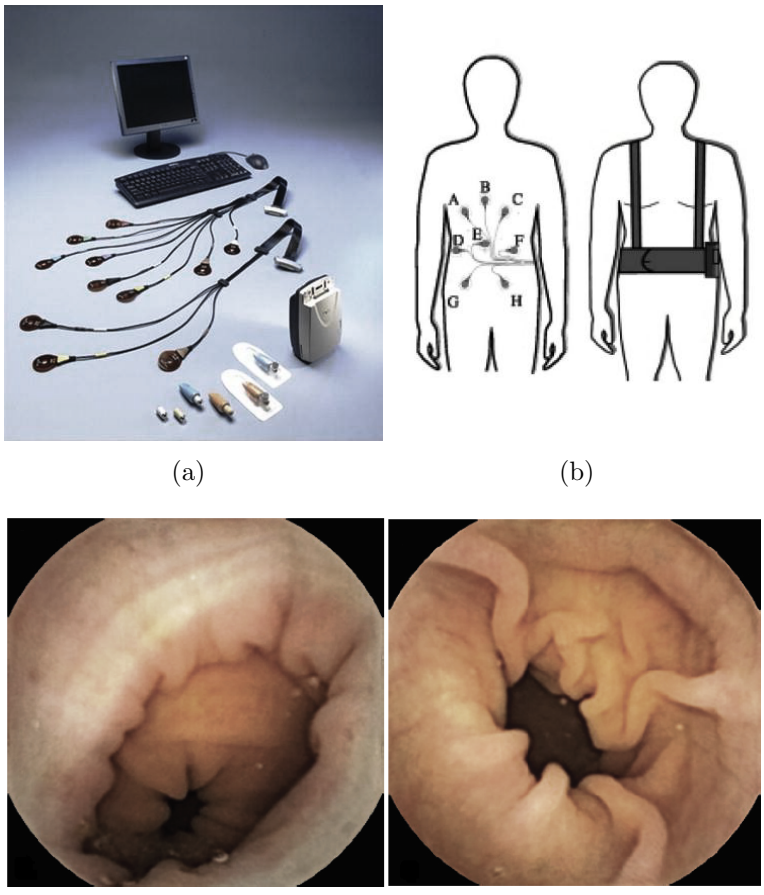

(a) (b)

(c)

Fig. 2.13: Acquisition system (a) body sensor positioning (b) example of images acquired with endoscopic capsule (c) (adapted from Lima (2008); Iobagiu et al. (2007)).

The system transmits wirelessly the images to an acquisition system fixed on the patient, Fig 2.13. Through a system of triangulation from the antennas is possible to estimate the position of the capsule in the body. The capsule batteries have sufficient time to analyze the whole digestive tract. The content is then analyzed in the hospital without surgery or sedation, transferring the images collected by the recorder to a computer Iobagiu et al. (2007); Adler et al. (2008); Fernandez-Urien et al. (2008).

2.5 Summary

The main function of the large intestine is to absorb water from digested food. The mucosa is characterized by the absence of villi and the presence of crypts (straight tubular glands) coated by goblet cells. The colon essentially secretes mucus and there is little enzymatic activity. The mucus lubricates the wall of the colon and helps aggregation of fecal matter.

Prevention is the most effective way to avoid colorectal cancer, acting on modifiable

risk factors, such as diet and physical exercise.

The aberrant crypt foci, biomarkers of colorectal cancer, can be used to identify individuals with a predisposition to develop colorectal cancer.

Even with the advance of new techniques the colonoscopy, remains the most effective and efficient method in the detection of lesions, polyps, in the diagnosis of colorectal cancer and inflammatory diseases such as Crohn's disease or Ulcerative Colitis. The advantage of this technique is to observe the entire colon, which does not occur in flexible sigmoidoscopy, and removal of polyps or biopsy, something the endoscopic capsule is unable to do, yet, it has the ability to capture images of the entire digestive tract.

There are other methods for the detection of colorectal cancer like fecal analyzes or DNA, although in the event of a positive result a colonoscopy must be conducted.

Chapter 3

Computational Image Processing & Analysis

3.1 Context

Image analysis has proven to be very important in several fields, among which the medical. Several pathologies have been detected through the development of new techniques and methods of computational image procesing and analysis. There is an increase in diagnostic efficacy, as well as a decrease in human error, affected by fatigue, boredom, subjectivity and environmental factors.

In this particular case, aberrant crypt foci, the colonoscopy generates a high amount of images (frames) which increases the probability of diagnostic error, since some lesions require special attention because their detection is hard to the naked eye, which is pretty much what is happening nowdays, except for staining tissues in vivo and in situ other advances did not occurred to assist the diagnosis, especially in real time.

The digital images have certain characteristics that can influence their processing and analysis. It is therefore useful to know some of its particularities and characteristics in order to get the most of the existing data or in development algorithms and applications.

3.2 Digital Image

A digital image resembles a two-dimension mathematical function (matrix) $f(x, y)$ where x and y are the coordinates of a point and the amplitude f the intensity value of the pixel. In case it is a color RGB image, there is a matrix for each color, which increases the processing time and physical space it occupies on the hard disk Gonzalez and Woods (2002).

The pixel value depends on the data type that was used for analog to digital conversion of the image. The greater the number of conversion bits, greater the image quality, Fig 3.1.

Usually are used 8 bits, 256 gray levels if the image has only one channel (grayscale). Color images demands 24 bits because 8 bits for each of the three matrices comprising image Burger and Burge (2009).

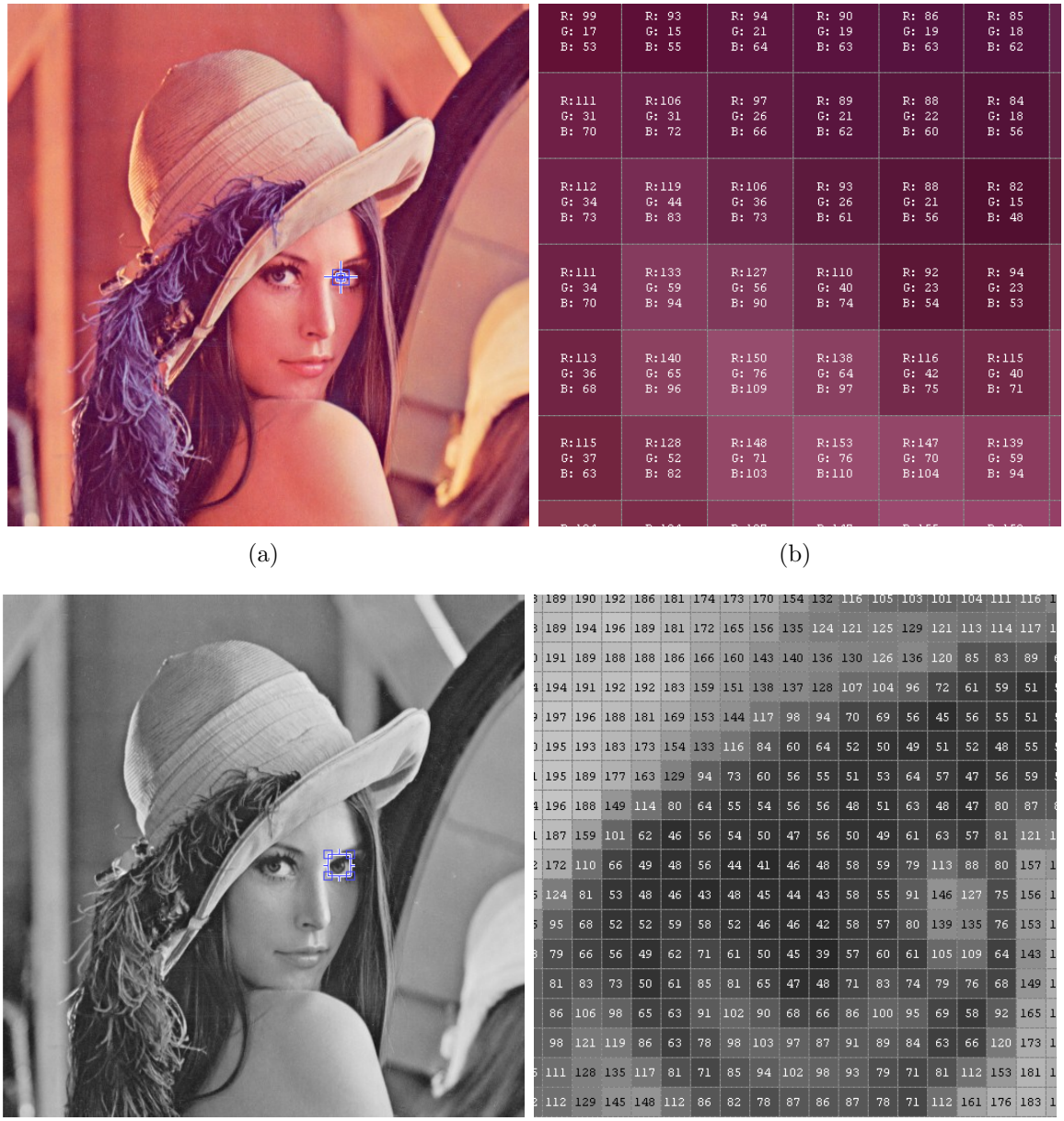

Fig. 3.1: Representation of a digital image: color (a), grayscale (c) and its value matrix (b) and (d), respectively.

An histogram is a distribution of frequencies. It gives an indication of how many times a particular event occurs, in images, the histogram, represents the number of occurrences for each pixel value, Fig 3.2.

The main function of a histogram is to provide statistical data about the image,

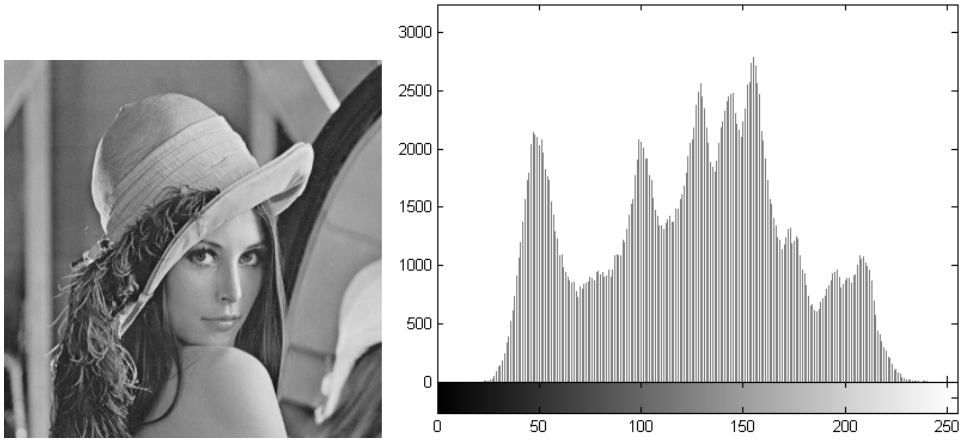

(a) (b)

Fig. 3.2: Original image (a) and its histogram (b).

distribution of intensities, characterization of possible classes (sets of intensities belonging to one object), among others. The histogram has no spatial information, this is lost. It is impossible to convert an image from a histogram.

Fig. 3.3: Three different grayscale images that have the same histogram (adapted from Burger and Burge (2009)).

3.3 Preprocessing

In general, preprocessing is performed to reduce noise and enhance parts or regions of interest in the image. Thus, it is possible to obtain a better image for subsequent operations, which may be the segmentation of structures or objects. It is important to perform a good preprocessing to obtain final results of the analysis more reliable and more easily.

3.3.1 Histogram Preprocessing

It may be necessary to perform histogram operations such as expansion and equalization. The expansion of the histogram allows improvements in visualization and interpretation

of images which have low contrast. The expansion increases the contrast, using the whole range of values that are not being used Burger and Burge (2009).

The histogram equalization also allows contrast enhancement, normalizing the intensities. Equalizes the distribution of gray levels in the final image allowing to obtain greater detail Gonzalez et al. (2004). It is possible to compare the difference between exapansion and equalization of the histogram in Fig 3.4.

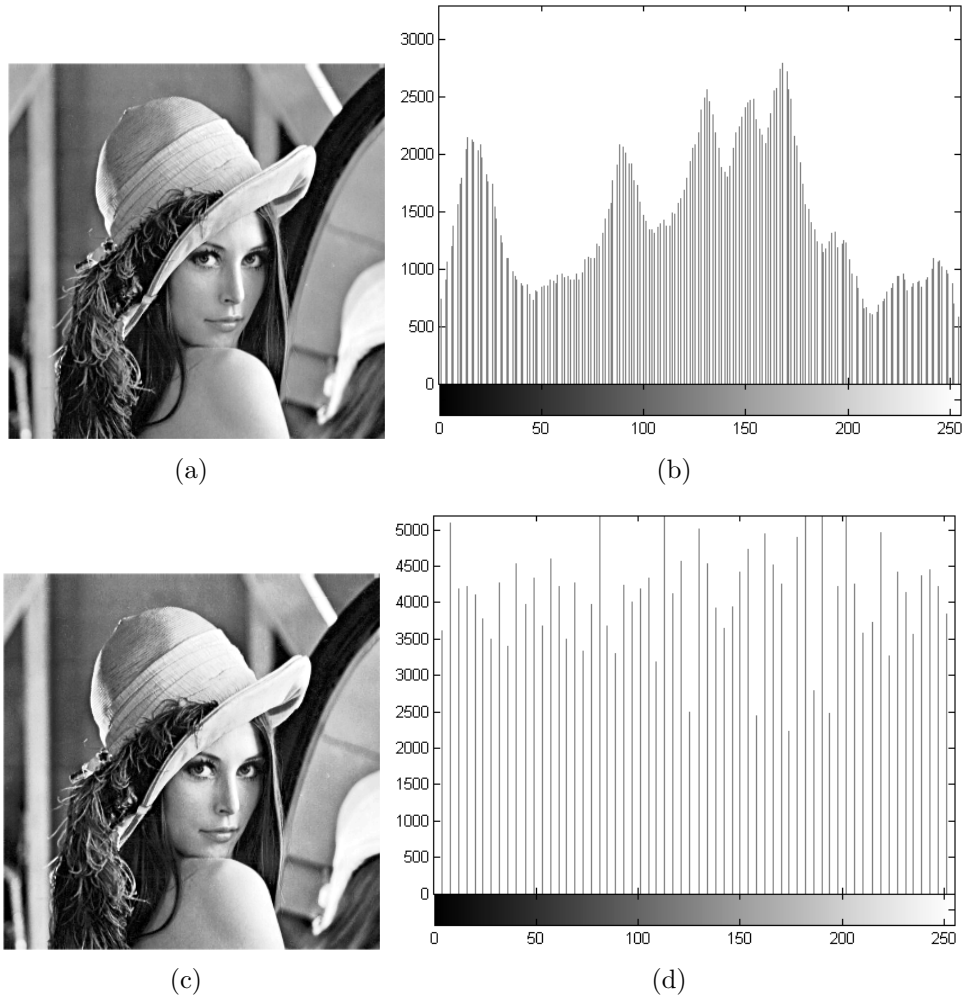

Fig. 3.4: Expansion (a) and its histogram (b). Equalization (c) and its of the histogram (d).

3.3.2 Neighborhood Operators

The spatial filtering is based on local operators using the information of a pixel and its neighborhood to perform calculations. Through convolution of an image by a mask, usually refered as kernel, which will go through, iteratively, the entire image, calculating the value of new pixels, Fig 3.5.

This process is important because it allows smoothing of the original image, removing

noise, extract boundaries and discriminating discontinuities (edges) and may also be useful to highlight objects in an image to ease its posterior segmentation Bankman (2000).

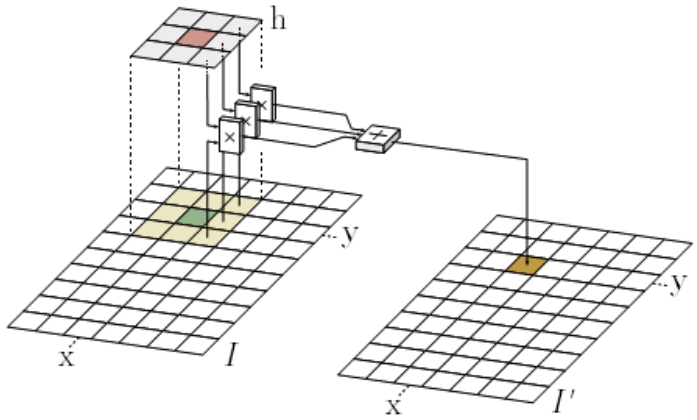

Fig. 3.5: Application of a kernel h to convolute an image I and the resulting image I' (adapted from Burger and Burge (2009)).

To soften the image, filters can be used, linear or nonlinear. The mean filter is an example of a linear smoothing filter. The non-linear filters are also called the order filters Suri et al. (2005).

The mean filter replaces the center pixel of the kernel by its neighborhood arithmetic mean value. Has some undesirable effects, such as blurring, the bigger the kernel the greater the blurring, which results in loss of detail, Fig 3.6. Allows removal of noise because it reduces the difference between white and black pixels within a neighborhood Pratt (2007).

(a) (b) (c)

Fig. 3.6: Mean filter with different size kernels: 3x3 (a) 9x9 (b) 15x15 (c).

The gaussian filter is also a suitable smoothing filter to remove noise with normal distribution, Fig 3.7. In addition to kernel size, it is necessary to choose a sigma value (standard deviation) suitable to contain 95% of the gaussian curve in the kernel Suetens (2009).

(a) (b) (c) (d) (e) (f)

Fig. 3.7: Gaussian filter with different size kernels: 3x3 (a) 9x9 (b) 15x15 (c) and sigma value of 5. Same kernel size 9x9 and different sigmas: 5 (d) 10 (e) 50 (f).

Gaussian or average filters are usually used to soften the image, however the information on the contours or discontinuities can be lost, Fig 3.8.

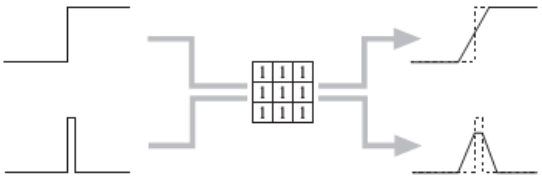

Fig. 3.8: Edge loss with average smoothing (adapted from Burger and Burge (2009)).

In order to preserve some of the contours it should be used order filters or non-linear, such as the median, minimum or maximum Burger and Burge (2009). The expression order is used once the image is convoluted with a given kernel the resulted it then sorted, Fig 3.9.

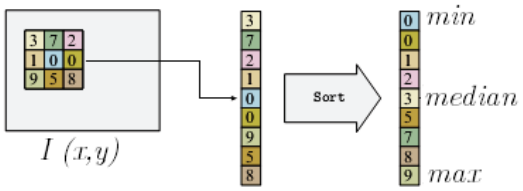

Fig. 3.9: Non-linear filters (adapted from Burger and Burge (2009)).

Values are adjusted to the filter, middle value if it is median, the lowest value for the minimum and the highest to maximum filter, Fig 3.10. The median filter is ideal for removing salt and pepper noise from a corrupted image Burger and Burge (2009); Suetens (2009).

In some cases it may be necessary to increase the sharpness of the image (sharpening) through filters of high frequencies, where the image obtained is added or subtracted from the initial image (unsharp), dependent on the value of the kernel. This emphasizes the discontinuities through first or second order derivatives Gonzalez et al. (2004).

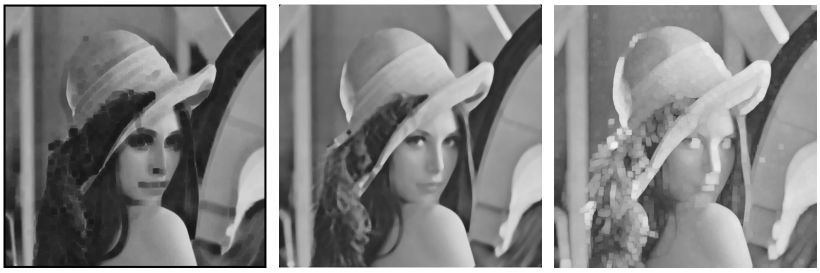

(a) (b) (c)

Fig. 3.10: Minimum (a) median (b) maximum (c) with a 9x9 kernel.

The use of the second order derivative or Laplace, Eq 3.1, has the advantage of discretization of the contours, border areas, Fig 3.11. That can enable a better segmentation, once it is possible to find the boundaries of objects in the image Gonzalez and Woods (2002).

$$\nabla^2 f = \frac{\partial^2 f}{\partial x^2} + \frac{\partial^2 f}{\partial y^2} \tag{3.1}$$

$$\frac{\partial^2 f}{\partial x^2} = f(x+1, y) + f(x-1, y) - 2f(x, y) \tag{3.2}$$

$$\frac{\partial^2 f}{\partial y^2} = f(x, y+1) + f(x, y-1) - 2f(x, y) \tag{3.3}$$

(a) (b) (c)

Fig. 3.11: Original image (a) laplace (b) result (c) after unsharp operation.

The first order derivative, Fig 3.12, can also be used to highlight discontinuities in the image, by gradient magnitude, Eq 3.4.

$$\nabla f = \begin{bmatrix} Gx \\ Gy \end{bmatrix} = \begin{bmatrix} \frac{\partial f}{\partial x} \\ \frac{\partial f}{\partial y} \end{bmatrix} \tag{3.4}$$

$$\nabla f = \sqrt{Gx^2 + Gy^2} = \sqrt{\left(\frac{\partial f}{\partial x}\right)^2 + \left(\frac{\partial f}{\partial y}\right)^2} \tag{3.5}$$

$$\theta = \tan^{-1}\left(\frac{Gy}{Gx}\right) \tag{3.6}$$

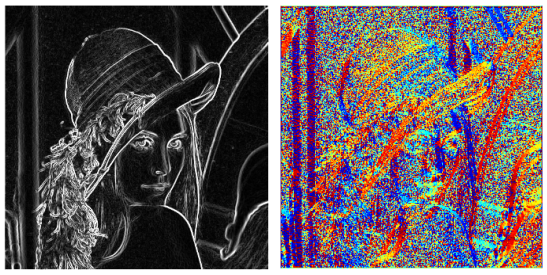

(a) (b)

Fig. 3.12: Gradient magnitude (a) and gradient phase (b).

3.3.3 Morphological Operators

Typically used in binary images, morphological operators may also be used in grayscale images and the result is similar to minimum and maximum operations Burger and Burge (2009).

The morphological operators such as dilation, erosion, opening and closing are used for noise removal local thinning or growth of a region of interest, closing holes in an object or when combined with other techniques to detect contours of regions Gonzalez et al. (2004).

The expansion, Fig 3.13(a), (dilate) corresponds intuitively to the growth of a given region by a given kernel h in an image I, Eq 3.7. Erosion, Fig 3.13(b), corresponds, therefore, to a contraction of a region by a given kernel, Eq 3.8.

$$I \oplus h = \Big\{(p+q) \mid \forall p \in I, q \in h\Big\} \tag{3.7}$$

$$I \ominus h = \Big\{(p+q) \mid \forall p \in I, q \in h\Big\} \tag{3.8}$$

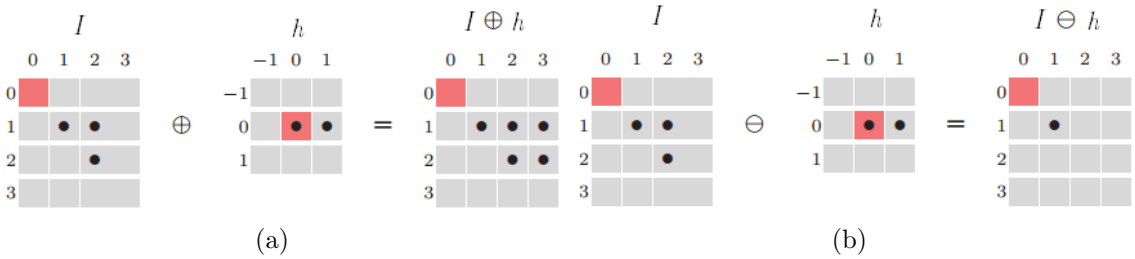

(a) (b)

Fig. 3.13: Dilate (a) and erode (b) operation (adapted from Burger and Burge (2009)).

The kernel can have different shapes, such as square, line, circular-shaped or cross-like, so that it can be possible to find image objects that resemble the kernel, Fig 3.14.

(a) (b) (c) (d)

Fig. 3.14: Dilate with round (a) square kernels (b). Erode with round (c) square kernels (d).

The aperture, Eq 3.9, is a morphological process where the image is eroded, and then dilated, enables removing noise caused by pixel size less than or equal to the size and shape of the kernel,Fig 3.15.

$$I \circledcirc h = (I \ominus h) \oplus h \tag{3.9}$$

The closure, Eq 3.10, is similar, consisting of a expansion succeeded by an erosion, generally used to remove holes in an image, Fig 3.15.

$$I \odot h = (I \oplus h) \ominus h \tag{3.10}$$

(a) (b) (c) (d)

Fig. 3.15: Open with round (a) square kernels (b). Close with round (c) square kernels (d).

3.4 Segmentation

Segmentation is, generally, the important step in the computational image processing and analysis and, particularly, in the field of medical imaging. Segmentation allows, for

example, locate an area of interest, also known as region of interest, or just ROI, to facilitate the visualization and feature extraction of that region in an image Pratt (2007).

There is not a general method of segmentation, as if it were a filter, to segment a structure or object in an image, but rather a set of techniques that assist this process. The intensities of pixels, detection of edges, texture and color are characteristics that may facilitate this process Pratt (2007).

Segmentation, Fig 3.16, may be divided into three major areas: Thresholding, Region-based and Boundary-Based Suetens (2009).

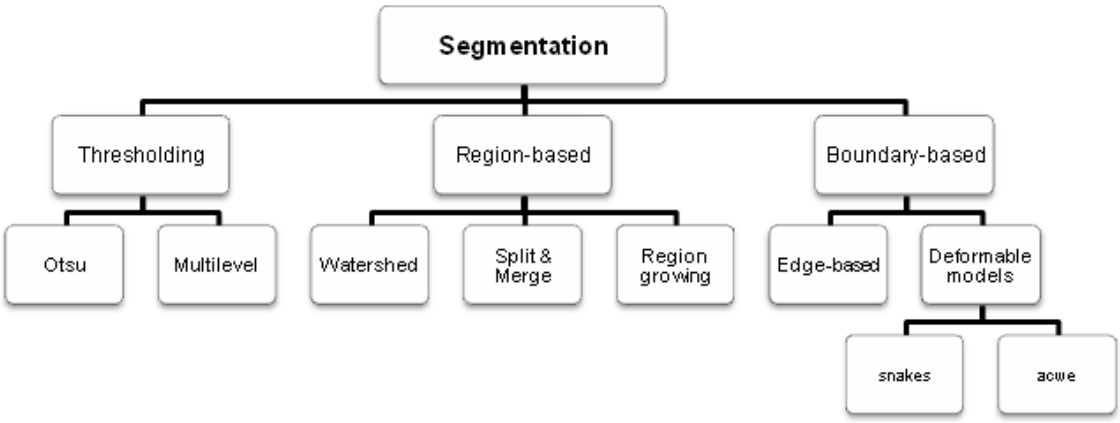

Fig. 3.16: Types of segmentation (adapted from Suetens (2009)).

3.4.1 Thresholding

This type of segmentation is based on the analysis of the histogram and intensity of the pixels. It can be written mathematically as a condition, Eq 3.11. Where I is the image, T the value of threshold and I' the resulting image binarized.

$$I'(x,y) = \begin{cases} 0, I(x,y) < T \\ 1, I(x,y) \geq T \end{cases} \tag{3.11}$$

The operations can be manual, where the user defines a threshold value or by an automatic histogram analysis wich allows determining the optimal value of the threshold operation Alves (2011).

The method developed by Otsu in 1979 allows the calculation of the threshold value by analysis of the histogram. This method is very efficient and effective in bimodal histograms, corresponding to images with a background and well-defined white objects or structures, foreground. However, this method has limitations when there are more modes in an histogram corresponding to different objects or structures Otsu (1979).

Otsu's method is based on increasing the distance between classes (mode) decreasing

the distance within the class. It is an iterative process that combines different intensities in two distinct classes and ends when the threshold value from one iteration to another remains the same.

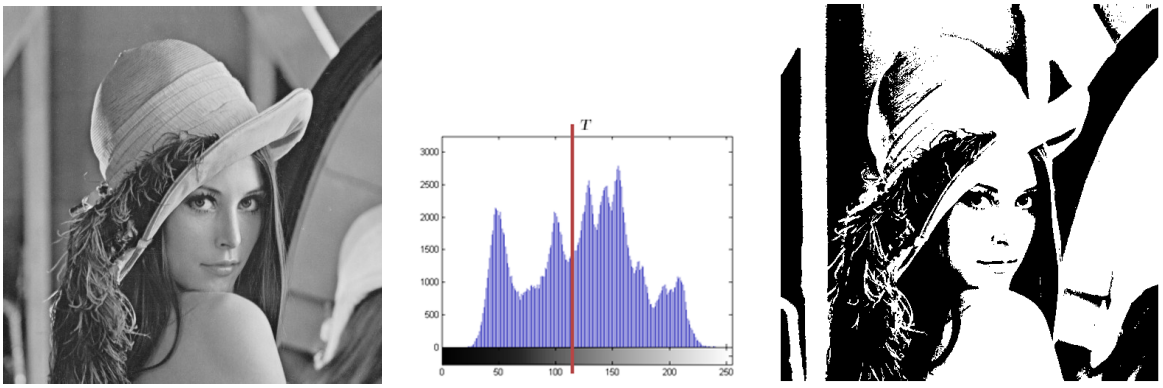

(a) (b) (c)

Fig. 3.17: Original image (a) Otsu's threshold (b) binarized image (c).

As it is possible to confirm in Fig 3.17 the selected image doe not have a bimodal histogram. Although binarization was performed the result may not be satisfactory. This will require using a more reliable segmentation algorithm that allows calculating the threshold values for images that have multimodal histograms Tsai (1995).

The histogram, as if it were a signal, is processed, smoothed and understated the number and location of the valleys corresponding to border areas between classes. With these values it is possible to segment depending on the number of valleys, Fig 3.18.

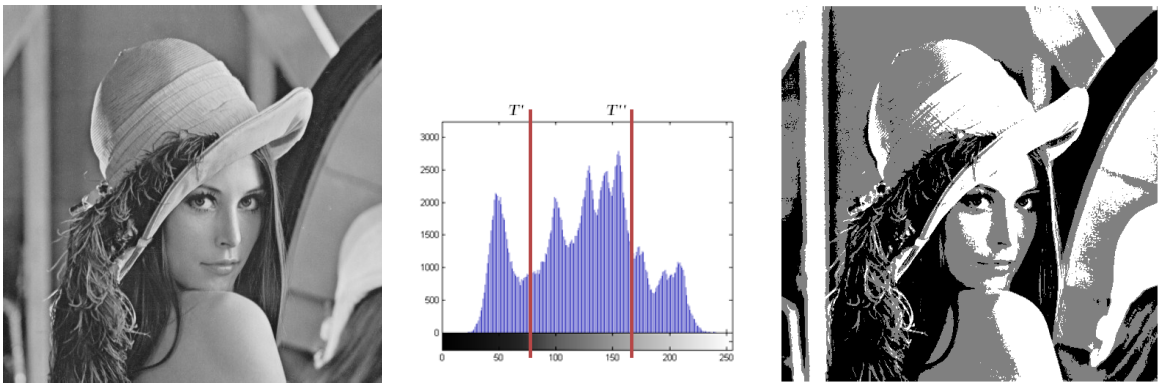

(a) (b) (c)

Fig. 3.18: Original image (a) multilevel threshold (b) binarized image (c).

3.4.2 Region-based

The process of region growing is, also, an iterative process, where a seed is defined in the image and assigned a maximum threshold, in the first iteration the average area is the pixel value as such this calculation is ignored. Then, the neighbors will be attached if their values are not much lower. It is calculated the average values of the region and will be grouped all neighboring pixels that have a value that does not move away from the threshold value initially set. The iteration stops once there are no more pixels to attach or the the neighbor pixels differ from the initial threshold Hojjatoleslami and Kittler (1998).

It is not an automatic process, since it requires the position of the seed to be initially defined. The aggregation threshold value could be calculated with local statistical methods. Although, it is not, the entire process can be autonomous.

(a) (b) (c) (d)

Fig. 3.19: Original image with three different seeds(a). Growth of the defined regions (b)(c)(d).

The Split & Merge method is an alternative technique for segmentation that combines pixels according to their similarity. This is accomplished by blindly dividing the image into regions and continue that division until the algorithm starts aggregating similar pixel intensities and ends when there arise changes Bleau and Leon (2000).

The Watershed is an algorithm commonly used in image processing. It is based on the topological analysis of the image, where the intensity of the pixel corresponds to a quota. Applying the watershed image segmentation technique to an image with only the object contours produces better results Haris et al. (1998).

3.4.3 Boundary-based

Segmentation with the aid of the image edges goes by the name of edge-based segmentation technique. These algorithms target regions separated by boundaries. It utilizes methods such as the first or second order derivatives as already mentioned above.

One of the most known is the Canny algorithm, which implements a LoG (Laplacian of Gaussian) filter, followed by a zero-crossing analysis Canny (1986).

(a) (b) (c) (d)

Fig. 3.20: Same threshold value and different sigmas: 1 (a) 3 (b). Same sigmas, different thresholds: 0.1 (c), 0.5 (d).

One of the most powerful segmentation algorithms based on deformable models is the Snake, or explicit active contours. Snakes are lines that fit the contours through iterative processes where energy minimization occurs inside the line. The snake deforms to match the contour of the object Kass et al. (1988).

The snake position is given by the parametric curve:

$$v(s) = [x(s), y(s)]^T, s \in [0, 1] \tag{3.12}$$

In practice $v(0) = v(1)$ since the curve is closed the starting point is also the end, Fig 3.21. Each point along curve is subject to the influence of external forces and internal forces Tiilikainen (2007).

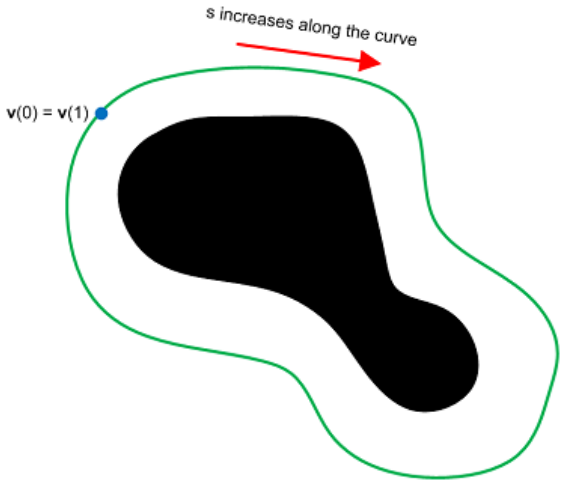

Fig. 3.21: The blue dot marks the starting and ending point of the curve (adapted from Tiilikainen (2007)).

It takes two terms to calculate the energy of a snake, internal and external energy. The sum of both is the total energy of the snake:

$$E_{snake} = \int_0^1 E_{snake}(v(s))ds \tag{3.13}$$

$$E_{snake} = \int_0^1 E_{int}(v(s)) + E_{ext}(v(s))ds \tag{3.14}$$

$$E_{snake} = \int_0^1 E_{int}(v(s)) + E_{img}(v(s)) + E_{con}(v(s))ds \tag{3.15}$$

The internal energy E_{int} is the mean result of the curvature with elasticity, which means that where the curvature of the snake is stretched elasticity is maximal and where the curvature is twisted elasticity is minimal Kass et al. (1988); Tiilikainen (2007).

$$E_{int} = \frac{1}{2}(\alpha(s) \left\|v_s(s))\right\|^2 + \beta(s) \left\|v_{ss}(s))\right\|^2) \tag{3.16}$$

The coefficients α and β generate the stiffness or elasticity of the snake. The external power E_{ext} is composed of E_{img} which attracts the snake to the desired contour and, E_{con} that is an energy defined by a constraint caused by human interaction, for example specifying points so that the outline does not fix in those points Kass et al. (1988); Tiilikainen (2007).

$$E_{img} = \omega_{line}E_{line} + \omega_{edge}E_{edge} + \omega_{term}E_{term} \tag{3.17}$$

Where the terms ω represent coefficients to be defined by the user.

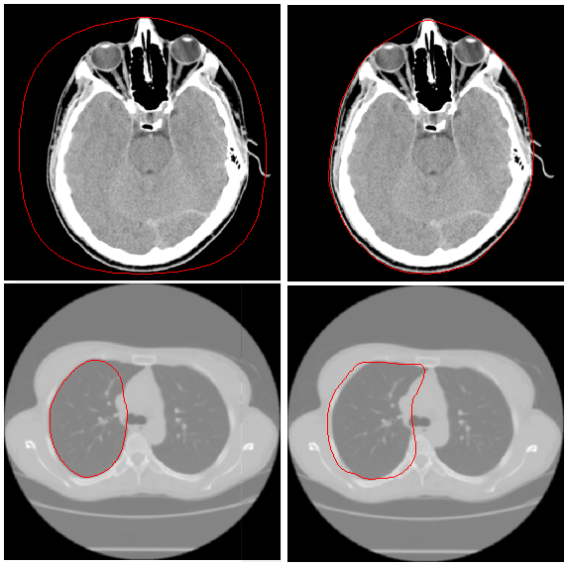

Fig. 3.22: Snake algorithm in two different images. Initial contour in left, final in right.

The Level Sets, also known as implicit active contours, allow targeting of a 2D and

3D image structures, closed contours and surfaces, respectively, which allows the curve to move perpendicularly to itself at a certain speed Vese and Chan (2002); Brox and Weickert (2004).

Unlike snakes this process allows the curve to separate or sling during evolution for a given shape. To this end, instead of following directly the deformable interface, puts the original interface embedded in a scalar function defined on the whole image, the interface is represented as *zero-th* level set (or contour) of the scalar function. Throughout the rest of the image the level set function ϕ is defined by the distance function to *zero-th* level Weeratunga and Kamath (2004); Li et al. (2010).

The function ϕ varies in time and space, $\phi = \Phi(x, y, t)$ is developed using partial differential equations (PDE) that contain terms essentially parabolic or hyperbolic Weeratunga and Kamath (2004).

Knowing that the function ϕ evolves in a direction normal to itself with speed F:

$$\phi(x(t), t) = 0 \tag{3.18}$$

Using the chain rule for partial differential equations, we have:

$$\phi_t + \nabla\phi(x(t), t) \cdot x'(t) = 0 \tag{3.19}$$

being F the speed at the perpendicular to the curvature n:

$$x'(t) \cdot n = F \tag{3.20}$$

$$n = \frac{\nabla\phi}{\|\nabla\phi\|} \tag{3.21}$$

In this case the evolution of ϕ can be written as follows:

$$\phi_t + F\,\|\nabla\phi\| = 0 \tag{3.22}$$

The speed F depends on some factors, such as local properties, the curvature and global properties such as shape and position of the front of the curve. It can be used to control the front curve and is the sum of two terms:

$$F = F_0 + F_1(k) \tag{3.23}$$

Where F_0 is a propagation constant and F_1 a scalar function of the curvature k.

$$k = div\left(\frac{\nabla\phi}{\|\nabla\phi\|}\right) \tag{3.24}$$

The propagation constant F_0 commonly known as balloon force is independent of the geometry of the deformable front. Once the level set is to be used for segmentation, it is necessary that the *zero-th* level set stops its progress when a discontinuity is detected, this can be achieved multiplying the speed F by a factor dependent on the image $g(x, y)$:

$$g(x,y) = \frac{1}{1 + \left(\frac{|\nabla I_\sigma|}{\lambda}\right)^2} \tag{3.25}$$

The I_σ is the image after convolution with a Gaussian filter. Through λ is possible to control the intensity that causes the speed to cancel itself near a discontinuity, with this definition the level set equation can be written as:

$$\frac{\partial \phi}{\partial t} = d(x,y) \cdot \|\nabla \phi\| \left(div \left(\frac{\nabla \phi}{\|\nabla \phi\|} \right) + F_0 \right) + \nabla g \cdot \nabla \phi \tag{3.26}$$

The term $\nabla g \cdot \nabla \phi$ has the attractive effect of contour when near a border or repulsive in case of exceeded it Weeratunga and Kamath (2004).

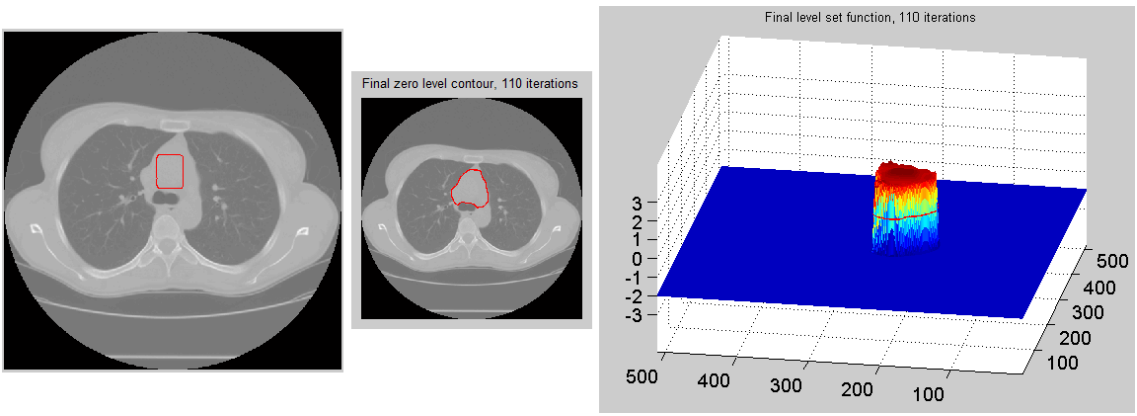

Fig. 3.23: Heart segmentation in a CT image using level set algorithm.

The segmentation model developed by Chan and Vese also known as ACWE (Active Contour without Edges) unlike snakes and level sets uses no boundaries, no gradients, as a stopping criterion in the calculation of the contour. Based on the level set method, is able to define objects or structures which exhibit a high degree of smoothing, with very poor defined contours Vese and Chan (2002); Cohen (2010).

Let Ω be an open limited set in $\mathbb{R}^2$, with $\partial\Omega$ as its boundary. An image $\mu_0 : \Omega' \to \mathbb{R}$ and $C(s)$ a determined curve defined in $C[0, 1]$. The region inside C is ω and the outside region is $\Omega \setminus \omega'$. The image $\mu_0 = \mu_0^{inside} + \mu_0^{outside}$, knowing that c_1 and c_2 are the pixel average values inside and outside the C curve, respectively.

The main objective of the algorithm is to minimize the energy $F(c_1, c_2, C)$ defined by:

$$\begin{aligned} F(c_1, c_2, C) = \mu \cdot length(C) + v \cdot Area(inside(C)) \\ +\lambda_1 \int_{inside(C)} |\mu_0(x,y) - c_1|^2 \, dxdy \\ +\lambda_2 \int_{outside(C)} |\mu_0(x,y) - c_2|^2 \, dxdy \end{aligned} \tag{3.27}$$

Where $\mu \geq 0, v \geq 0, [\lambda_1, \lambda_2] > 0$ are fixed parameters, usually defined by the user. Sugested by Chan and Vese, $v = 0, [\lambda_1, \lambda_2] = 1$.

The solution will be the minimazation of the following problem:

$$\inf_{c_1, c_2, C} F(c_1, c_2, C) \tag{3.28}$$

Which can also be formalized in a level set, $C \subset \Omega$ is represented by *zero-th* level set by a function of Lipschitz $\phi : \Omega \to \mathbb{R}$.

$$\begin{cases} C = \partial\omega = \{(x,y) \in \Omega : \phi(x,y) = 0\} \\ inside(C) = \omega = \{(x,y) \in \Omega : \phi(x,y) > 0\} \\ outside(C) = \Omega \setminus \omega' = \{(x,y) \in \Omega : \phi(x,y) < 0\} \end{cases} \tag{3.29}$$

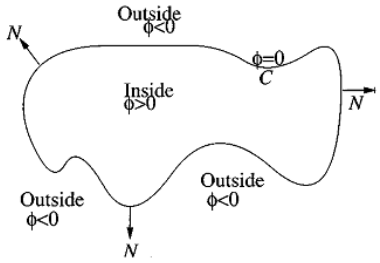

Fig. 3.24: Value of ϕ in function of C (adapted from Cohen (2010)).

Given a determined contour C, $\phi(x,y)$ is defined by the distance function from C, when in contour outside $\phi(x,y)$ assumes negative values.

In Fig 3.25 is possible to verify the ability of the Chan & Vese algorithm in performing segmentation in smoothed images, or images with smoothed contours Chan and Vese (2001).

3.5 Endoscopic Applications

Currently, the number of researchers in the area of aberrant crypt foci is increasing. This is due to the difficulty of the problem in question, coupled with the need for standardization of procedures and methods to facilitate the work of clinical staff.

The in vivo analysis detection of external borders of aberrant crypt foci and its holes are, for reasons previously seen, extremely relevant for medical diagnosis. So far the meth-

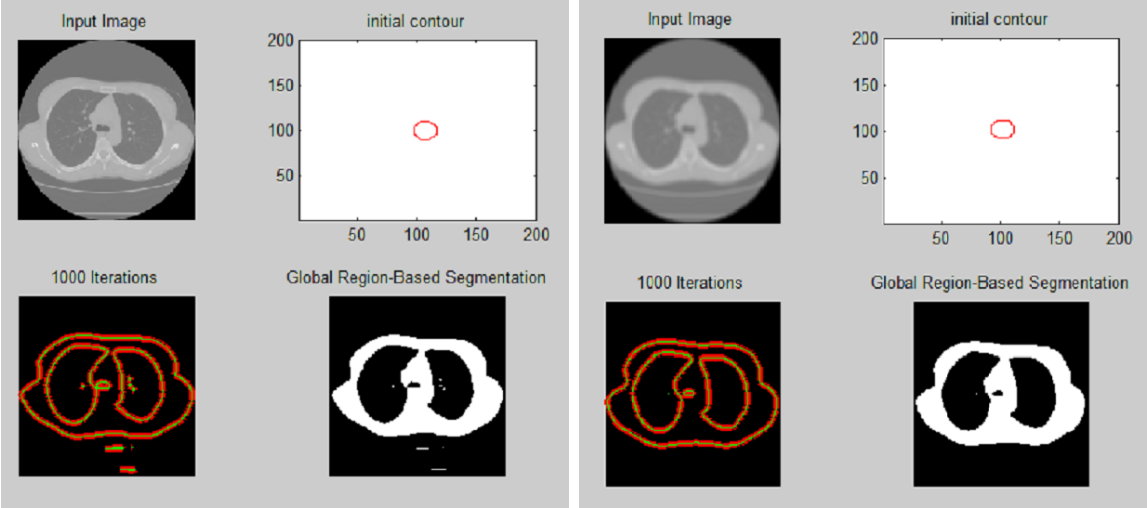

(a) (b)

Fig. 3.25: Chan & Vese algorithm application: original image (a) smoothed image (b).

ods applied to the segmentation and analysis of aberrant crypt foci are somewhat subjective and manual, depending on the direct observation of a medical specialist Figueiredo and Almeida (2011).

3.5.1 Polyp Detection

For automatic detection and segmentation of polyps, structures that can be derived from aberrant crypt foci, there are several algorithms that already have meaningful results. Polyps are larger structures than aberrant crypt foci, precursors in colorectal cancer, and they can even block stool passage in the bowel.

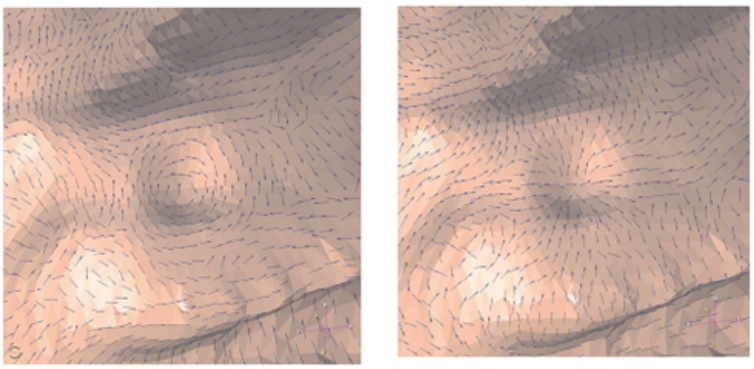

(a) (b)

Fig. 3.26: Circular pattern in maximum curvature directions (a), focusing pattern in minimum pattern directions (adapted from Riaz et al. (2006)).

The automatic detection of polyps can be performed without colonoscopy, using virtual

colonoscopy, it has the advantage of being a noninvasive method. However, for a general screening, the morphological data of the inner wall of the colon and rectum, obtained by conventional colonoscopy is more evident, some methods are based on the curvature, Fig 3.26, shape and texture and still statistical classification by clustering techniques Riaz et al. (2006).

The method for detecting polyps is through the medium or gaussian curvature, as polyps can be characterized by protrusions on the surface of colorectal inner wall Figueiredo et al. (2009).

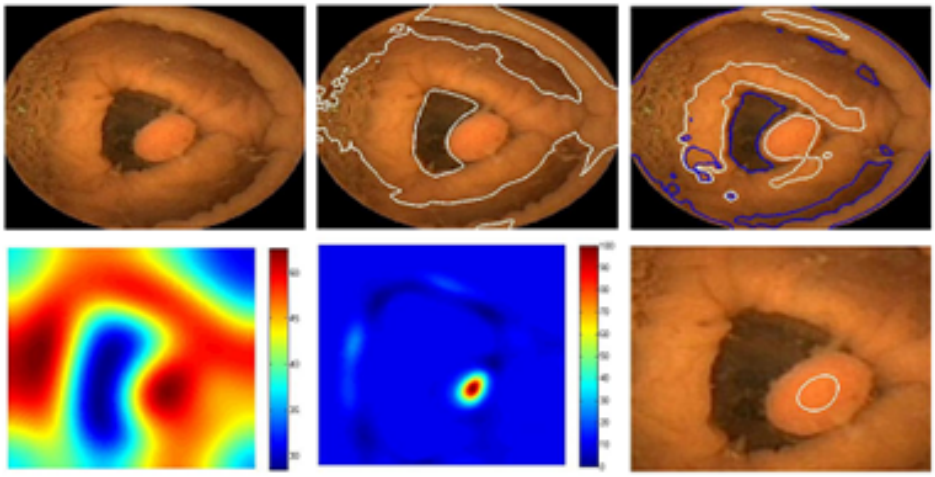

Fig. 3.27: Polyp segmentation in wireless endoscopic capsule image (adapted from Figueiredo et al. (2009)).

For this purpose, the image is pre-processed, where it is converted from RGB to grayscale and smoothed. Information about the points of maximum and minimum intensity are extracted, as well as outlines for possible identification of the polyp. Similar technique is currently used for aberrant crypt foci detection. The segmentation uses the algorithm developed by Chan & Vese formulated to minimize level set errors Chan and Vese (2001); Sethian (1996).

This detection can also be done wirelessly via endoscopic capsules, the acquired video is processed frame-by-frame, as a solo image, using segmentation methods that depend on the texture, shape and color of the object.

The acquired image of endoscopic capsule with polyps, Fig 3.27, segmented by RGB values (in white) debug this segmentation (blue) and correlated this information with the same processing applied to the image in grayscale. The final image is a result of overlapping data where it is possible to verify the spatial location of the polyp. The presence of feces, liquid and air bubbles would jeopardize the correct algorithm functioning Li and Meng (2011); Vilariño et al. (2010).

3.5.2 ACF Segmentation

There has been investigation on mathematical methods that resemble the pattern of the crypts as well as of its own development, so that it is easier to develop algorithms capable of identifying aberrant crypt foci in most cases Figueiredo et al. (2008, 2011a); Apanasovich et al. (2007).

There are several variables which complicate the automatic segmentation process, so this process is currently manual. Factors such as the environment where the images are acquired, with the possible presence of feces, fluid, air bubbles and the proper technique of capturing images, which depends on the ability of the operator of the colonoscope, hamper the process. Other problems are associated with tissue coloration, which may be ineffective, the amount of glare caused by light necessary to illuminate the interior of the colon and rectum. The curvature caused by the lens, blur can also complicate the procedure. The whole segmentation is performed manually, it consumes considerable time and induces errors due to fatigue of the observer and decreases reproducibility Figueiredo et al. (2011b); McGinley et al. (2010).

In Fig 3.28 is possible to check all the manual segmentation performed in *Photoshop*, after segmentation feature extraction is facilitated, determining the area of the crypts, number of crypts, perimeter, among others, then analyzing texture in order to classify the crypt as an aberrant crypt foci correctly McGinley et al. (2010).

Fig. 3.28: From left to right: Manual segmentation, topographic representation, texture-based coloring and feature extraction (adapted from McGinley et al. (2010)).

Other segmentation methods are still being researched, mainly mathematical models, by Figueiredo et al. (2010), through variational segmentation. Also using methods developed by Chan and Vese (2001), modified to be implemented in *Comsol Multiphysics* for the mathematical models formulation and *Matlab* for algorithm implementation as well as using PDE and level set Figueiredo et al. (2008).

There are also some proposals mathematically less complex as proposed by Riaz et al. (2011) which uses a filter LoG (Laplacian of Gaussian) to extract features in conjunction with the Harris corner detector, Fig 3.30.

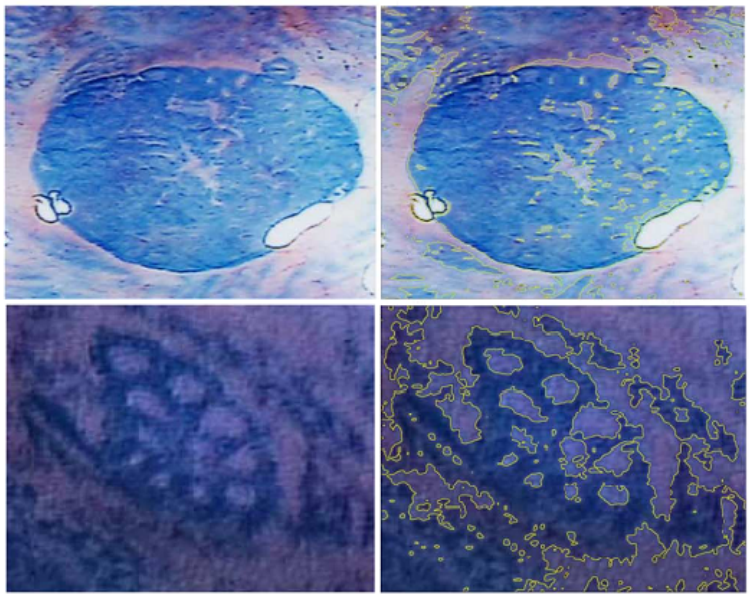

Fig. 3.29: Obtained results in ACF segmentation by Figueiredo et al. (2010) (adapted from Figueiredo et al. (2010)).

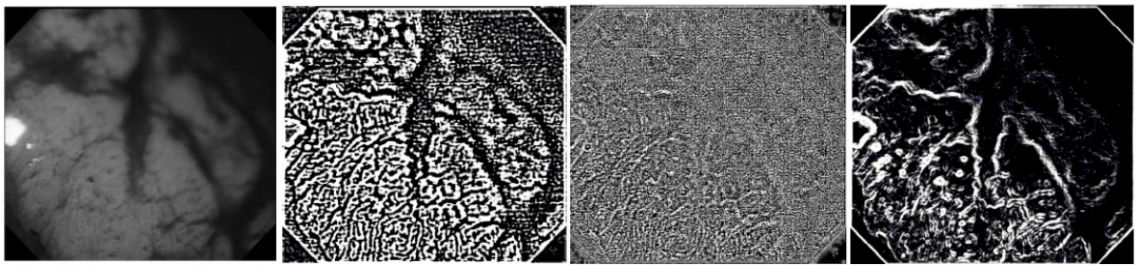

Fig. 3.30: From left to right: Original image in the upper left, after Riaz et al. (2011) algorithm and final result in lower right (adapted from Riaz et al. (2011)).

3.6 Summary

This section allows the understanding of some of the methods either in pre-processing or in image segmentation. It is important to understand the advantages and disadvantages of pre-processing. Segmentation is not a trivial process and presents challenges in the segmentation of structures and objects in medical images. It may be a hybrid process, such as a combination of various techniques in order to obtain results. Most of the chapter's figures are a result of applied filters and segmentation methods mentioned.

To sum up, there has been a lot of research around the aberrant crypt foci. However, there are difficulties, starting with the technique used for image acquisition and, as mentioned above, also dependant on the skill of the doctor during examination. The presence of noise and lighting makes it difficult to standardize targeting process. There are already some proposals based on existing algorithms and improvement thereof.

Chapter 4

Implementations

4.1 Context

The segmentation of ACF has proven to be a difficult task, as evidenced by the fact that even nowadays there is not a method for it is segmentation with high reliability. This method is still being pursued by many developers and researchers, one of the mais drivers in this small community is Figueiredo et al. (2010). The method used is Variational Image Segmentation and her approach is by enhancing the active contours without edges with Chan and Vese (2001) algorithm, employing level sets to extract boundaries it was able to identify ACF, boundaries and internal crypts orificies.

My approach consists, mainly, in hybrid segmentation algorithms, as automatic region growing and color-driven active contours without edges, Fig 4.1. Both techniques rely on previous methods developed and used in preprocessing and feature extraction.

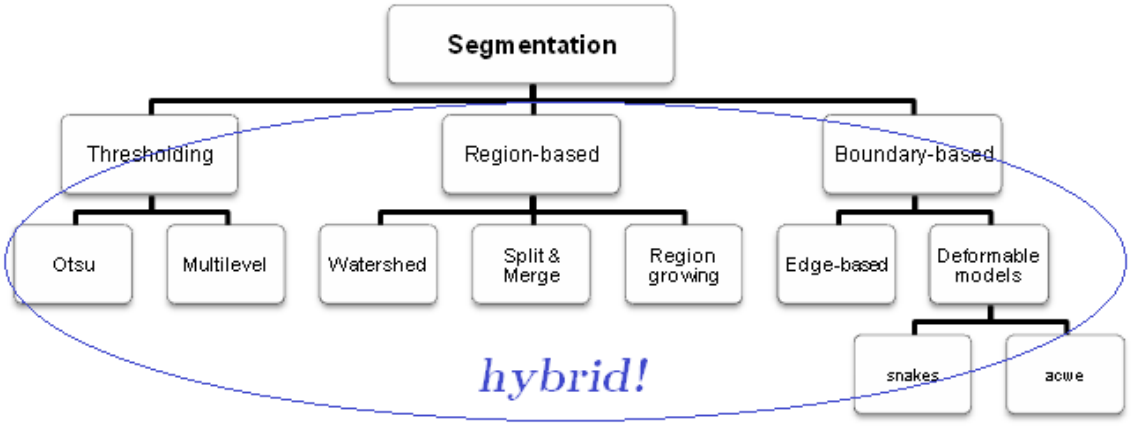

Fig. 4.1: Hybrid Segmentation.

The image acquisition system provides color ACF images which increases developed algorithm input. This is mainly due to dyeing, otherwise the images could be analyzed in

grayscale.

The images contain many artifacts such issues with dyes, sub or over-coloring, illumination difficulties causing dark areas or glare in ROI, the presence of stool or air bubbles and, also, the incorrect use of the colonoscope, intrinsically linked to the technical ability of the clinician who performed the exam.

4.2 Preprocessing

The developed algorithm follows the flowchart in Fig 4.2. It was developed to enhance the original images and, also, testing different smoothing filters, Median, Gaussian with different kernels and sigmas. Anisotropic Diffusion was also used, code was developed by Peter Kovesi (2007) at University of Western Australia, guided by Perona and Malik (1990).

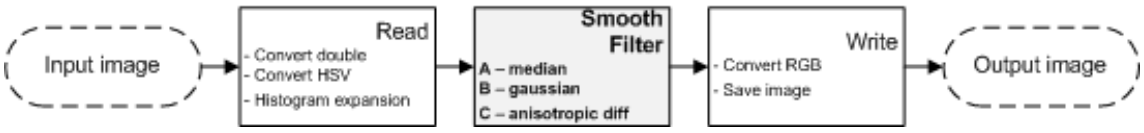

Fig. 4.2: Preprocessing flowchart.

Because of the necessity to remove noise from initial images a preprocessing step is required. Also, in this case, color images will be converted from RGB (Red, Blue and Green) to HSV (Hue, Saturation and Value). There are already many algorithms that convert from RGB to HSV and vice-versa, this will facilitate the preprocessing step.

A smoothing operation needs to be perfomed in order to remove pixel-based speckle, noise or soften large areas where the glare is noticed. If this step is not made properly, segmentation could be oompromised, as mencioned before.

4.3 Feature Extraction

Biomedical images have much information stored in color. It is important to harvest that information in order to be used in the following steps. This is related to the dye used. Methylene blue-stained tissues will reflect a predominance of the blue spectrum, so the blue color channel will have an important characterization of the image.

Also, in this stage it will be already possible to discard non-relevant areas of the image, such as noise, that was already been filtered in the previous step and glare areas. Although, some of the ACF might be in a glare area, it will be necessary to have an estimation of the area affected by glare, Fig 4.3.

The feature extraction stage consists of three feature extraction algorithms that were developed for this intent. The mip (maximum_intensity_projection), get_contour and remove_glare.

Fig. 4.3: Feature Extraction flowchart.

The maximum_intensity_projection is a calculation of the most predominant color of the RGB matrices in one given pixel. It is basically a projecion of the maximum pixel value of the three matrices in one. It searches for the maximum value of the three matrices and then it performs a comparison between the three RGB values of that pixel, if the difference is bigger than 10% (estimated parameter) of the maxmum value it will save it in the new RGB image for that matrix, while for the other matrices the stored value will be null, Fig 4.4, if the values are similar, both values will be stored in their color matrix respectively.

Altought the results of this algorithm could be interpreted as a segmentation, it will provide input for the segmentation step considered. The maximum_intensity_projection gives a color mapping approximation that can be used to define a ROI. In case of Methylene blue-stained tissues, a blue ROI is possible to extract with this algorithm and also consider other areas with blue hue, but assigning them with less significance.

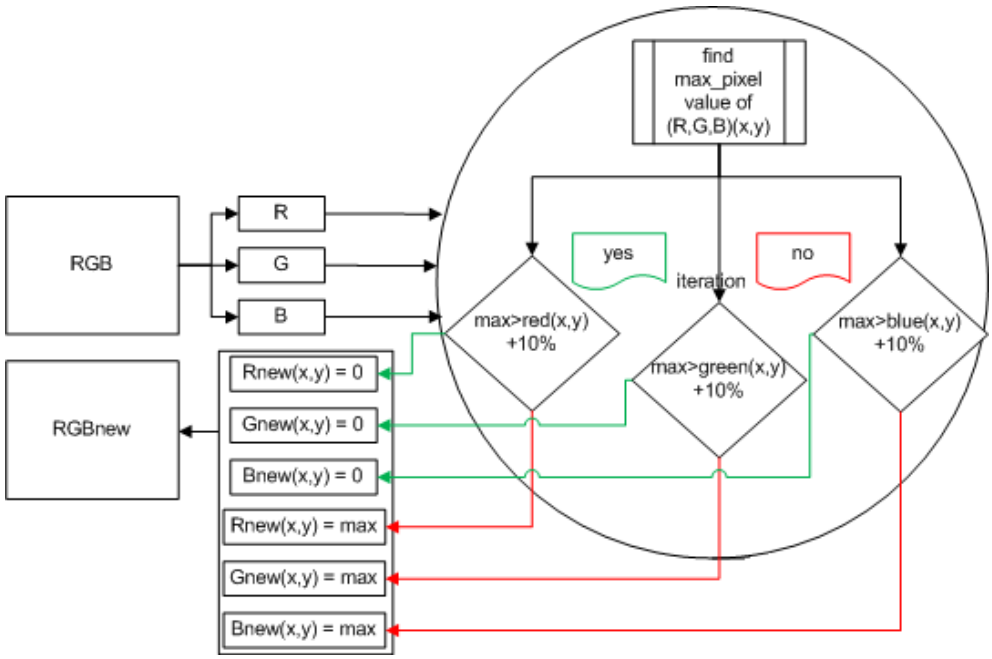

Fig. 4.4: maximum_intensity_projection algorithm.

The glare_removal is a clear example of a feature extraction algorithm, once its purpose is to identify areas of noise caused by light misuse, Fig 4.5. Though this algorithm provides output without the glare, by performing a neighborhood data interpolation, its result is purely visual. Since the original image will not be analyzed as part of a video sequence there is not a possibility to correlate those pixels to the ones in previous or following frames, so the result of this algorithm is not reliable but it will give an idea of the image without glare.

The major output of this algorithm is the glare mask. The glare mask is an image of the pixels that are affected by the misuse of light. This can be used to guide segmentation techniques.

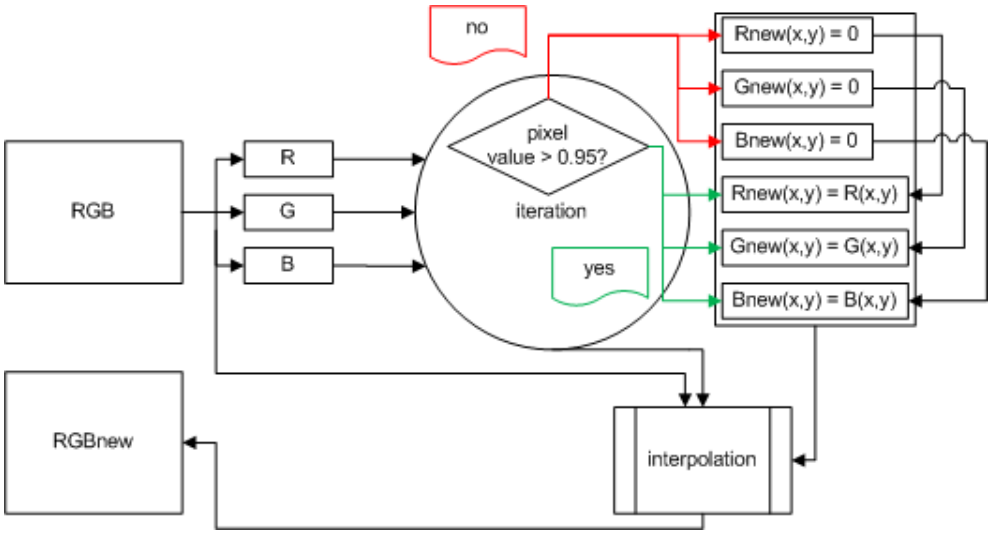

Fig. 4.5: remove_glare algorithm.

The get_contour algorithm is a simple contour-driven process that relies on the Sobel/Prewitt edge detector in all RGB channels and then sums it into one single matrix, the result is given in grayscale. It has maximum values when the edges are coincident in all matrices, Fig 4.6. The result of this algorithm is a grayscale image, with the information of the object borders. Pixel values are in accordance to its relevance in the border.

4.4 Segmentation

The segmentation step is portrayed in Fig 4.7 and is a direct result of the previous steps, their outputs will provide inputs for this process as it has been the case so far. Each phase relies on the output of the previous.

Some methods were developed, iterative_threshold and hybrid ones, others adapted, ACWE and Snakes, so that they can be used for this particular case, the ACF segmenta-

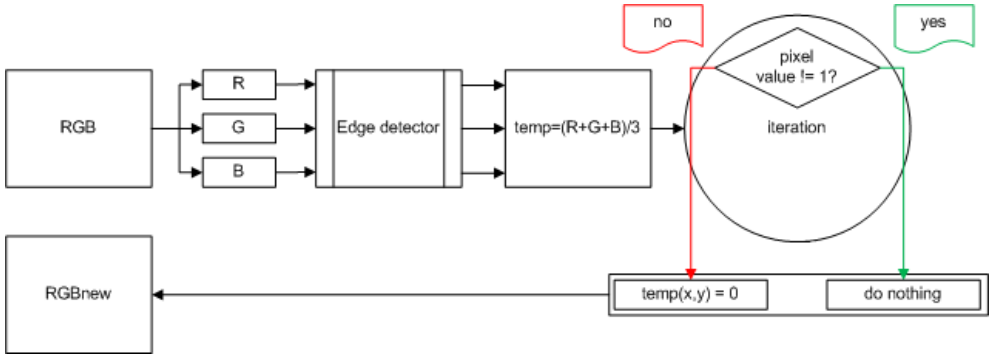

Fig. 4.6: get_contour algorithm.

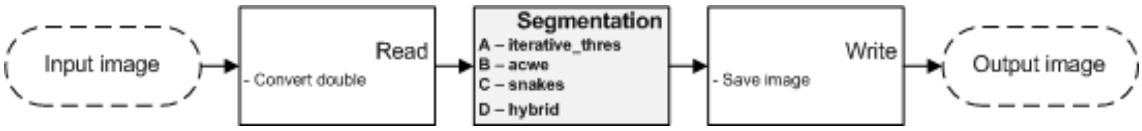

Fig. 4.7: Segmentation flowchart.

tion and its specificities. Segmentation is challenged by round-shape images, camera and patient information embedded in image, the use of different dyes and presence of artifacts.

The iterative_threshold method was developed as an aproximation of multilevel thresholding, it has the ability to perform segmentation in images that have multimodal histograms, Fig 4.8. In addition to have color, the ACF images, have multimodal histograms. This is due to dying, enabling the identification and manual segmentation, perfomed nowadays.

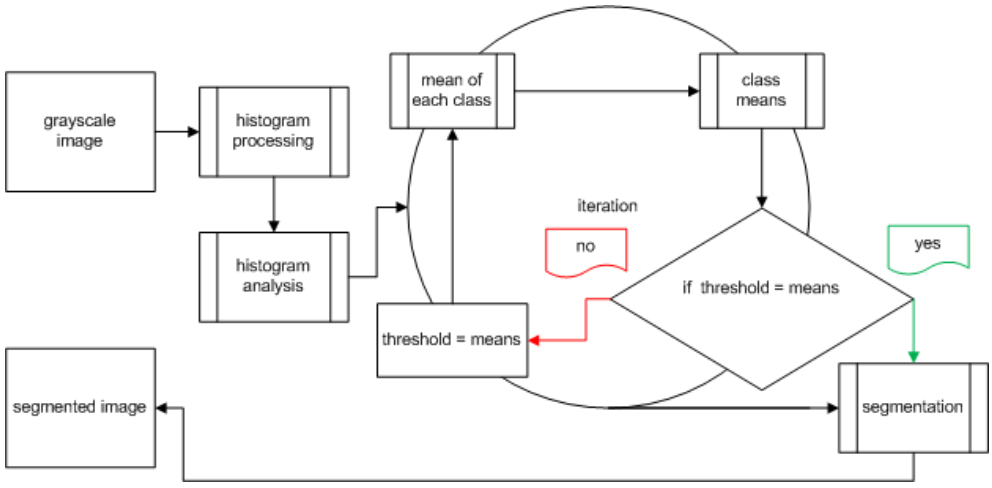

Fig. 4.8: iterative_threshold algorithm.

This algorithm's input is the original image and by histogram analysis it automatically detects the threshold values, perfoming a multi-level segmentation. It has the ability of being used in semi-automatic mode, where the user defines a maximum number of threshold bins. A bin is also considered as a class. Classes are limited by valleys, if an

histogram has only two classes, bimodal, it should only have on threshold value, an ideal Otsu's algorithm application.

An hybrid_acwe method was developed in order to improve segmentation results. The ACWE code was developed by Yue Wu (2009) at Tufts University and it performs the algorithm of Chan and Vese (2001). I have adapted it to the ACF specifications. The input image goes through maximum_intensity_projection and then get_contour algorithms thus obtaining an image that will be used as mask when the ACWE is used in a smoothed initial image, Fig 4.9.

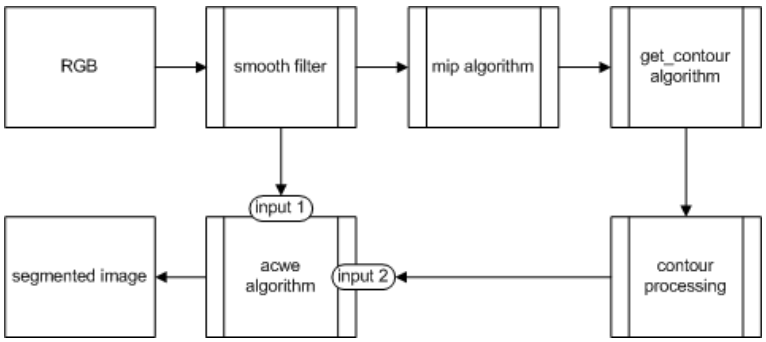

Fig. 4.9: hybrid_acwe algorithm.

Contour processing is required to remove points that are not relevant or not part of the desired contour. Isolated pixels in a given neighborhood will be removed, as well as contour thining by morphological operators.

Providing a mask or initial contour that resembles the original image objects aids the acwe calculation once it will be guided by the maximum_intensity_projection object borders.

Region growing is a segmentation algorithm with a manual value input that is the seed. The algorithm was developed by Dirk-Jan Kroon (2008) at University of Twente following Adams and Bischof (1994). To overcome this user-dependent input an automtic mode was developed, hybrid_region_grow, Fig 4.10.

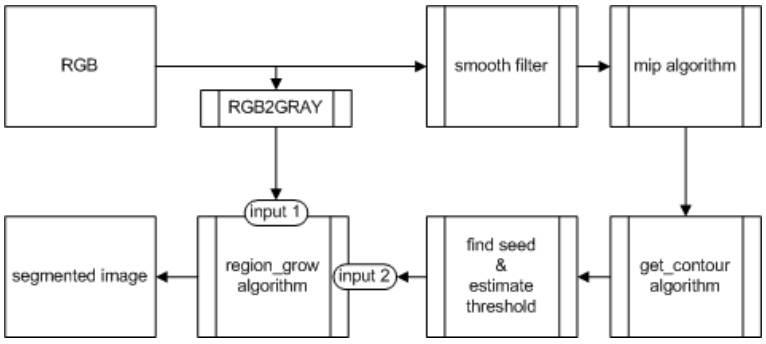

Fig. 4.10: hybrid_region_grow algorithm.

Following the same reasoning as the hybrid_acwe, when in the contour analysis step, in this algorithm a seed will be extracted, using the same principle of how to extract the center of mass of an object. Contour has grayscale pixel values, it will be a weighted mass center. It will be useful if there is a single ACF in image as this algorithm only has the ability to detect one seed. The threshold is given by mean and variance calculations of the grayscale pixel values surrounding the detected seed in the grayscale smoothed image.

A deformable-models was used, the snake coding was developed by Ritwik Kumar (2010) at Harvard University following Kass et al. (1988), in addition to the original image, the algorithm performs a smoothing with a gaussian filter and then it prompts in a GUI (Graphical User Interface) values of α, β, γ, κ, ω_{line}, ω_{edge}, ω_{term}. Initial points of the snake and number of interations is also an input parameter of this algorithm.

4.5 Summary

The purpose of this chapter is to explain the developed algorithms. Some were developed from scratch, others were adapted to meet the ACF specifications. Hybrid algorithms seemed like a proper way of overcoming the difficulties of the ACF segmentation, that is the reason they were developed.

Initial preprocessing aims to remove noise from the image by choosing the best smoothing filter. The feature extraction step provides information about image characteristics, colors, edges and damaged areas. The last phase is the segmentation, the main objective is to segment the ACF present on the image.

The hybrid algorithms developed rely on previous outputs, so it is important to ensure that they are valuable to achieve the main objetive.

Chapter 5

Results & Discussion

5.1 Context

The dataset consists in eight images containing diverse types of ACF configurations, gathered through different methods and medical staff, by colonoscopic techniques with the use of dyes. These images were provided by the ongoing research: UTAustin/MAT/0009/2008 - FCT. This dataset is not homogeneous, six images have evident glare problems, in one of them it is possible to observe air bubbles and seven of them have embedded colonoscope information, Fig 5.1.

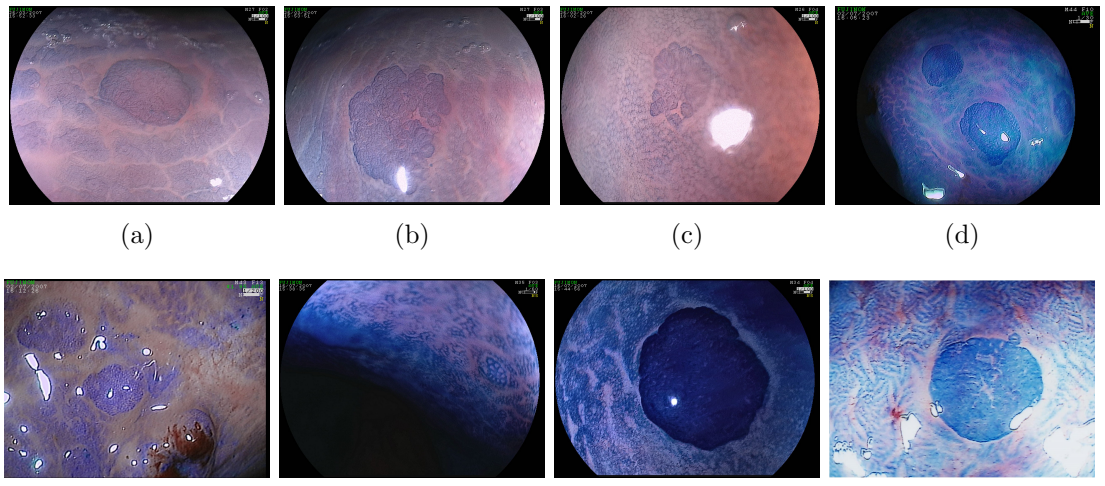

(a) (b) (c) (d)

(e) (f) (g) (h)

Fig. 5.1: Dataset.

5.2 Preprocessing

The algorithms were developed and coded in Matlab® software with the aid of its Image Processing Toolbox. Initially the image was converted to HSV, this way it is possible to perform histogram expansion without tamper real image color, as the expansion is done in the Value channel, responsible for image brightness. With this operation is possible to use the entire histogram range of the initial image before advancing to filter steps. In order to evaluate preprocess step fiability, some statistics as MSE (Mean Square Error) and PSNR (Peak Signal to Noise Ratio) were calculated for each image analyzed, Table 5.1.

Tab. 5.1: Image quality measurements.

Mean Square Error (MSE)	$\frac{1}{MN}\sum_{j=1}^{M}\sum_{k=1}^{N}\left(x_{j,k}-x'_{j,k}\right)^2$
Peak Signal to Noise Ratio (PSNR)	$10\log\frac{255^2}{MSE}$
Normalized Cross-Correlation (NK)	$\sum_{j=1}^{M}\sum_{k=1}^{N} x_{j,k}\cdot x'_{j,k}/\sum_{j=1}^{M}\sum_{k=1}^{N} x_{j,k}^2$
Average Difference (AD)	$\sum_{j=1}^{M}\sum_{k=1}^{N}\left(x_{j,k}-x'_{j,k}\right)/MN$
Structural Content (SC)	$\sum_{j=1}^{M}\sum_{k=1}^{N} x_{j,k}^2/\sum_{j=1}^{M}\sum_{k=1}^{N} {x'_{j,k}}^2$
Maximum Difference (MD)	$Max\left(\left\|x_{j,k}-x'_{j,k}\right\|\right)$
Normalized Absolute Error (NAE)	$\sum_{j=1}^{M}\sum_{k=1}^{N}\left\|x_{j,k}-x'_{j,k}\right\| / \sum_{j=1}^{M}\sum_{k=1}^{N}\left\|x_{j,k}\right\|$

Three smooth filters were used, median and gaussian with differente kernels and anisotropic diffusion. The choice of median filter was made in order to remove speckle noise and provide smoothness once it has the ability to remove salt-and-pepper-like noise as well as border preserving capabilities. Gaussian and anisotropic diffusion were performed in order to obtain the best smoothed image as well as provide comparison between different smoothing filters.

Expansion does not provide smoothing of the image, so it will not be taken into account altought, but it is possible to induce that a simple action as histogram expansion could transform the image completly. Just analyzing the MSE and PSNR values of the expanded column, is possible to deduce that the histogram expansion introduces noise in the image.

Pictures with higher MSE have lower PSNR and vice-versa, a higher value of PSNR is good since it means better signal-to-noise ratio, wich is the final purpose of the image preprocessing or enhancement step.

Maximum diference is a parameter not be considered crucial, once it returns the maximum pixel diference detected between the original image and the preprocessed one. Analyzing the obtained values one could deduce that is linked to the PSNR variation, although when the value of MD is higher the PSNR is lower, wich is not a correct conclusion. A clear example is two black images with same size but one of them has a white pixel, in this case both PSNR and MD will be high.

NK values reflects how much the images are shifted as if they were two waveforms. This is used for finding small parts of an image which match a template image. The closer to one the more similiar the images are.

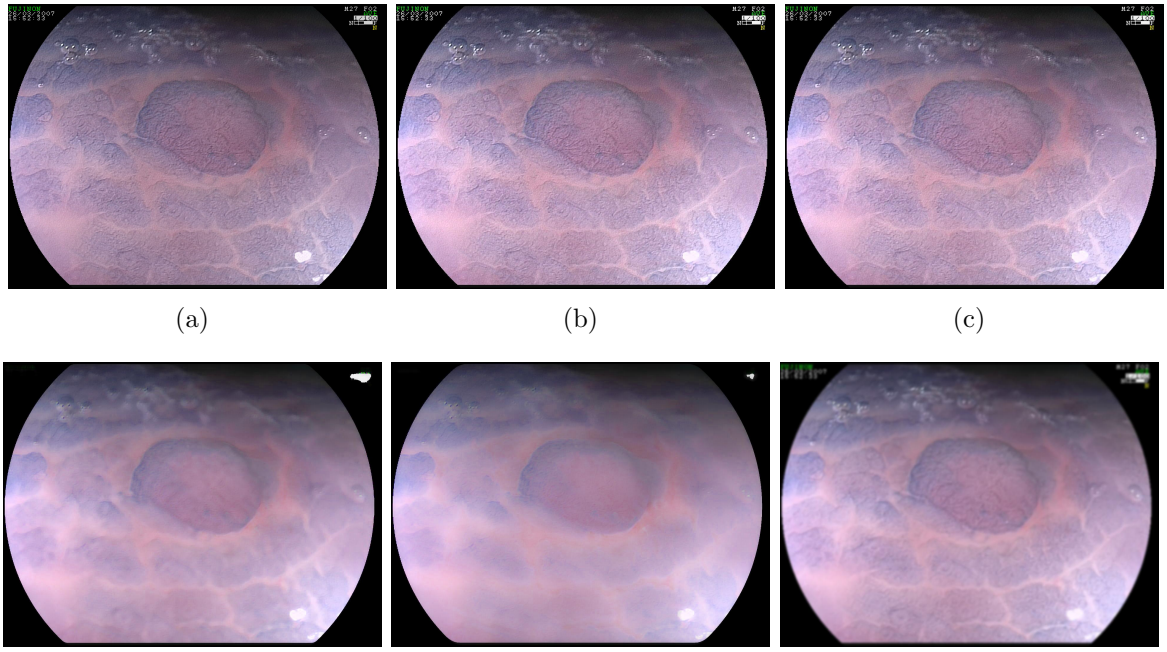

(a) (b) (c)

(d) (e) (f)

Fig. 5.2: Image a: Original image (a), expanded (b), gaussian filter kernel size 17 (c), median filter kernel size 21 (d), 50 (e) and anisotropic diffusion (f).

Tab. 5.2: Image (a) statistics.

Image (a)	expanded	anisoff	median 17	median 21	median 50	gaussian 17
MSE	427,4843	536,1290	553,2505	556,2271	587,8939	427,0727
PSNR	21,8216	20,83815	20,7016	20,6783	20,4378	21,8258
NK	1,1661	1,1531	1,1566	1,1561	1,1500	1,1646
AD	-18,1242	-18,0663	-17,6276	-17,5910	-17,0327	-18,1108
SC	0,7353	0,7456	0,7412	0,7416	0,7472	0,7369
MD	14	198	239	235	250	66
NAE	0,1672	0,1767	0,1721	0,1722	0,1728	0,1675

In Fig 5.2, with the help of Table 5.2, it is possible to verify that the expanded image is brighter than the original image. Also anisotropic diffusion and gaussian filtering provide a good PSNR. The higher the median kernel size is the more blurred is the image, as expected.

For the Fig 5.3, the median fiter with size 17 and 21 have little difference values, but the difference between 21 and 50 has a higher ratio than in the previous image, Fig 5.2. The same happens to all the other values. PSNR and MSE values for median filters are

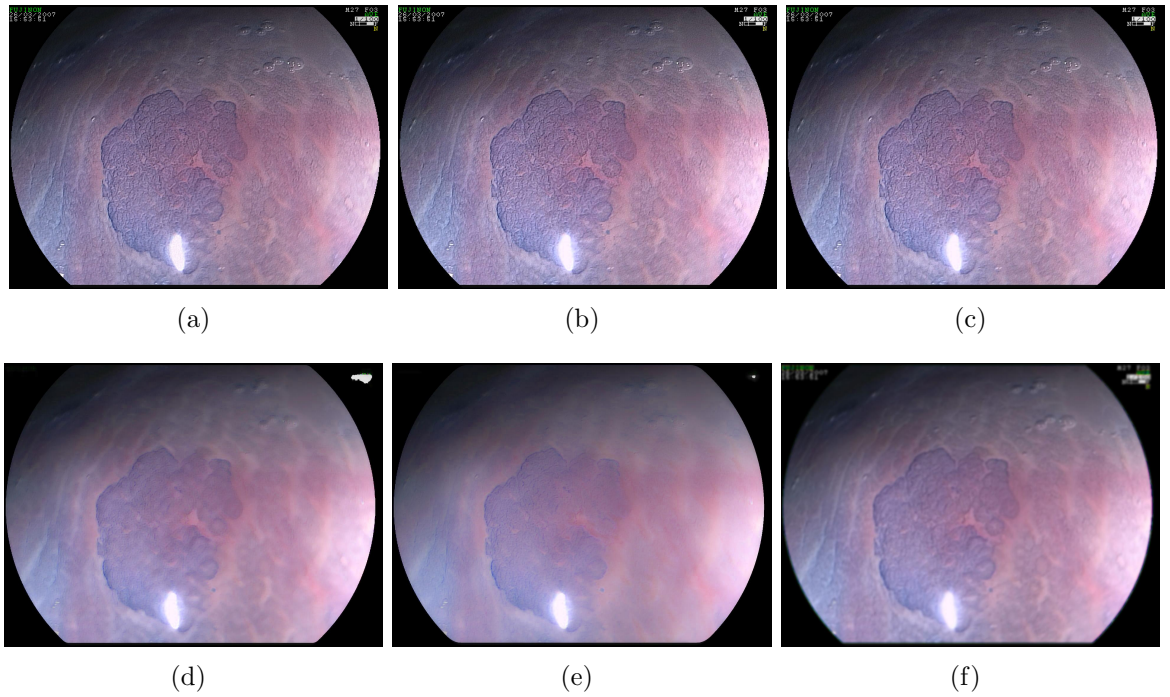

(a) (b) (c)

(d) (e) (f)

Fig. 5.3: Image b: Original image (a), expanded (b), gaussian filter kernel size 17 (c), median filter kernel size 21 (d), 50 (e) and anisotropic diffusion (f).

Tab. 5.3: Image (b) statistics.

Image (b)	expanded	anisoff	median 17	median 21	median 50	gaussian 17
MSE	111,8283	242,7766	246,0504	249.0088	290,0893	113,7464
PSNR	27,6453	24,2787	24,2206	24.1687	23,5055	27,5714
NK	1,0902	1,0738	1,0793	1.0787	1,0716	1,0882
AD	-8,9633	-8,7479	-8,5577	-8.5153	-7,9315	-8,9077
SC	0,8412	0,8578	0,8495	0.8502	0,8584	0,8440
MD	20	200	237	239	244	76
NAE	0,0914	0,1079	0,1014	0.1016	0,1037	0,0921

twice the other values, Table 5.3. The gaussian kernel 17 seems a better choice in this image, although it does not remove salt and pepper noise better than the median filter and it does smooth edges.

At Fig 5.4 is possible to analyze that even smoothed by a gaussian kernel the original image and the smoothed one are very similiar, with low MD, probably due to the presence of a relatively big glare area in the orginal image. Higher smoothing increases glare aberration, Table 5.4.

The PSNR for the median filter kernel size 17 and 21 had a higher value than the one for anisotropic diffusion, Fig 5.5, wich had not happen yet with the previous images, Table 5.5.

In Fig 5.6 the image gets easily blurred, from median filter application. In this image

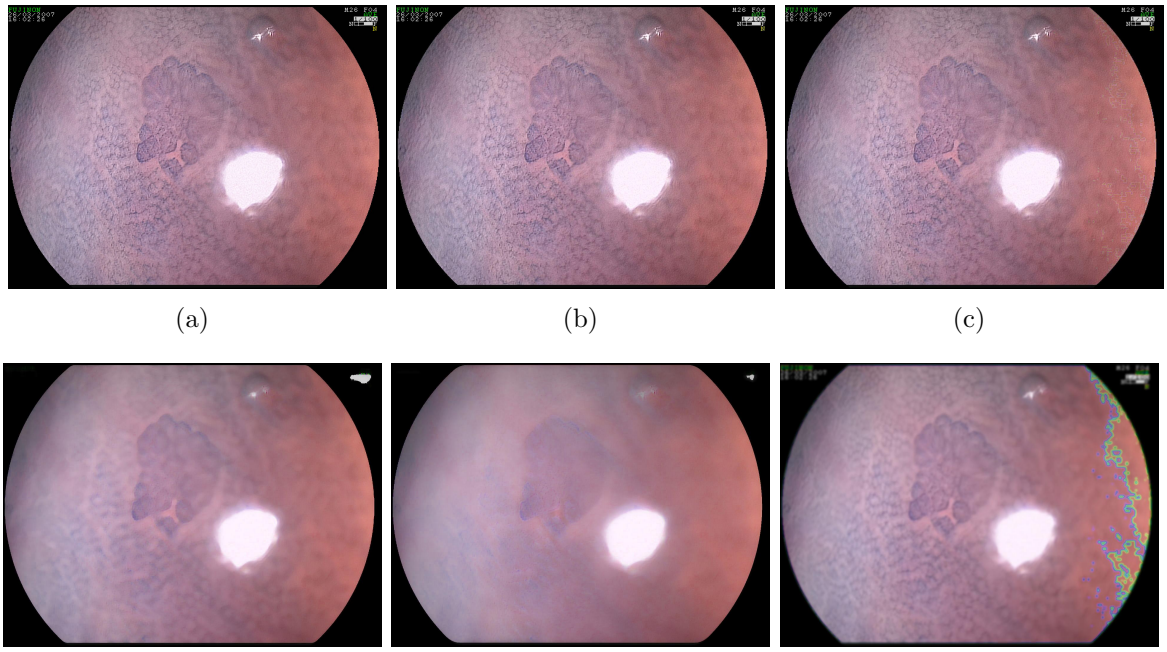

(a) (b) (c)

(d) (e) (f)

Fig. 5.4: Image c: Original image (a), expanded (b), gaussian filter kernel size 17 (c), median filter kernel size 21 (d), 50 (e) and anisotropic diffusion (f).

Tab. 5.4: Image (c) statistics.

Image (c)	expanded	anisoff	median 17	median 21	median 50	gaussian 17
MSE	5,2049	144,2074	132,1954	137,2005	184,3902	14,6925
PSNR	40,9667	26,5409	26,9186	26,7572	25,4734	36,4598
NK	1,0135	1,0075	1,0089	1,0086	1,0038	1,0133
AD	-1,5374	-1,9380	-1,4346	-1,4190	-0,9355	-1,6431
SC	0,9734	0,9773	0,9753	0,9756	0,9821	0,9734
MD	18	201	235	236	236	68
NAE	0,0154	0,0514	0,0414	0,0428	0,0503	0,0183

the median filter is able to minimize the glare, it will not be necessary to use remove_glare algortihm for this case. The statistics show that the anisotropic diffusion algorithm has almost the same values as the median filter with kernel size 50, Table 5.6.

In the Fig 5.7 median filters and anistropic diffusion have similar values, which becomes acceptable due to the big dark area in the bottom of the image caused by poor light conditions, Table 5.7.

Anisotropic diffusion once again gets PSNR values lower than median filtering. In this case even the gaussian filter has higher PSNR value than the result from the histogram expansion, Fig 5.8. It is possible to analyze the data in Table 5.8.

On the last Fig 5.9, values for PSNR are very similar between the different output results, Table 5.9. Either gaussian or median filter with kernel size 17 provide efficient

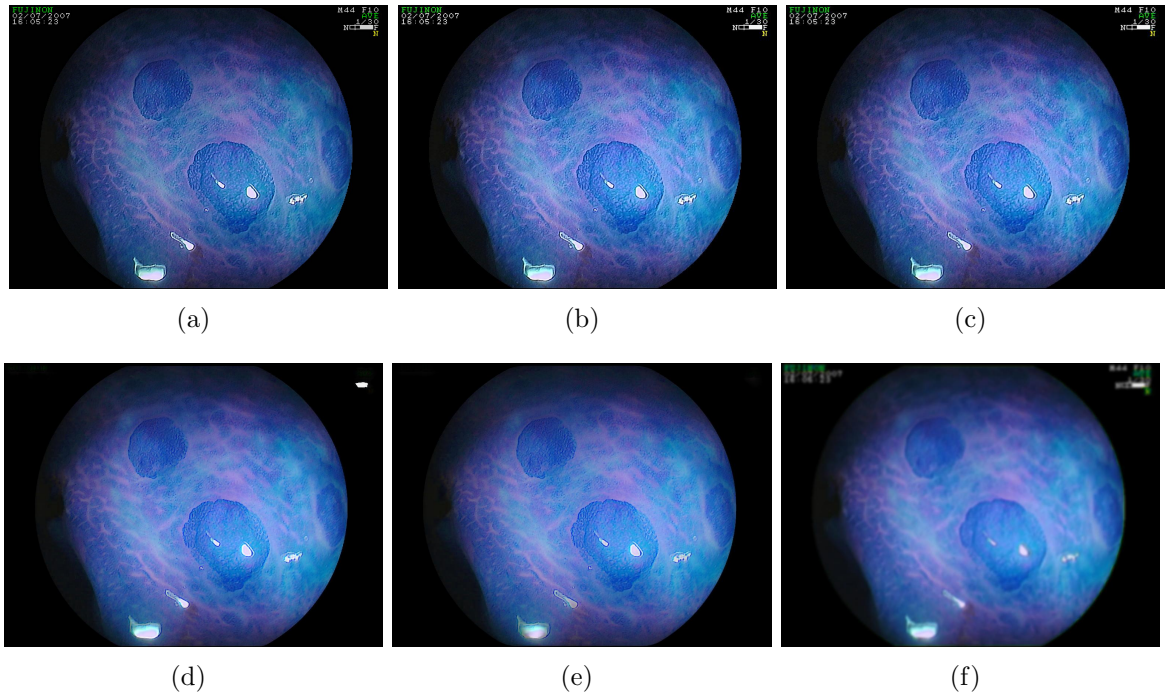

(a) (b) (c)

(d) (e) (f)

Fig. 5.5: Image d: Original image (a), expanded (b), gaussian filter kernel size 17 (c), median filter kernel size 21 (d), 50 (e) and anisotropic diffusion (f).

Tab. 5.5: Image (d) statistics.

Image (d)	expanded	anisoff	median 17	median 21	median 50	gaussian 17
MSE	149,8181	291,7886	280,7334	282,5428	303,6931	147,4541
PSNR	26,8321	23,4801	23,6479	23,6200	23,3065	26,4442
NK	1,1700	1,1189	1,1310	1,1292	1,1139	1,1630
AD	-8,7027	-8,3642	-7,8448	-7,7845	-7,2739	-8,6267
SC	0,7297	0,7708	0,7580	0,7599	0,7754	0,7374
MD	19	206	228	228	228	65
NAE	0,1785	0,2041	0,1898	0,1897	0,1910	0,1782

smoothing.

For the following steps (feature extraction and segmenation) the input images will be smoothed with a median filter, kernel size twenty-one, this provides acceptable smoothing, shown by statistics, and also the ability to remove speckle noise and preserve edges.

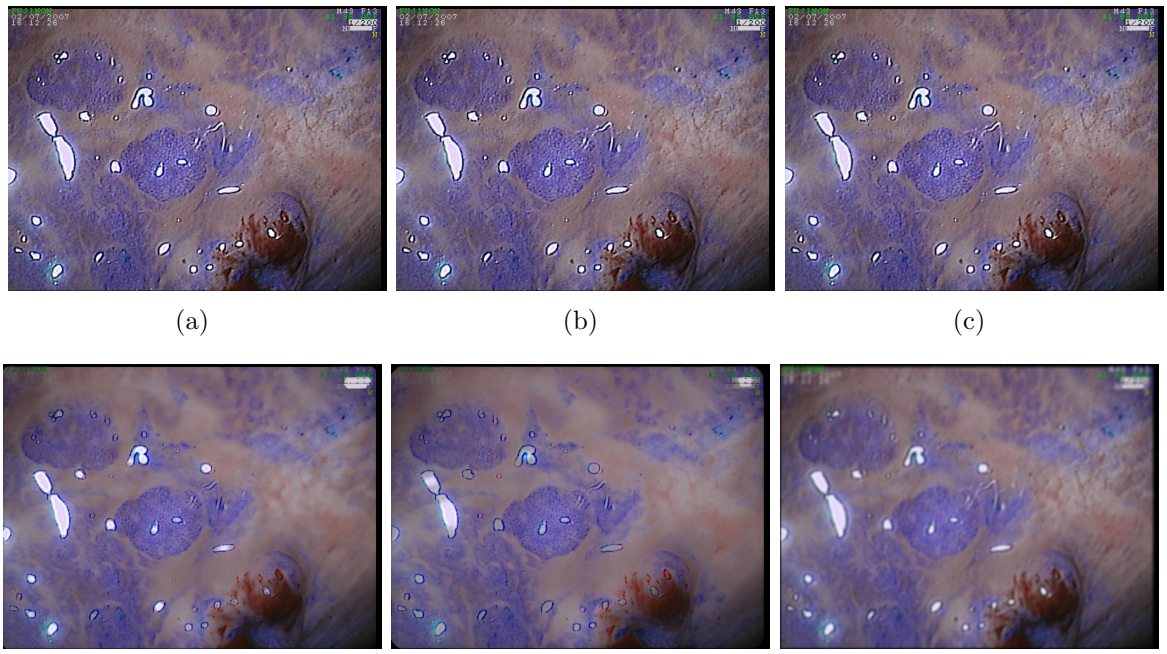

(a) (b) (c)

(d) (e) (f)

Fig. 5.6: Image e: Original image (a), expanded (b), gaussian filter kernel size 17 (c), median filter kernel size 21 (d), 50 (e) and anisotropic diffusion (f).

Tab. 5.6: Image (e) statistics.

Image (e)	expanded	anisoff	median 17	median 21	median 50	gaussian 17
MSE	2,4771	268,7279	185,7883	196,2895	283,9764	7,0812
PSNR	44,1914	23,8377	25,4406	25,2018	23,5980	39,6297
NK	1,0081	0,9768	0,9844	0,9813	0,9606	1,0058
AD	-0,7891	-0,4246	-0,2440	-0,0611	1,3093	-0,7547
SC	0,9838	1,0240	1,0154	1,0211	1,0576	0,9880
MD	19	203	215	217	220	66
NAE	0,0113	0,0819	0,0673	0,0705	0,0869	0,0141

Tab. 5.7: Image (f) statistics.

Image (f)	expanded	anisoff	median 17	median 21	median 50	gaussian 17
MSE	46,5095	136,3597	135,7815	137,9742	147,6897	47,8241
PSNR	31,4554	26,7839	26,8024	26,7328	26,4373	31,3343
NK	1,1071	1,0668	1,0746	1,0733	1,0632	1,1015
AD	-4,4913	-4,3268	-3,8923	-3,8695	-3,6001	-4,4513
SC	0,8155	0,8554	0,8442	0,8457	0,8586	0,8228
MD	14	197	236	236	236	67
NAE	0,1049	0,1330	0,1174	0,1182	0,1200	0,1060

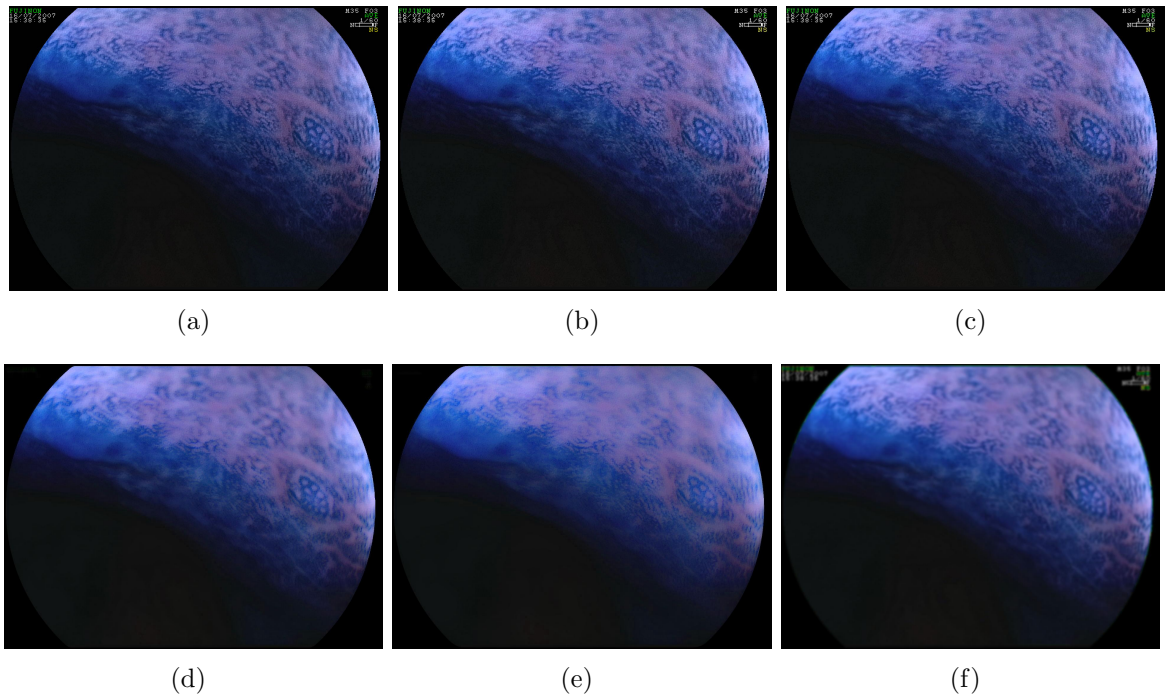

(a) (b) (c)

(d) (e) (f)

Fig. 5.7: Image f: Original image (a), expanded (b), gaussian filter kernel size 17 (c), median filter kernel size 21 (d), 50 (e) and anisotropic diffusion (f).

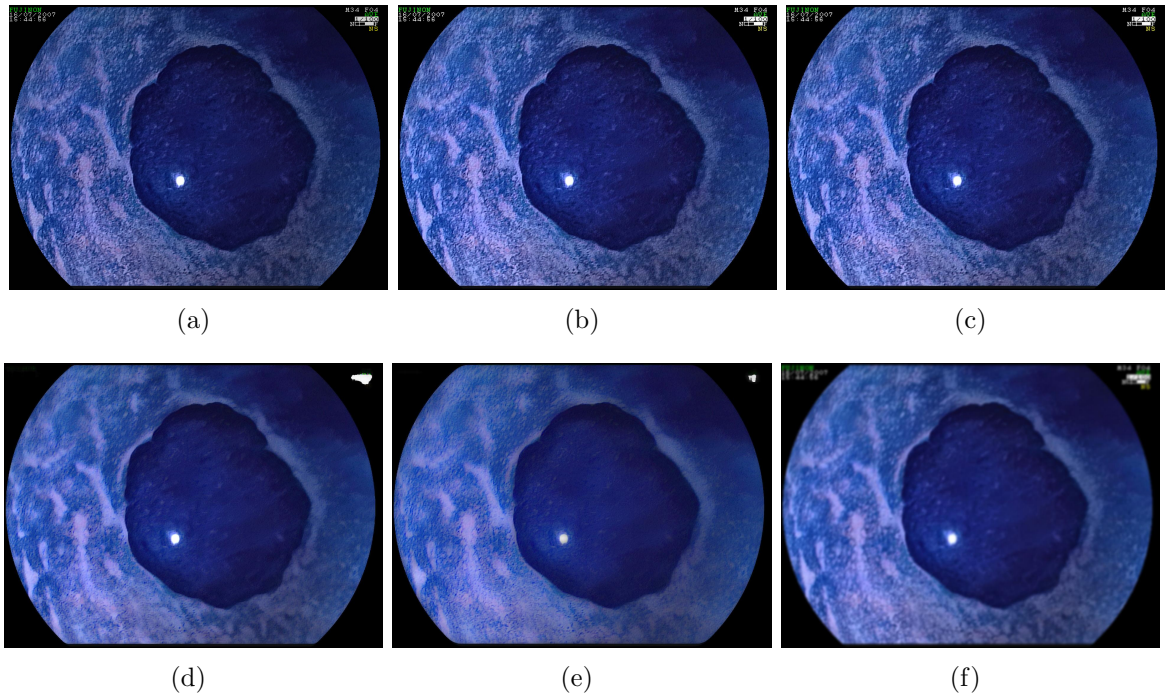

(a) (b) (c)

(d) (e) (f)

Fig. 5.8: Image g: Original image (a), expanded (b), gaussian filter kernel size 17 (c), median filter kernel size 21 (d), 50 (e) and anisotropic diffusion (f).

Tab. 5.8: Image (g) statistics.

Image (g)	expanded	anisoff	median 17	median 21	median 50	gaussian 17
MSE	135,3550	268,1142	229,8925	230,5015	244,1384	132,9637
PSNR	26,8161	23,8476	24,5156	24,5041	24,2544	26,8935
NK	1,1847	1,1250	1,1260	1,1214	1,0869	1,1787
AD	-9,2045	-9,1446	-8,0301	-7,9018	-6,9042	-9,1878
SC	0,7121	0,7581	0,7625	0,7678	0,8085	0,7186
MD	12	197	235	235	236	42
NAE	0,1880	0,2194	0,1879	0,1874	0,1860	0,1883

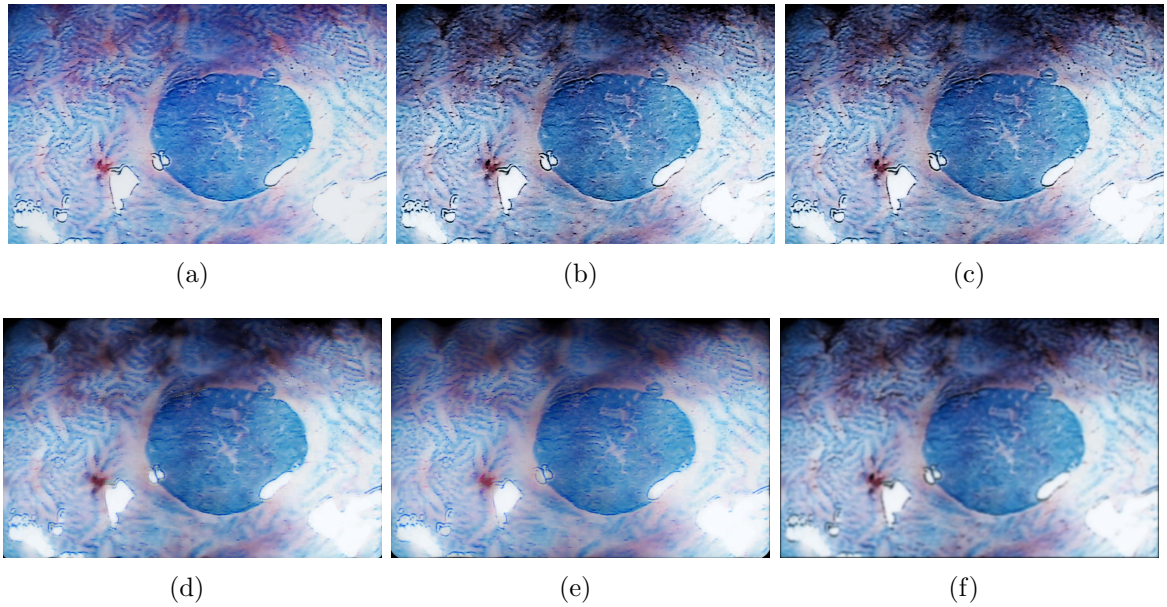

(a) (b) (c)

(d) (e) (f)

Fig. 5.9: Image h: Original image (a), expanded (b), gaussian filter kernel size 17 (c), median filter kernel size 21 (d), 50 (e) and anisotropic diffusion (f).

Tab. 5.9: Image (h) statistics.

Image (h)	expanded	anisoff	median 17	median 21	median 50	gaussian 17
MSE	559,5535	739,8477	608,9652	617,9869	669,5752	552,8255
PSNR	20,6524	19,4394	20,2849	20,2210	19,8728	20,7049
NK	0,9372	0,9203	0,9374	0,9369	0,9312	0.9362
AD	15,4399	16,6034	14,2869	14,3122	15,1244	15,5104
SC	1,1160	1,1504	1,1131	1,1140	1,1258	1,1187
MD	108	202	209	209	231	90
NAE	0,1204	0,1341	0,1222	0,1229	0,1260	0,1200

5.3 Feature Extraction

The remove_glare results are shown in Fig 5.10 and Fig 5.11, while the output result is merely cosmetic, because the interpolation introduces estimated pixel values in glare areas, its second output, the glare mask, is relevant to discard areas where the glare is affecting the acquired image.

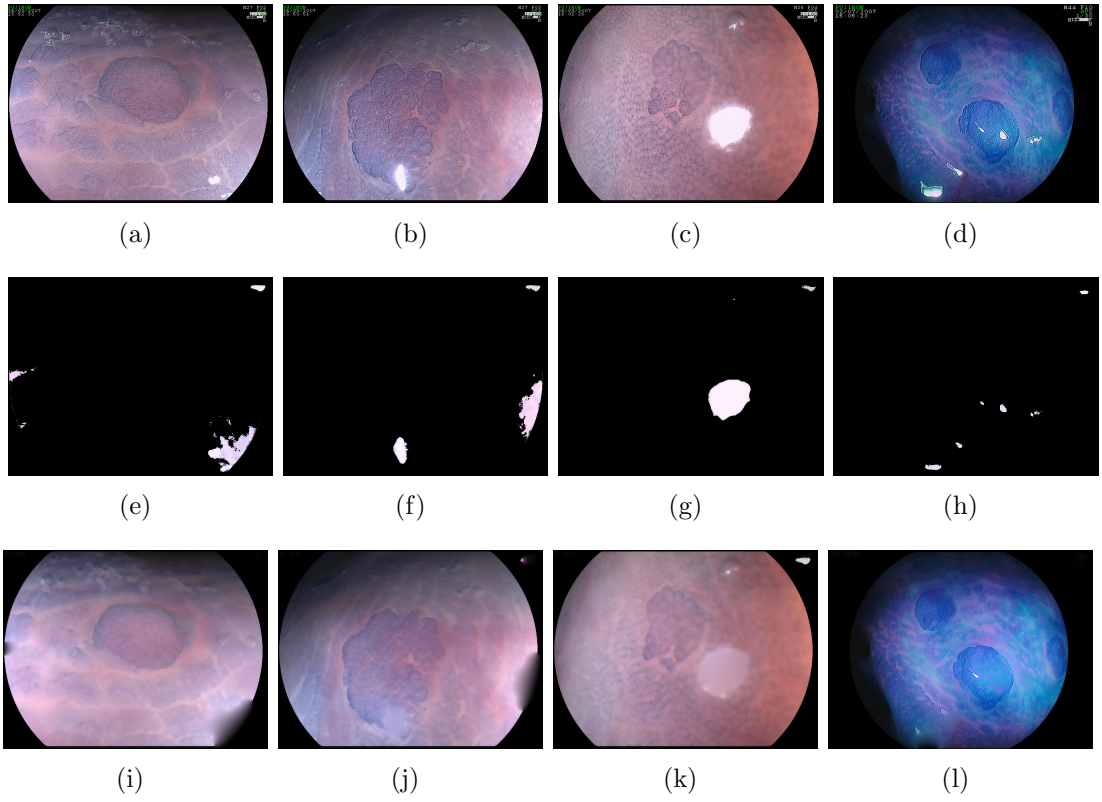

Fig. 5.10: Input image (first row), glare mask (second row) and remove_glare output (last row).

The maximum_intensity_algorithm as previously explained, results in a ROI, that is differentiated in color, as if it were a segmentation output already. Though its output may be interpreted as a color segmented image, it will not be analyzed as such.

For the set of images, Fig 5.12, first two rows, the mip did not detect properly the predominance of blue color present in the stained ACF. The blue color predominance was detected far from the ACF in the first two images, as for the third it did not detect at all. In the forth image the blue spectrum dominates the picture. For all second row outputs in Fig 5.12 a ROI was not possible to extract. Over-staining was possible to identify in Fig 5.12(d).

At Fig 5.12, last two rows, for the first case, the algorithm was able to detect possible ROI areas in blue, the ACF responds to methylene blue staining, which sugests that blue areas could possibly be lesions caused by or the ACF itself.

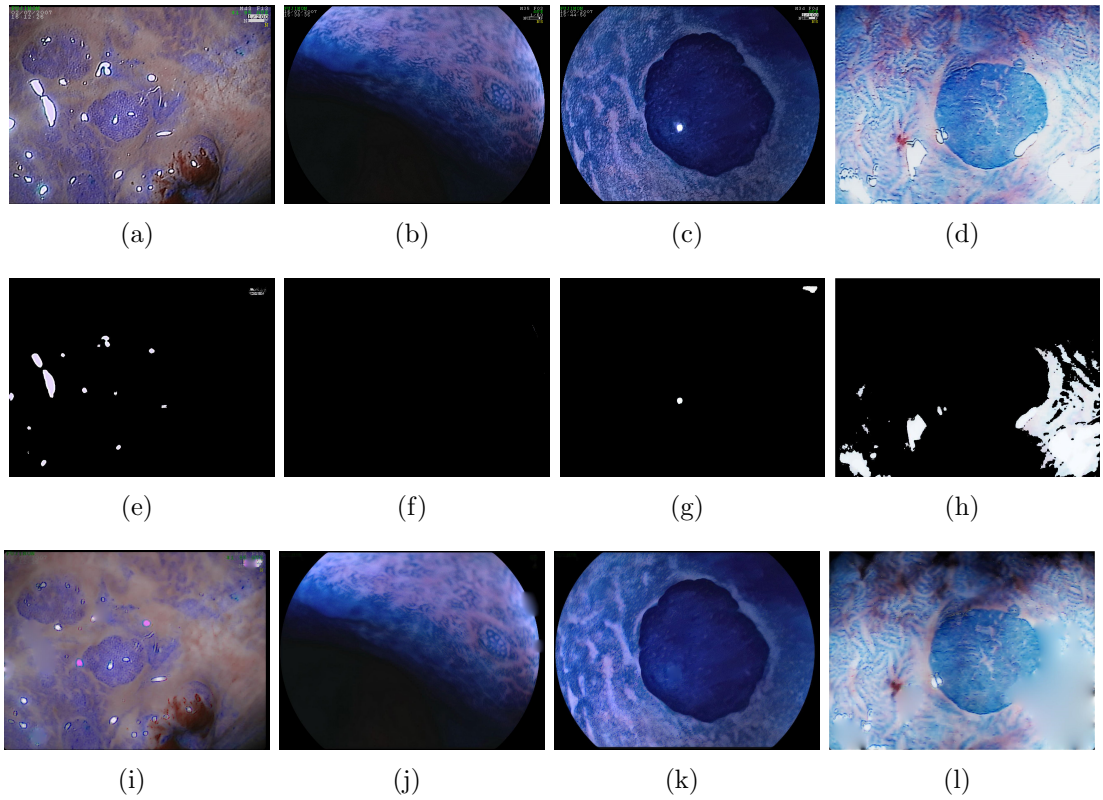

Fig. 5.11: Input image (first row), glare mask (second row) and remove_glare output (last row).

In the last case of Fig 5.12 mip was able to identify a ROI containing the ACF, but also surrounding tissue that was also colored with the methylene blue dye.

This algorithm will easly detect predominant colors in an image, but if the image as already a predominant color it is unnecessary to apply, since the output will be almost as equal as the input. This algorithm will be applied in the segmentation steps, as they provide information that help segmentation process.

The get_contour algorithm when compared to the laplacian edge detector, outputs better visual results. Although it may have noise, it is possible to filter some of the speckle noise of the image. This is due to previous smoothing step, lower smoothing will reflect more noise, while higher smoothing will degrade the object edges, decreasing the efficiency of the get_contour algorithm as well as other contour detectors.

This algorithm consists on a edge detector, Sobel, Prewitt or Canny. It detects the edges in the three RGB channels and later it correlates the information of them into one single image.

The presence of glare clearly manifests on the results of both filters used, laplacian or get_contour. Once they are treated as objects, both algorithms provide their edges and as for the ACF in the image it is not possible to obtain relevant information about their edges, Fig 5.13, Fig 5.14, Fig 5.15 and Fig 5.16.

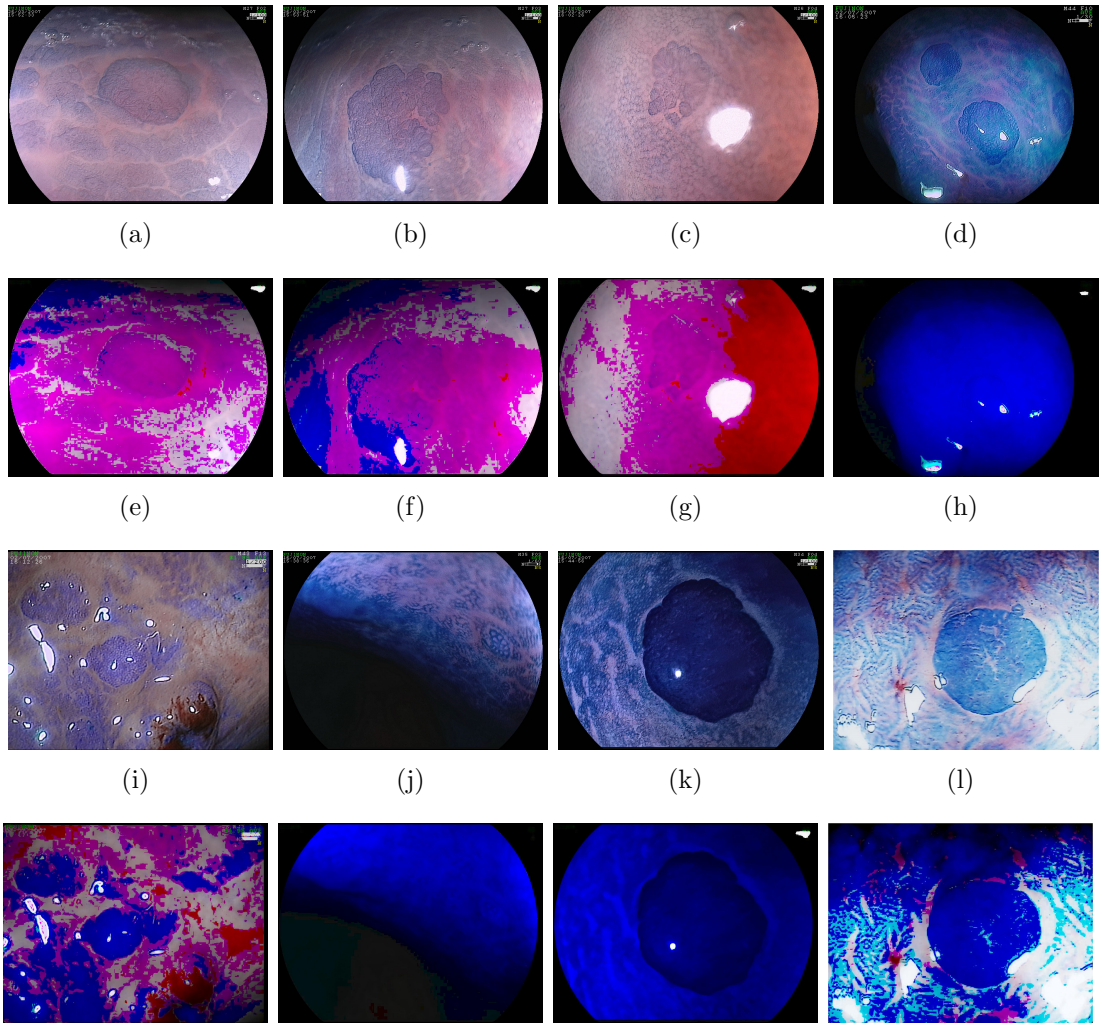

Fig. 5.12: Input image (first and third rows) and maximum_intensity_projection output (second and last rows).

In Fig 5.13 and Fig 5.14, the laplacian output is barely noticeable as well as the get_contour, for the first three images, once their edges are smoothed. In the forth image, it is possible to have better outputs, when in comparison to previous results.

The results in Fig 5.15 and Fig 5.16 are more perceptible for either filters. Altough, get_contour seems to have better results, it still has noise that could compromise future usage of these outputs in segmentation process. Using morphological filters it is possible to decrease by removing isolated pixels or link both ends of a contour.

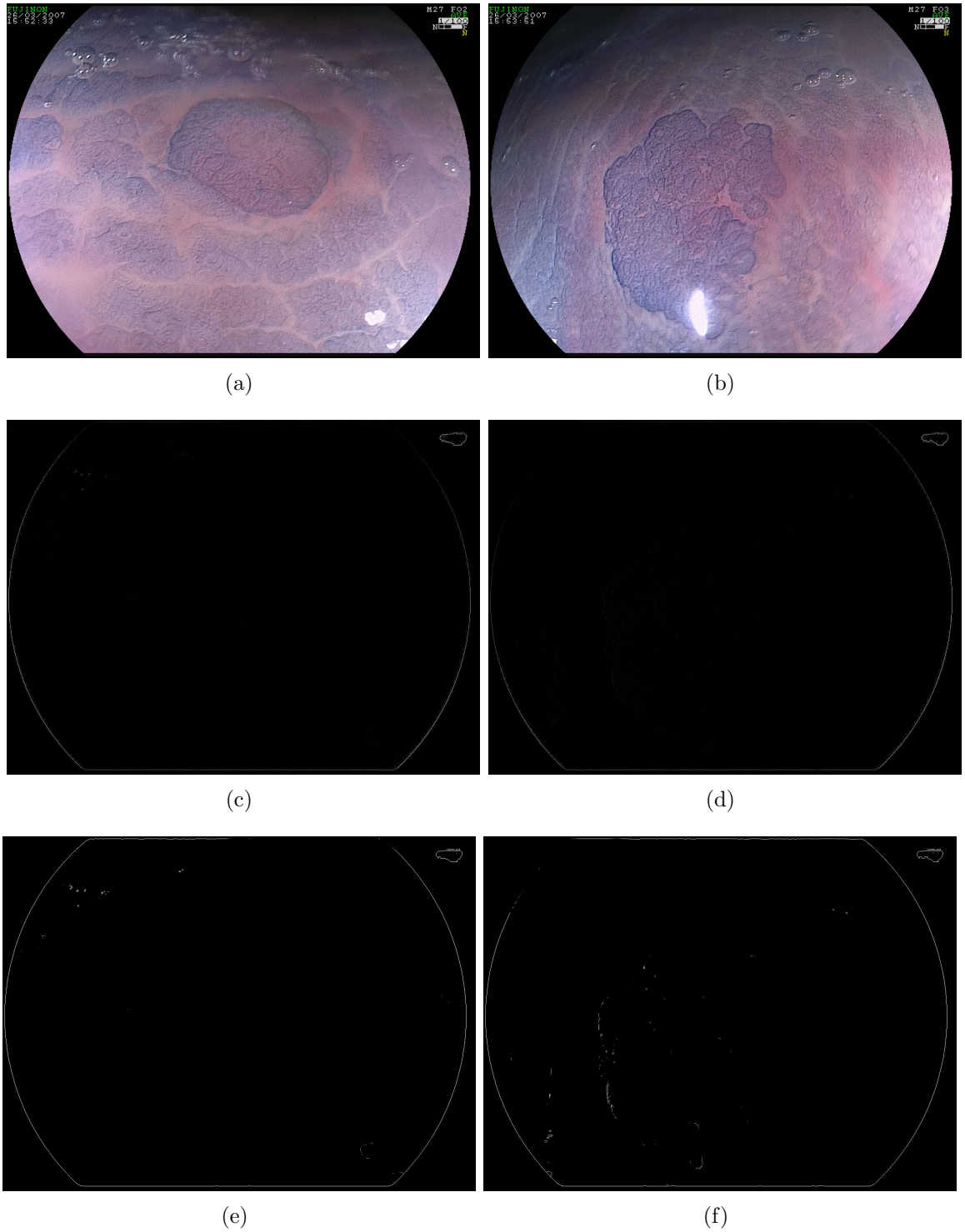

(a) (b)

(c) (d)

(e) (f)

Fig. 5.13: Input image (first row), laplacian filter (second row) and get_contour output (third row).

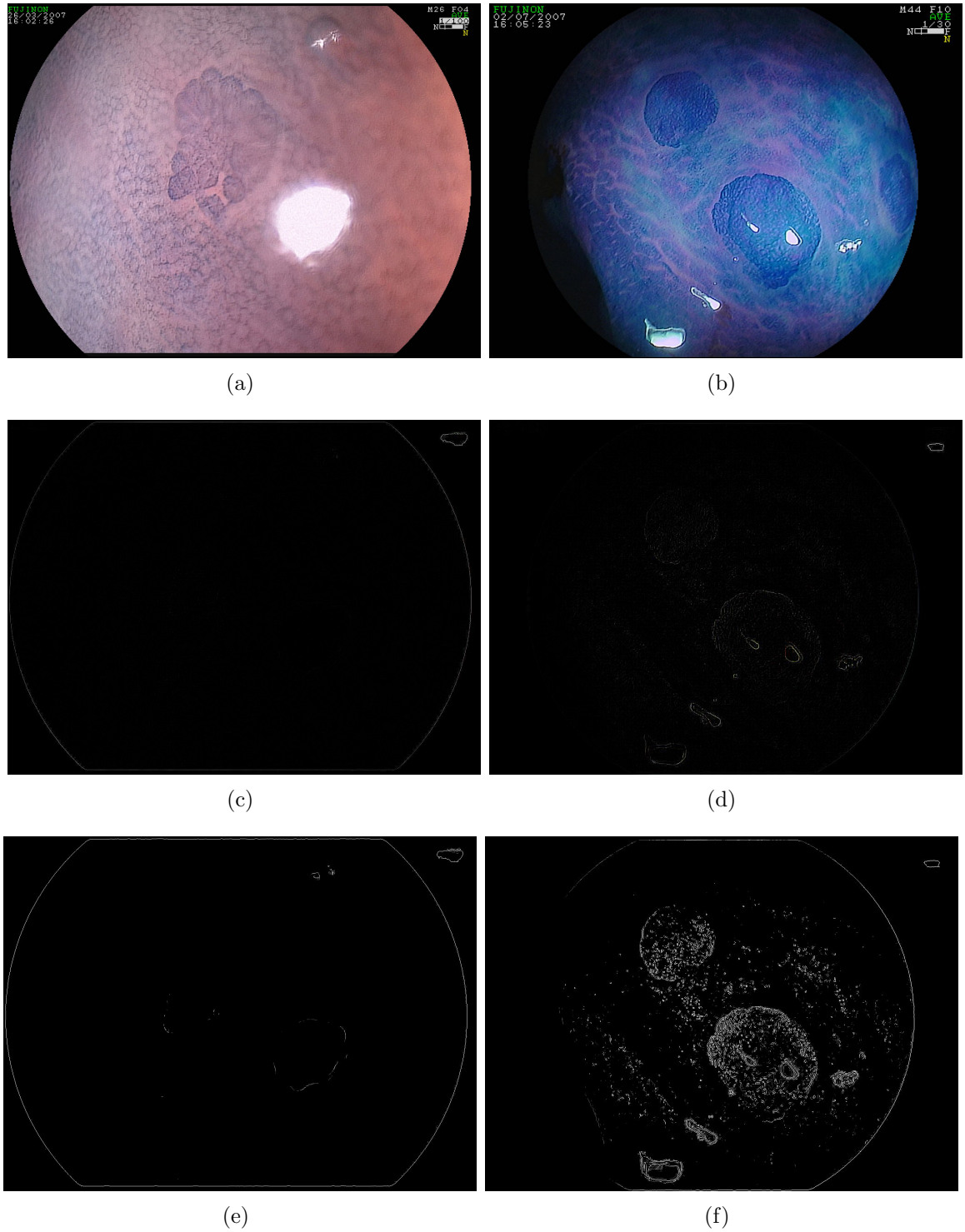

(a) (b)

(c) (d)

(e) (f)

Fig. 5.14: Input image (first row), laplacian filter (second row) and get_contour output (third row).

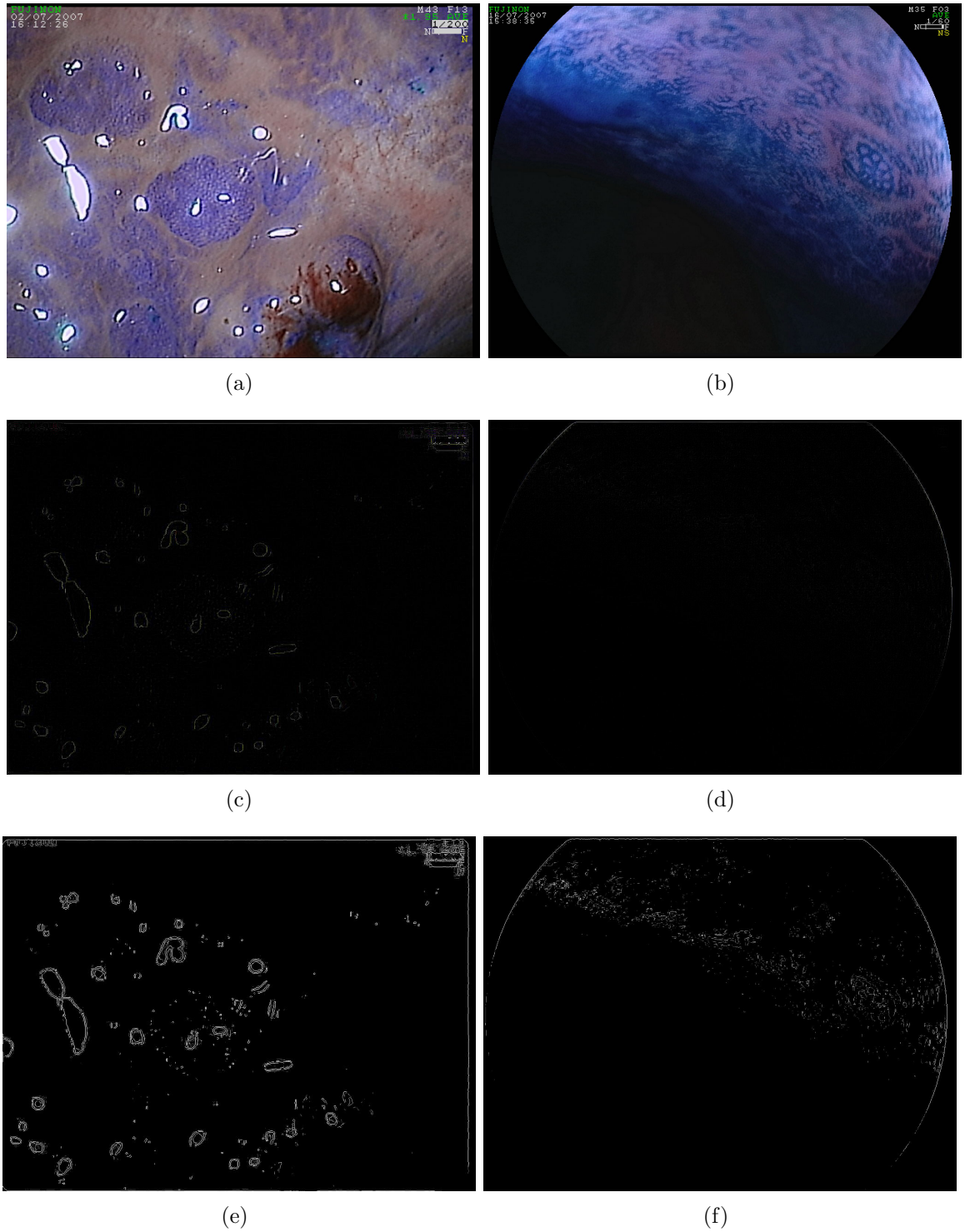

(a) (b)

(c) (d)

(e) (f)

Fig. 5.15: Input image (first row), laplacian filter (second row) and get_contour output (third row).

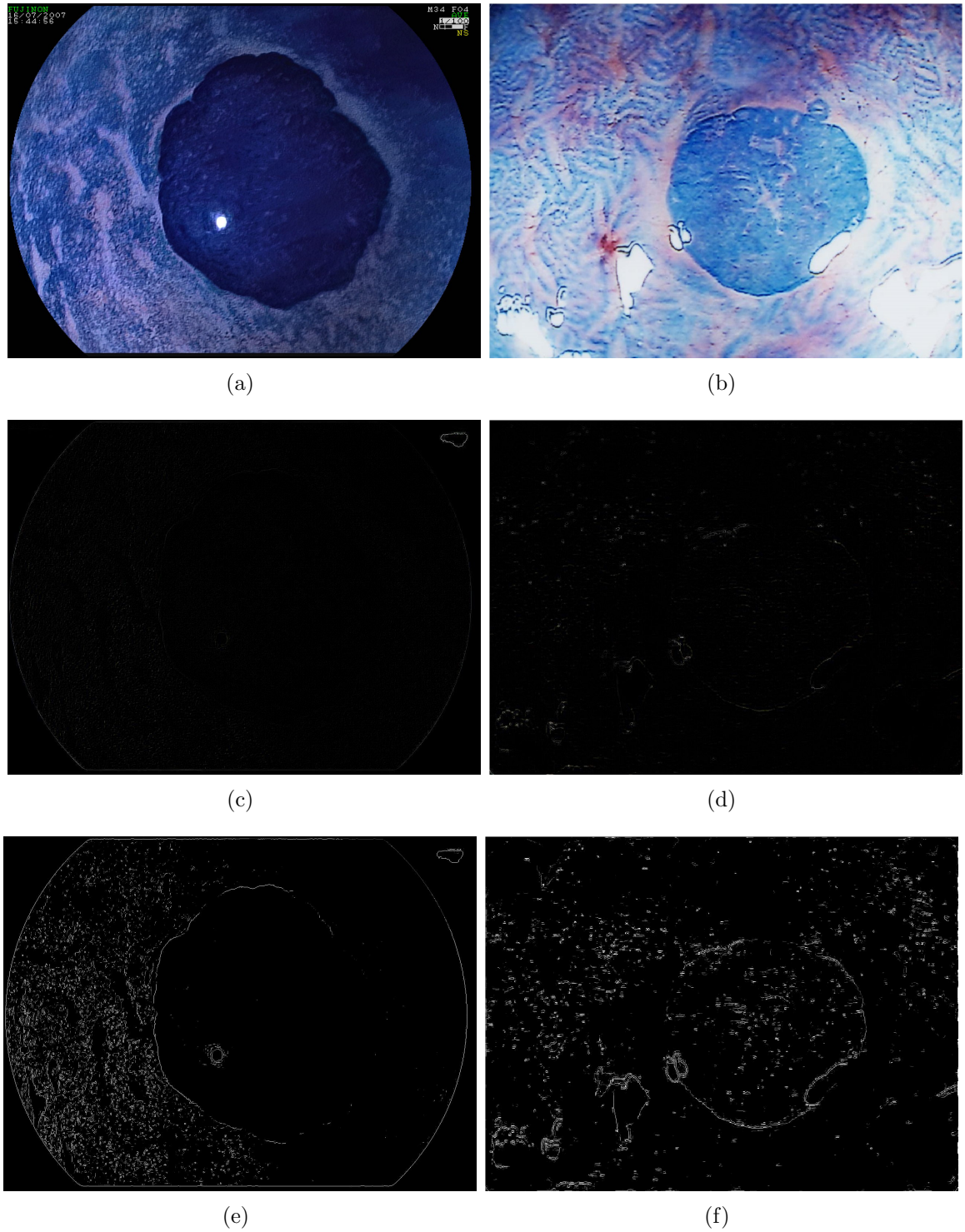

(a) (b)

(c) (d)

(e) (f)

Fig. 5.16: Input image (first row), laplacian filter (second row) and get_contour output (third row).

5.4 Segmentation

In this phase, all outputs will be considered as inputs, in order to achieve the best result possible. The iterative_threshold only accepts grayscale input images so any input must be converted to grayscale, even the mip outputs wich provide color mapping, Fig 5.17 and Fig 5.18. For this algorithm, the median filter output was used.

In both images, it was not possible to verify segmentation of the ACF present in each case image with this algorithm. The maximum_intensity_algorithm has better results, converting the image to grayscale results in losing valuable information about the colorspace. Also, with an original image so color homogeneous it would be dificult for a color algorithm to segment the ACF, as its color is the same as the background, wich makes difficult to sort foreground from background, Fig 5.17(d) and Fig 5.18(c).

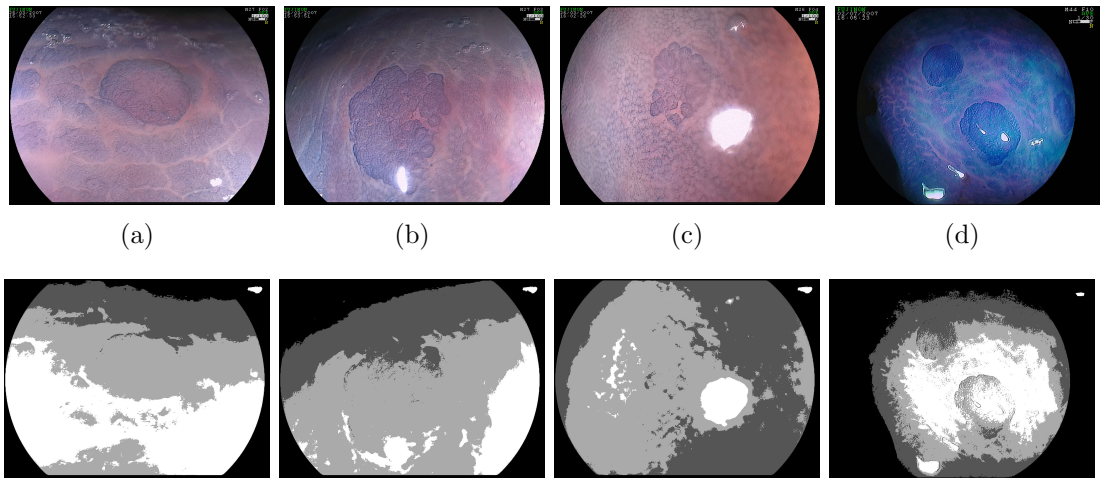

Fig. 5.17: Input image (first row) and iterative_threshold output (last row).

Snakes is a deformable model that converges to a contour, in this case the ACF contour. This was applied manually, input values and initial contour were inserted, Table 5.10 for each case image, some of the values were used by Alves (2011).

It was not possible to segment the ACF, that is due to the intial snake contour selected, once Alves (2011) obtained better results with some of the values used. Although it could be a direct consequence of an erroneous initial smoothing, Fig 5.19 and Fig 5.20.

This is a valuable algorithm if each images has only one ACF, which is not the case for this dataset. So, it was only applied to the images where this occurs most evidently.

The ACWE model was also tested, input parameters are the image, μ, mask type and number of iterations. Different values of μ and mask types were used to adapt to ACF specifications. The ACWE algorithm is able to detect contours even in highly smoothed images. The input images of this algorithm will be the output images of the preprocessing

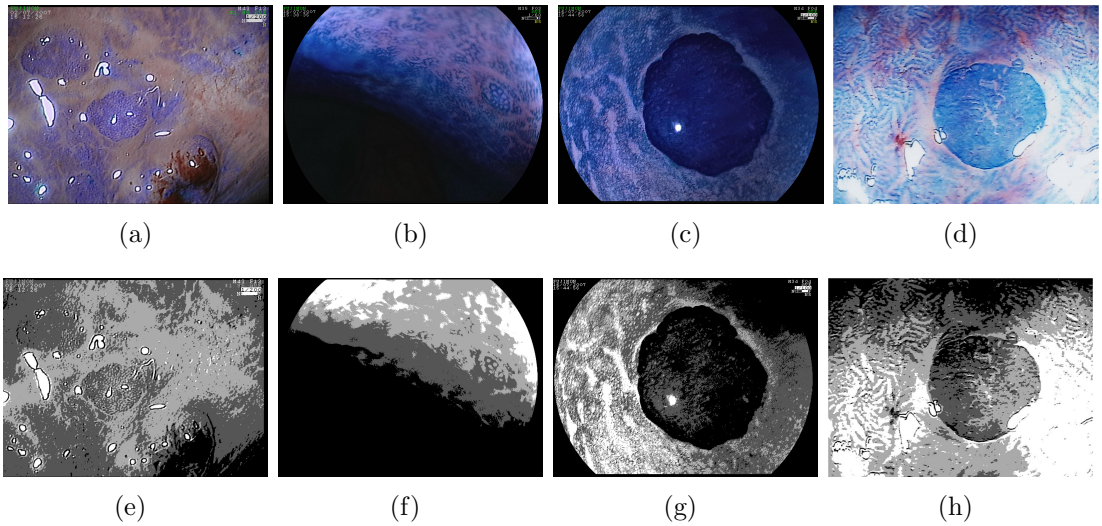

(a) (b) (c) (d)

(e) (f) (g) (h)

Fig. 5.18: Input image (first row) and iterative_threshold output (last row).

Tab. 5.10: Snake input values.

Parameters/Case	1	2	3	4	5	6
α	0,1	0,1	0,5	0,5	0,5	0,5
β	0,1	0,1	0,1	0,1	0,2	0,2
γ	0,1	0,1	0,1	1	1	1,5
κ	0,15	0,15	0,15	0,2	0,2	0,2
ω_{line}	0,1	0,1	0,1	0,1	0,3	0,5
ω_{edge}	0,1	1	1	1	1	1,5
ω_{term}	0,1	0,1	0,1	0,1	0,4	0,5
$Iterations$	100	200	200	300	300	500

step, Fig 5.21, Fig 5.22, Fig 5.23 and Fig 5.24.

When using higher values of μ the contour tends to slide through the whole image, not fixing in any contour even if there is a contour with strong edges, Fig 5.21(c) and Fig 5.24(c).

With this algorithm applied in a median filtered image, kernel size twenty-one, it was not possible to obtain the segmentation of the ACF. The ACWE detects also other contours, from other objects, that have the same pixel values or are easily mistaken with an ACF.

For this purpose hybrid_acwe was developed, it performs smoothing, remove_glare, mip and get_contour, and applies the last output as a mask for the ACWE method, this way the mask resembles the original image contours. The input of this algorithm is an untreated image. The μ was fixed in 0.1 which was the best value from the previous results with ACWE.

The results are similar, Fig 5.25, although the borders were used as mask it is not

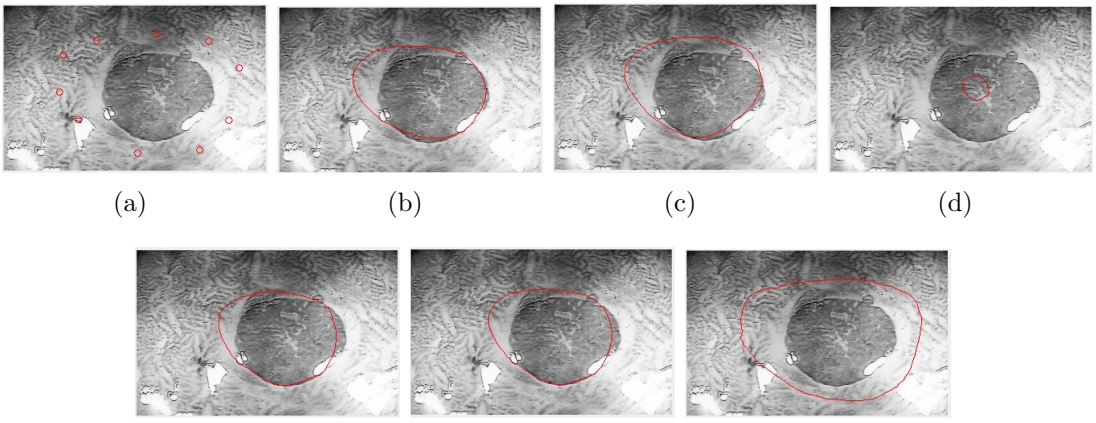

(a) (b) (c) (d)

(e) (f) (g)

Fig. 5.19: Snake initial points (a), case 1 (b), 2 (c), 3 (d), 4 (e), 5 (f) and 6 (g).

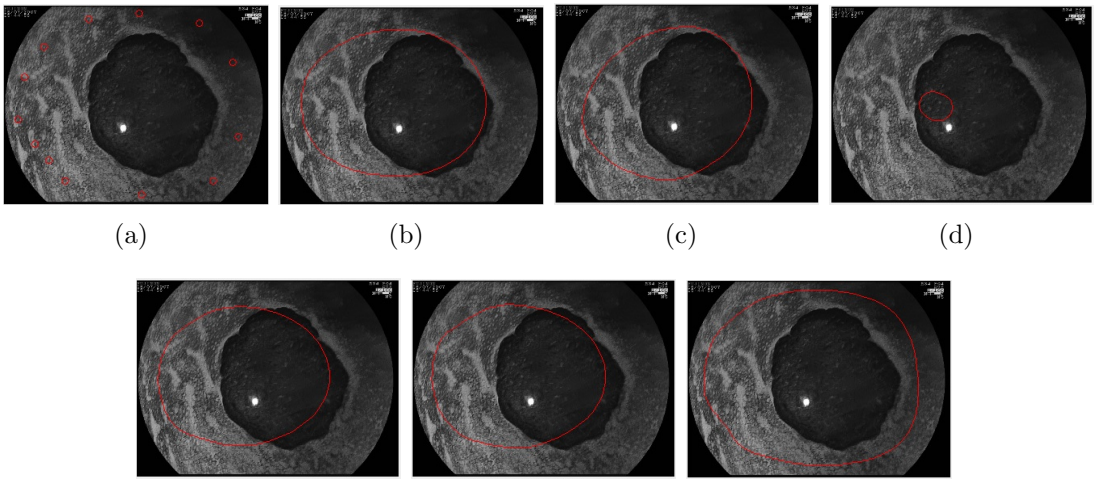

(a) (b) (c) (d)

(e) (f) (g)

Fig. 5.20: Snake initial points (a), case 1 (b), 2 (c), 3 (d), 4 (e), 5 (f) and 6 (g).

clear if they have helped the ACWE once the results are almost the same. For Fig 5.26, it is possible to see an improvement in the results in cases (c) and (d).

The hybrid_region_grow is an automatic seed placement method. Through image contours, estimated by get_contour algorithm it is possible to, also, estimate a proper position of the seed. As mencioned before, this method is useful when there is a single ACF in image. This algorithm relies on smoothing, remove_glare and get_contour outputs, Fig 5.27, Fig 5.28, Fig 5.29 and Fig 5.30.

Thie algorithm was able to position the seed directly in the ACF, except in Fig 5.29, making it a good result outset even before segmentation process steps in and grow the region surrounding the seed.

Even though the seed was detected correctly in most cases, the final output of the

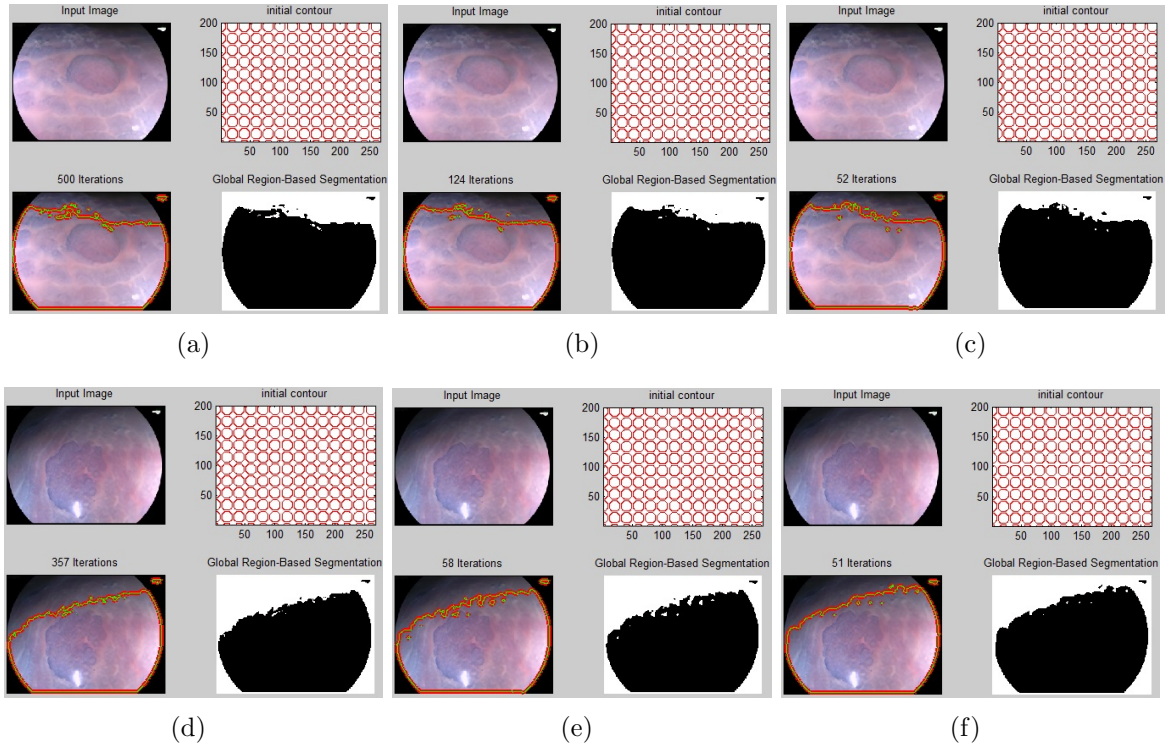

Fig. 5.21: Whole mask type: $\mu = 0.1$ (first column), $\mu = 0.3$ (second column) and $\mu = 0.5$ (third column).

hybrid_region_grow was not able to segment as many images as the expected. Also, as mentioned before, this algorithm was developed for images with only one ACF and that can be seen in Fig 5.28(b)(d) where there are two ACF and only one was detected.

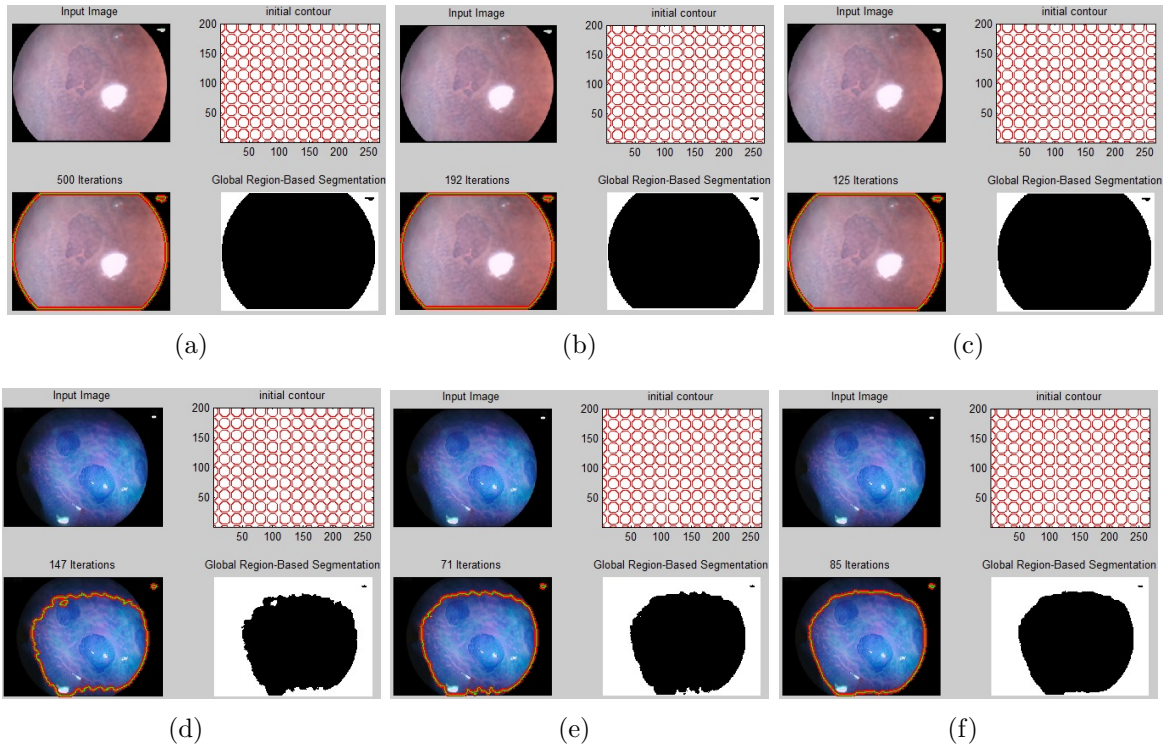

(a) (b) (c)

(d) (e) (f)

Fig. 5.22: Whole mask type: $\mu = 0.1$ (first column), $\mu = 0.3$ (second column) and $\mu = 0.5$ (third column).

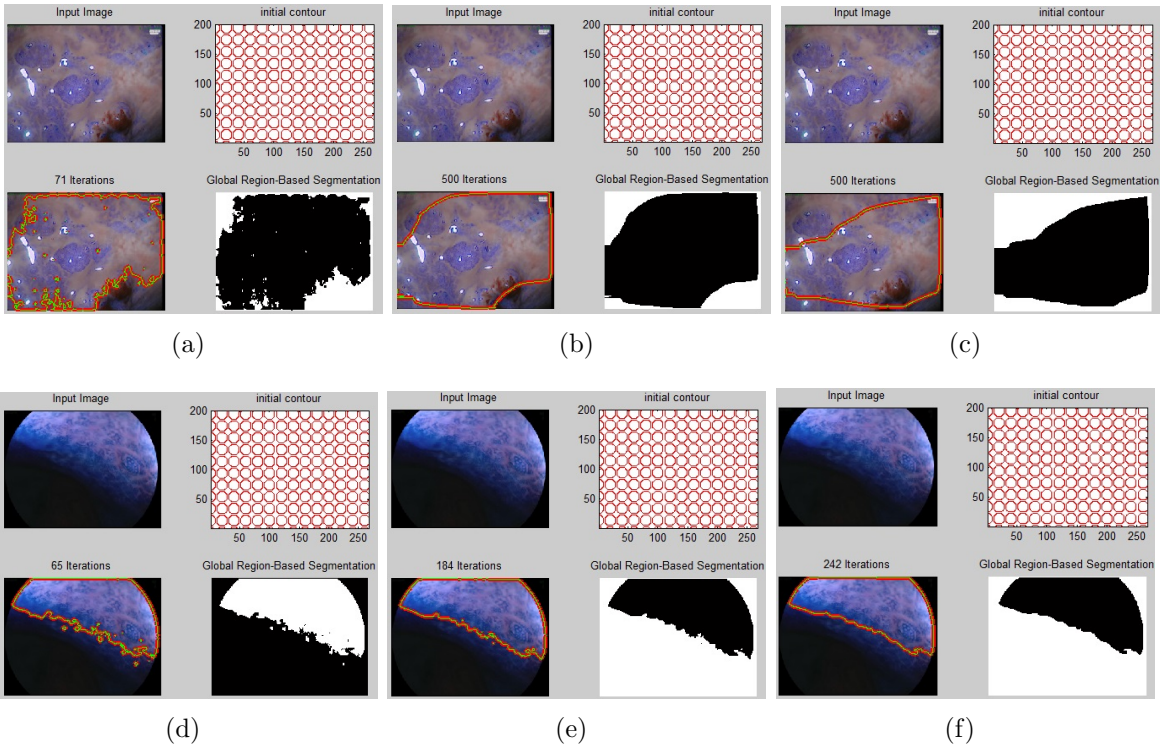

(a) (b) (c)

(d) (e) (f)

Fig. 5.23: Whole mask type: $\mu = 0.1$ (first column), $\mu = 0.3$ (second column) and $\mu = 0.5$ (third column).

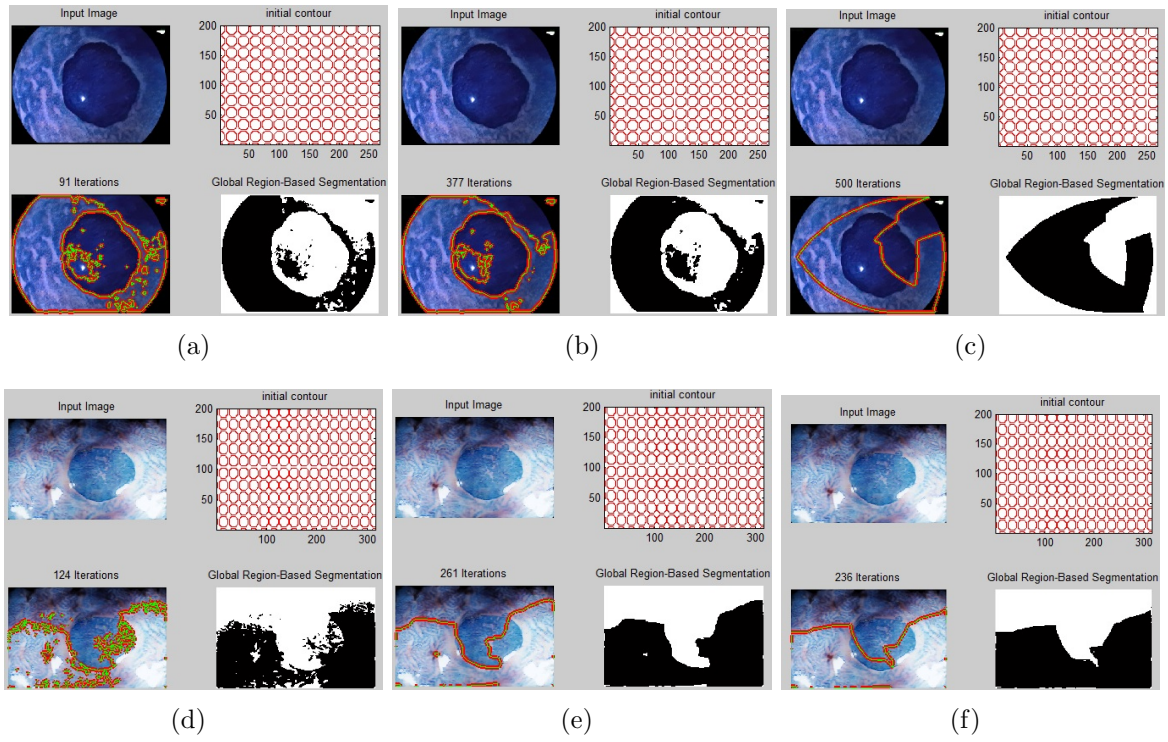

Fig. 5.24: Whole mask type: $\mu = 0.1$ (first column), $\mu = 0.3$ (second column) and $\mu = 0.5$ (third column).

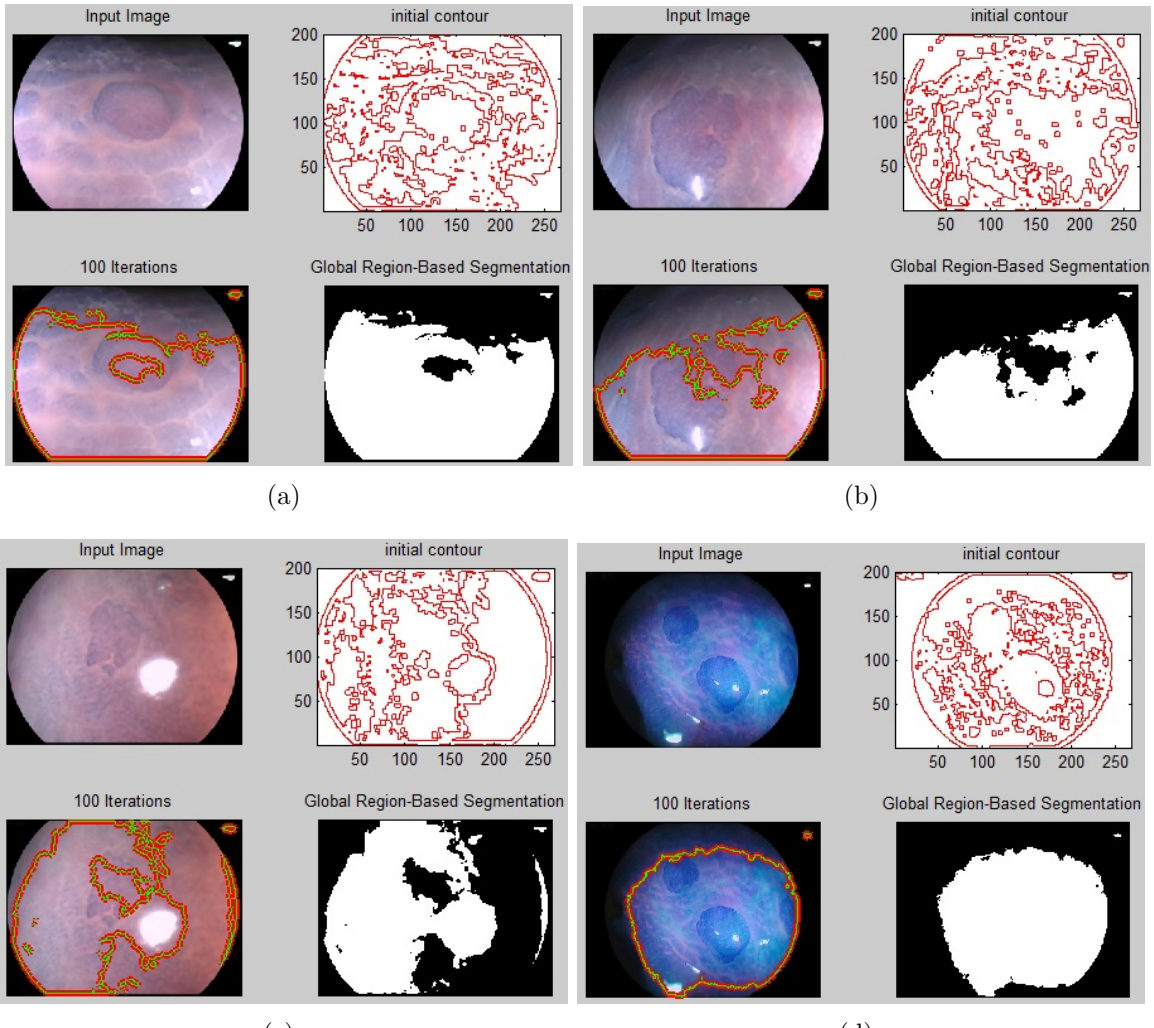

Fig. 5.25: hybrid_acwe output for different images.

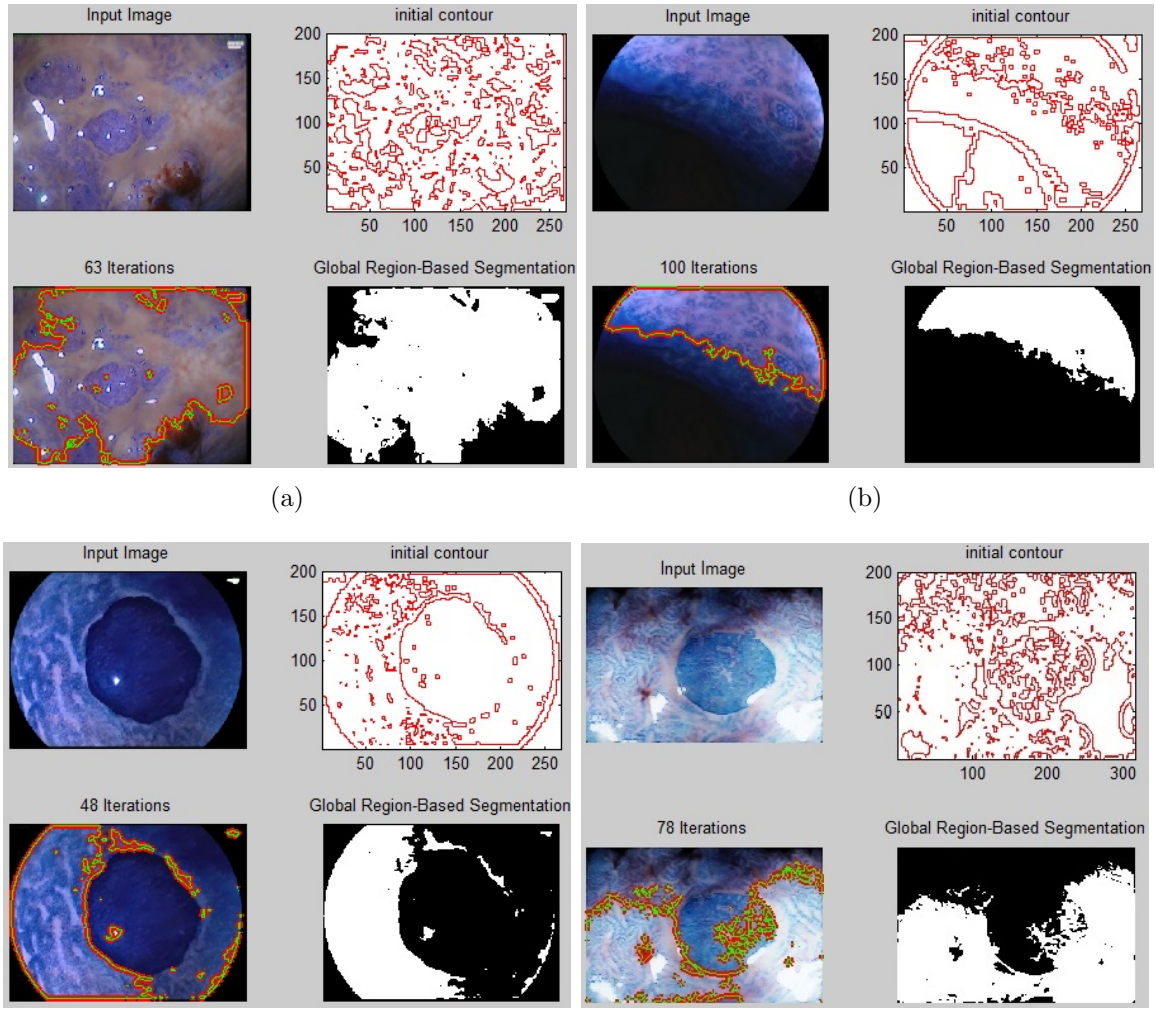

Fig. 5.26: hybrid_acwe output for different images.

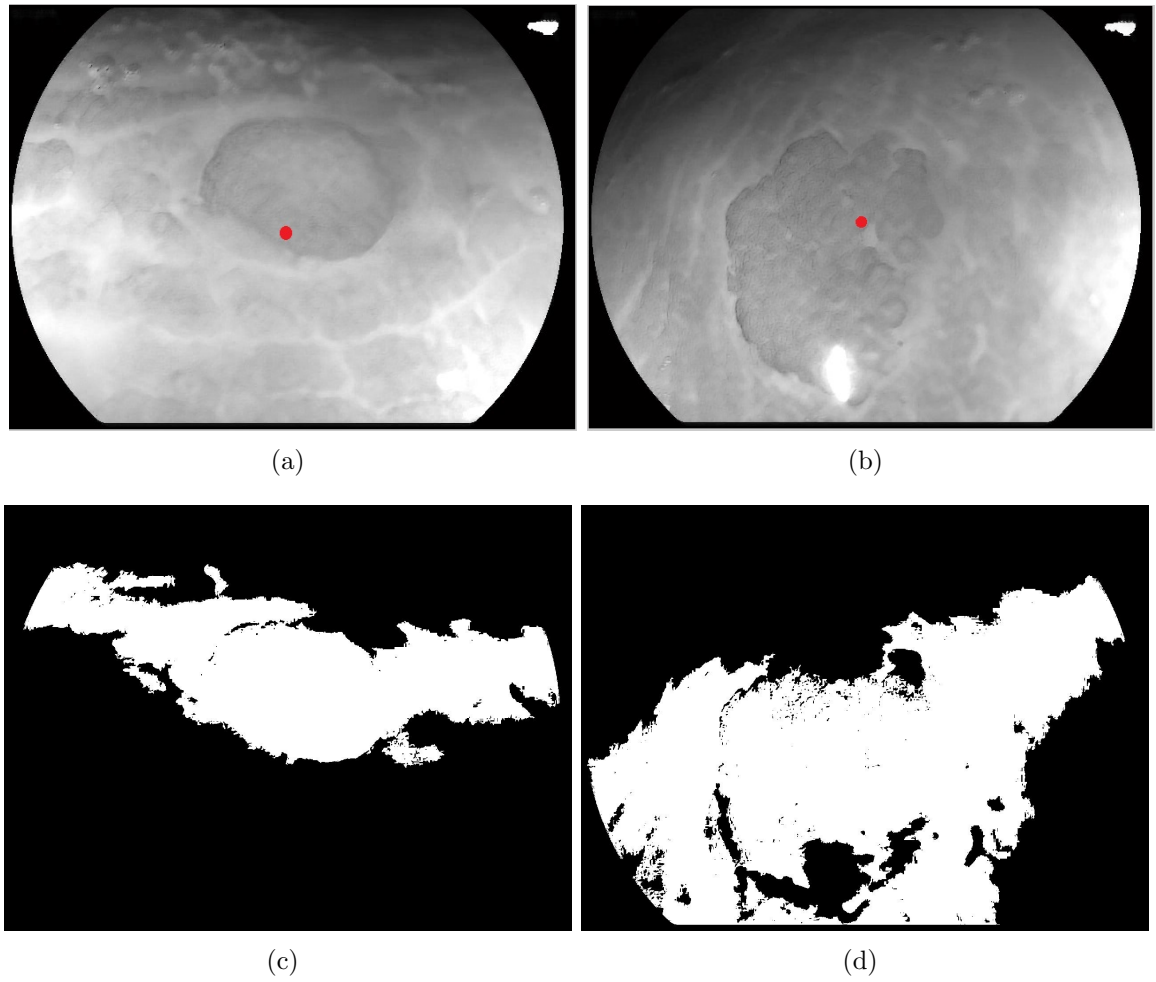

(a) (b)

(c) (d)

Fig. 5.27: Seed positioning (first row) and hybrid_region_grow output (last row).

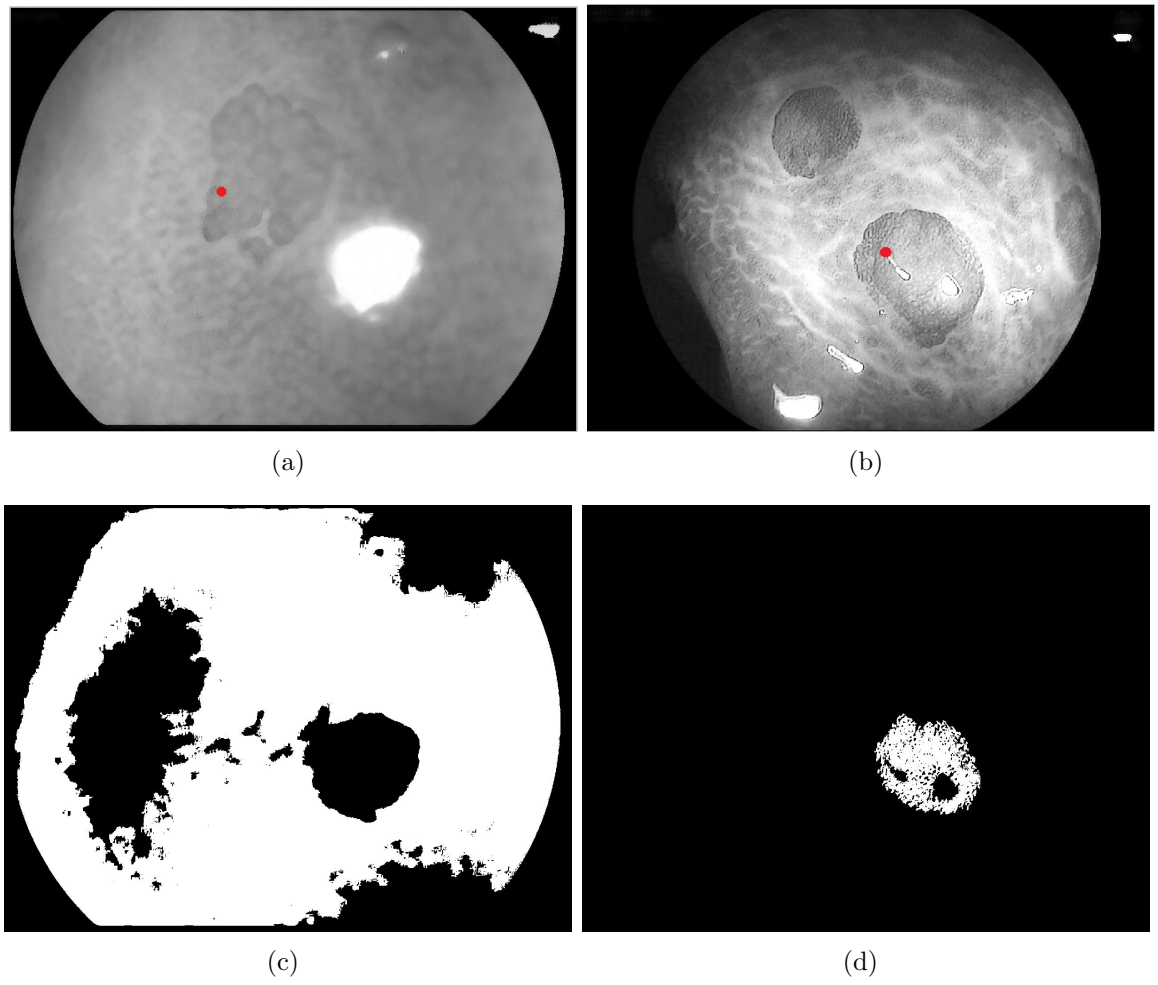

(a) (b)

(c) (d)

Fig. 5.28: Seed positioning (first row) and hybrid_region_grow output (last row).

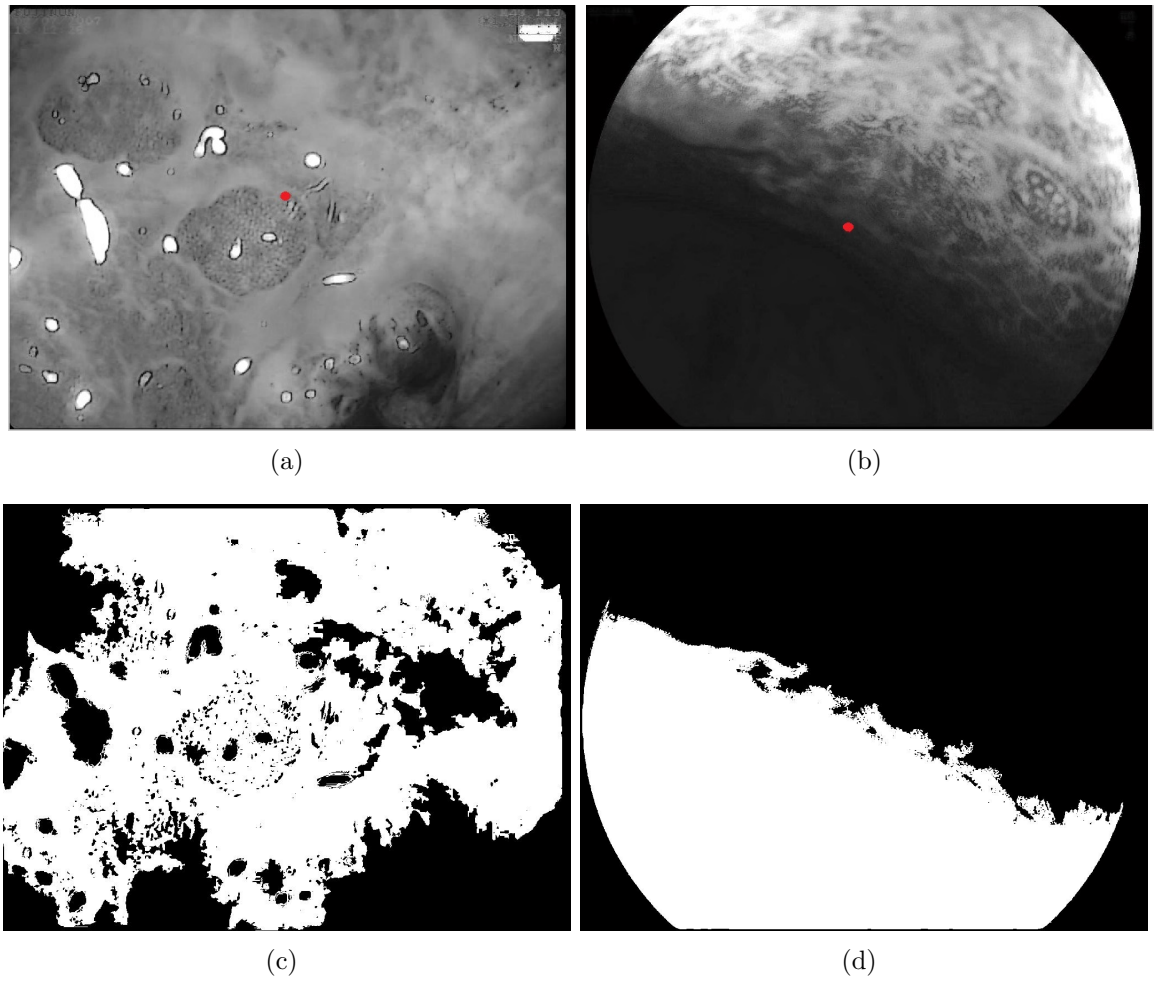

(a) (b)

(c) (d)

Fig. 5.29: Seed positioning (first row) and hybrid_region_grow output (last row).

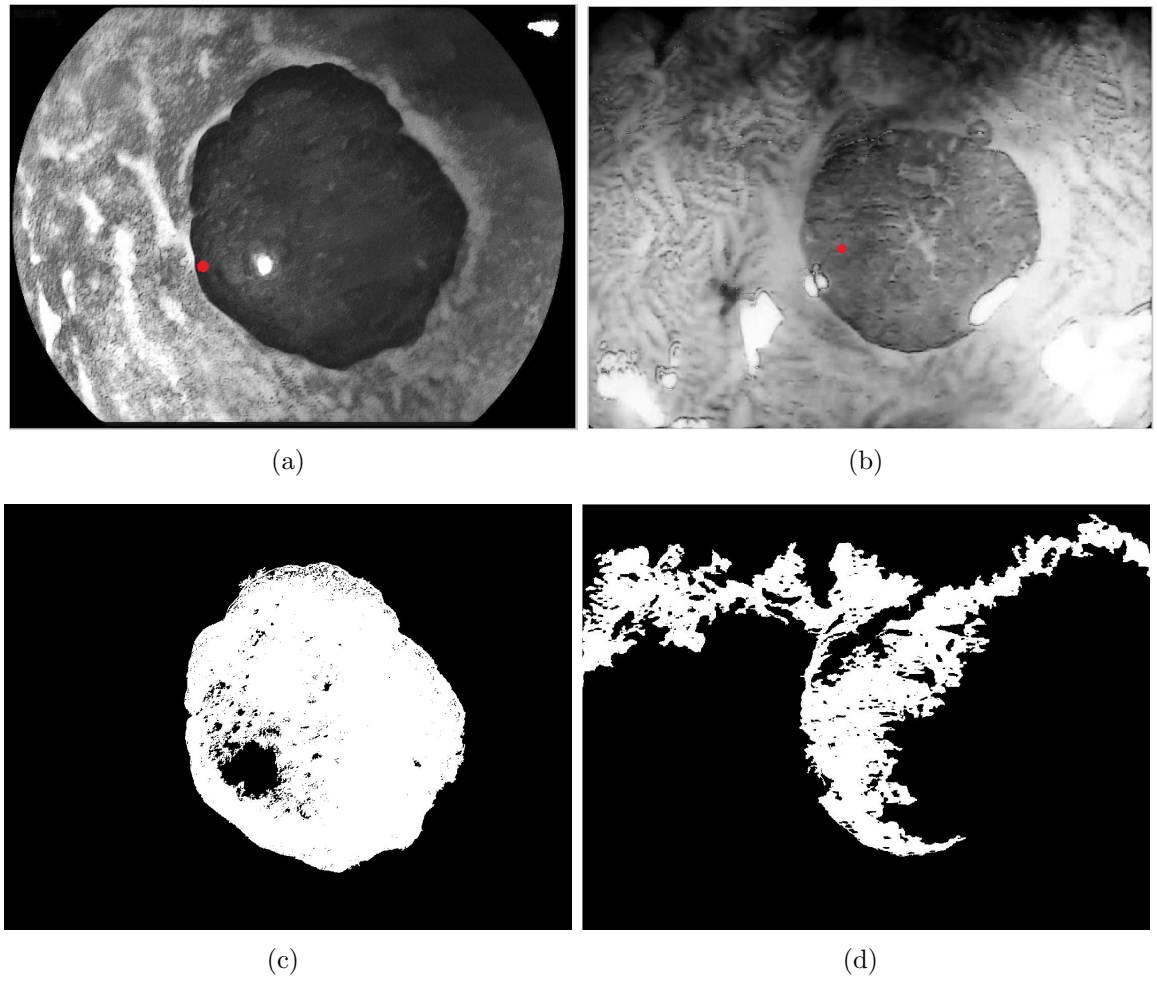

(a) (b)

(c) (d)

Fig. 5.30: Seed positioning (first row) and hybrid_region_grow output (last row).

5.5 Summary

The choice of the median filter, with kernel size twenty-one, in the preprocessing step was related to the statistics obtained. It was a good smoothing algorithm, but also it did not reflect on edge-loss. Though some of the algorithms in the segmentation phase almost did not rely on low-smoothed images. The ACWE algorithm can perform well in high smoothed images.

In feature extraction step, the get_contour results had more noise than expected, but the increase of the smoothing in previous step, could compromise image integrity further ahead. Also the glare_removal introduced more noise to the image, wich is expected since it was only a pure cosmetic result. The glare_mask could be used in future developments. The mip perfomed as expected in most case images.

Segmentation was achieved in one case with the hybrid segmentation techniques. The hybrid_region_grow has proven to be effective in detecting the ACF, when in single ACF images. Some known techniques were used, that already produced acceptable results in other thesis, the snake values were adapted from Alves (2011) and different results were obtained.

Chapter 6

Conclusions & Future Work

The early detection of colorectal cancer contributes to a higher cure chance of this high mortatily and disabling disease. Curently, there as been a growing number of research and grants in this particular area, either in laboratory techniques, biologycal, or in image analysis and detection of ACF.

The ACF is considered to be a percursor of colorectal cancer, so it is crucial the early detection of these structures in colonoscopy techniques. The aim of this dissertation was, mainly, to help this ongoing research, by developing techniques that help the segmentation of the aberrant crypt foci.

The final objective of the preprocessing step was to obtain better images, when compared to the original ones. Better in terms of noise and contrast. Smoothing algorithms were used in this phase to help following steps. The best results were achieved by stretching the histogram and then perform a medin filtering, to remove noise.

The feature extraction was developed in order to harvest image characteristics, like the areas affected by glare, caused by misuse of light. Also, since these images have color, extract a color mapping, a distribution of the predominant colors in one given pixel. This works almost as a simple segmentation technique and border detection, wich is clearly commited with the smoothing phase.

At the segmentation step, only one developed algorithm was able to detect the ACF properly. Although, some of the methods used could be enhanced to improve its ability to ACF segmentation.

The main difficulty are the different image acquisition systems, the different techniques used by medical staff and, also, the errors introduced by them and the patient own biology, even if the dye is properly absorved or not. There is no uniformization of the acquired images and this is a problem that needs to be solved in order to achieve better results.

This thesis should be considered as an introduction to ACF segmentation techniques, as it contributes to the ongoing research in this area and it could provide guide lines to

researchers and developers.

As final thoughts, image normalization is an initial critical step, as well as clinical validation of the developed algorithms. A bigger dataset of different image acquisition systems and by different clinicians will be important to develop more efficient and effective techniques.

Personally it was a great challenge, even though the ultimate goal was to segment the ACF, I have always faced it as an aid to the research beeing perfomed nowdays.

Bibliography

Adams, R. and Bischof, L. (1994). Seeded region growing. *IEEE Transactions on Pattern Analysis and Machine Intelligence*, 16(6):641–647.

Adler, D., Chand, B., Conway, J., Diehl, D., Kantsevoy, S., Kwon, R., Mamula, P., and Rodriguez, S. (2008). Capsule endoscopy of the colon. *American Society for Gastrointestinal Endoscopy*, 68(4):621–623.

Alrawi, S., Schiff, M., Carroll, R., Dayton, M., Gibbs, J., Kulavlat, M., Tan, D., Berman, K., Stoler, D., and Anderson, G. (2006). Aberrant crypt foci. *Anticancer Research*, 26:107–120.

Alves, A. (2011). Endoscopic image analysis of aberrant crypt foci. Master's thesis, Faculty of Engineering, University of Porto.

Apanasovich, T., Ruppert, D., Lupton, J., Popovic, N., Turner, N., Chapkin, R., and Carroll, R. (2007). Aberrant crypt foci and semiparametric modeling of correlated binary data. *The International Biometric Society*, 64(490-500).

Bankman, I. (2000). *Handbook of Medical Imaging*. Academic Press.

Bleau, A. and Leon, J. (2000). Watershed-based segmentation and region merging. *Computer Vision and Imagem Understanding*, 77:317–370.

Brotherstone, H., Vance, M., Edwards, R., Miles, A., Robb, K., Evans, R., Wardle, J., and Atkin, W. (2007). Uptake of population-based flexible sigmoidoscopy screening for colorectal cancer: a nurse-led feasibility study. *Journal of Medical Screening*, 14:76–80.

Brox, T. and Weickert, J. (2004). Level set based image segmentation with multiple regions. *Pattern Recognition*, pages 415–423.

Burger, W. and Burge, M. (2009). *Principles of Digital Image Processing*. Springer.

Canny, J. (1986). A computational approach to edge detection. *IEEE Transactions on Pattern Analysis and Machine Intelligence*, 6(679-698).

Cash, B., Riddle, M., Bhattacharya, I., Barlow, D., Jensen, D., del Pino, N., and Pickhardt, P. (2011). Ct colonography of a medicare-aged population: Outcomes observed in an analysis of more than 1400 patients. *American Journal of Roentgenology*, 199:1–8.

Chan, T. and Vese, L. (2001). Active contours without edges. *IEEE Transactions on Image Processing*, 10(2):266–277.

Cohen, R. (2010). The chan-vese algorithm. Technical report, Israel Institute of Technology.

Colditz, G., Atwood, K., Emmons, K., Willett, W., Trichopoulos, D., and Hunter, D. (2000). Harvard report on cancer prevention. *Cancer Causes and Control*, 11:477–488.

Couceiro, L., Alves, I., and Almendra, R. (2009). Doenças oncológicas em portugal. Alto Comissariado da Saúde.

Emura, F., Saito, Y., Taniguchi, M., Fujii, T., Tagawa, K., and Yamakado, M. (2007). Further validation of magnifying chromocolonoscopy for differentiating colorectal neoplastic polyps in a health screening center. *Journal of Gastroenterology and Hepatology*, 22:1722–1727.

Fernandez-Urien, I., Carretero, C., Borda, A., and Muñoz-Navas, M. (2008). Colon capsule endoscopy. *World Journal of Gastroenterology*, 14(34):5265–5268.

Figueiredo, Isabel, F. P. and Almeida, N. (2011). Image-driven parameter estimation in absorption-diffusion models of chromoscopy. *SIAM Journal of Imaging Sciences*, 4(3):884–904.

Figueiredo, I., Figueiredo, P., Leal, C., and Urbano, J. (2008). A mathematical model for a comprehensive approach to the dynamics of human colonic aberrant crypt foci.

Figueiredo, I., Figueiredo, P., Stadler, G., Ghattas, O., and Araújo, A. (2010). Variational image segmentation for endoscopic human colonic aberrant crypt foci. *IEEE Transactions on Medical Imaging*, 29(4):998–1011.

Figueiredo, I., Leal, C., Romanazzi, G., Engquist, B., and Figueiredo, P. (2011a). A convection-diffusion-shape model for aberrant colonic crypt morphogenesis. *Computational Visual Science*, 14:157–166.

Figueiredo, I., Leal, C., Romanazzi, G., Figueiredo, P., and Donato, M. (2011b). A coupled convection-diffusion level set model for tracking epithelial cells in colonic crypts. *Procedia Computer Science*, 1(955-963).

Figueiredo, I., Prasath, S., Tsai, Y.-H., and Figueiredo, P. (2009). Automatic detection and segmentation of colonic polyps in wireless capsule images. Technical report, Department of Mathematics at University of Coimbra, Department of Mathematics at University of Texas and Faculty of Medicine at University of Coimbra.

Gonzalez, R. and Woods, R. (2002). *Digital Image Processing*, chapter Prentice Hall. 2.

Gonzalez, R., Woods, R., and Eddins, S. (2004). *Digital Image Processing using Matlab*. Prentice Hall.

Gouveia, J., Coleman, M., Haward, R., Zanetti, R., Hakama, M., Borras, J., Primic-Zakelj, M., Koning, H., and Travado, L. (2008). Improving cancer control in the european union: Conclusions from the lisbon round-table under the portuguese eu presidency. *European Journal of Cancer*, 44:1457–1462.

Gregorio, C., Losi, L., Fante, R., Modica, S., Ghidoni, M., Pedroni, M., Tamassia, M., Gafa, L., de Leon, M. P., and Roncucci, L. (1997). Histology of aberrant crypt foci in the human colon. *Histopathology*, 30:328–334.

Gupta, A., Pretlow, T., and Schoen, R. (2007). Aberrant crypt foci: What we know and what we need to know. *Clinical Gastroenterology and Hepatology*, 5:526–533.

Guyton, A. and Hall, J. (2000). *Textbook of Medical Physiology*, chapter 12, pages 751–808. Saunders, 12 edition.

Hamilton, S. and Aaltonen, L. (2000). Pathology and genetics of tumours of the digestive system. Technical report, International Agency for Research on Cancer.

Haris, K., Efstratiadis, S., Maglaveras, N., and Katsaggelos, A. (1998). Hybrid image segmentation using watersheds and fast region merging. *IEEE Transactions on Imagem Processing*, 7(12):1684–1699.

Hojjatoleslami, S. A. and Kittler, J. (1998). Region growing: A new approach. *IEEE Transactions on Image Processing*, 7(7):1079–1084.

Iobagiu, S., Ciobanu, L., and Pascu, O. (2007). Colon capsule endoscopy: a new method of investigating the large bowel. *Journal of Gastrointestinal and Liver Diseases*, 17:347–352.

Kass, M., Witkin, A., and Terzopoulos, D. (1988). Snakes: Active contour models. *International Journal of Computer Vision*, 1:321–331.

Kato, S., Fu, K., Sano, Y., Fujii, T., Saito, Y., Matsuda, T., Koba, I., Yoshida, S., and Fujimori, T. (2006). Magnifying colonoscopy as a non-biopsy technique for differential diagnosis of non-neoplastic and neoplastic lesions. *World Journal of Gastroenterology*, 12(9):1416–1420.

Kida, M., Kobayashu, K., and Sigenji, K. (2003). Routine chromoendoscopy for gastrointestinal diseases: Indications revised. *Endoscopy*, 35(7):590–596.

Kukitsu, T., Takayama, T., and Miyanishi, K. (2008). Aberrant crypt foci as precursors of the dysplasia-carcinoma sequence in patients with ulcerative colitis. *Clinical Cancer Research*, 14:48–54.

Li, B. and Meng, M. (2011). Contourlet-based features for computerized tumor detection in capsule endoscopy images. *Annals of Biomedical Engineering*, 39(12):2891–2899.

Li, C., Xu, C., Gui, C., and Fox, M. (2010). Distance regularized level set evolution and its application to image segmentation. *IEEE Transactions on Image Processing*, 19(12):3243–3254.

Lima, S. (2008). Estudo de algoritmos para detectar pólipos em vídeo de endo-cápsula. Master's thesis, Universidade de Aveiro.

Maillard, P., Flaction, L., Samur, E., Hellier, D., Passenger, J., and Bleuler, H. (2008). Instrumentation of a clinical colonoscope for surgical simulation. In *30th Annual International IEEE EMBS Conference*.

Makinen, M. (2007). Colorectal serrated adenocarcinoma. *Histopathology*, 50:131–150.

Maria, M. (2009). Metodologia de rastreio do cancro do cólon e recto. Master's thesis, Faculdade de Medicina da Universidade de Coimbra.

McGinley, J., Thompson, M., and Thompson, H. (2010). A method for serial tissue processing and parallel analysis of aberrant crypt morphology, mucin depletion, and beta-catenin staining in an experimental model of colon carcinogenesis. *Biological Procedures Online*, 12(118-130).

Otori, K., Sugiyama, K., and Hasebe, T. (1995). Emergence of adenomatous aberrant crypt foci (acf) from hyperplastic acf with concomitant increase in cell proliferation. *Cancer Research*, 55:4743–4746.

Otsu, N. (1979). A threshold slection method from gray-level histograms. *IEEE Transactions on Systems, Man, and Cybernetics*, 9(1):62–66.

Perona, P. and Malik, J. (1990). Scale-space and edge detection using anisotropic diffusion. *IEEE Transactions on Pattern Analysis and Machine Intelligence*, 12(7):629–639.

Pickhardt, P., Taylor, A., and Gopal, D. (2006). Surface visualization at 3d endoluminal ct colonography: Degree of coverage and implications for polyp detection. *Gastroenterology*, 130:1582–1587.

Pinto, C., Paquete, A., and Pissarra, I. (2010). Colorectal cancer in portugal. *The European Journal of Health Economics*, 10(1):65–73.

Pinto, G. R. (2010). Carcinoma colo-rectal: diagnóstico e tratamento. Master's thesis, Faculdade de Medicina da Universidade do Porto.

Pratt, W. (2007). *Digital Imagem Processing*. Wiley, 4 edition.

Pretlow, T. and Pretlow, T. (2005). Mutant kras in aberrant crypt foci (acf): Initiation of colorectal cancer. *Biochimica et Biophysica Acta*, 1756:83–96.

Riaz, F., Ribeiro, M., and Coimbra, M. (2006). A review of current computer aided diagnosis systems for polyp detection in virtual colonoscopy. Technical report, Faculdade de Ciências da Universidade do Porto, Faculdade de Medicina do Porto and Instituto Português de Oncologia.

Riaz, F., Vilariño, F., Ribeiro, M., and Coimbra, M. (2011). Identifying potentially cancerous tissues in chromoendoscopy images. In *Iberian Conference on Pattern Recognition and Image Analysis*. Iberian Conference on Pattern Recognition and Image Analysis.

Rodriguez, L., Rodriguez, B., and Vilchis, J. (2007). Focos de criptas aberrantes. *Endoscopia*, 19:116–119.

Roncucci, L., Modica, S., Pedroni, M., Tamassia, M., Ghidoni, M., Losi, L., Fante, R., Gregorio, C., Manenti, A., Gafa, L., and de Leon, M. P. (1997). Aberrant crypt foci in patients with colorectal cancer. *British Journal of Caner*, 77(23):2343–2348.

Rubesin, S., Levine, M., Laufer, I., and Herlinger, H. (2000). Double-contrast barium enema examination technique. *Radiology*, 215:642–650.

Sá, P. M. G. (2008). Cancro do cólon e recto. Master's thesis, Faculdade de Ciências da Saúde, Universidade da Beira Interior.

Seeley, R., Stephens, T., and Tate, P. (2004). *Anatomy Physiology*, chapter 24, pages 860–896. MGraw-Hill, 6 edition.

Sethian, J. A. (1996). Level set method: An act of violence. Technical report, University of Berkley.

Shpitz, B., Klwin, E., Buklan, G., Neufeld, D., Nissan, A., Freund, H., Grankin, M., and Bernheim, J. (2003). Suppressive effect of aspirin on aberrant crypt foci in patient with colorectal cancer. *Journal of Gastroenterology and Hepatology*, 52:1598–1601.

Song, L., Adler, D., Chand, B., Conway, J., Croffie, J., DiSario, J., and Mishkin, D. (2007). Chromoendoscopy. *American Society for Gastrointestinal Endoscopy*, 66(4):639–649.

Suetens, P. (2009). *Fundamentals of Medical Imaging*. Cambridge University Press, 2 edition.

Suri, J., Wilson, D., and Laxminarayan, S. (2005). *Handbook of Biomedical Image Analysis - Segmentation Models*, volume 1. Kluwer Academic.

Takayama, T., Katsuki, S., Takahashi, Y., Ohi, M., Nojiri, S., Sakamaki, S., Kato, J., Kogawa, K., Miyake, H., and Niitsu, Y. (1998). Aberrant crypt foci of the colon as percursors of adenoma and cancer. *The New England Journal of Medicine*, 339(18):1277–1284.

Taylor, S., Halligan, S., Saunders, B., Bassett, P., Vance, M., and Bartram, C. (2003). Acceptance by patients of multidetector ct colonography compared with barium enema examination, flexible sigmoidoscopy and colonoscopy. *American Journal of Roentgenology*, 181:913–921.

Thorup, I. (1996). *Aberrant crypt foci in the colo-rectal mucosa as reliable markers of tumor development*. PhD thesis, Institute of Toxicology, Department of General Toxicology,.

Tiilikainen, N. (2007). A comparative study of active contour snakes. Master's thesis, Copenhagen University.

Tortora, G. and Derrickson, B. (2009). *Principles of Anatomy and Physiology*, chapter 24, pages 921–968. John Wiley and Sons, Inc, 12 edition.

Tsai, D.-M. (1995). A fast thresholding selection procedure for multimodal and unimodal histograms. *Pattern Recognition Letters*, 16:653–666.

Vese, L. and Chan, T. (2002). A multiphase level set framework for image segmentation using the mumford and shah model. *International Journal of Computer Vision*, 50(3):271–293.

Vilariño, F., Spyridonos, P., DeIorio, F., Vitrià, J., Azpiroz, F., and Radeva, P. (2010). Intestinal motility assessment with video capsule endoscopy: Automatic annotation of phasic intestinal contractions. *IEEE Transactions on Medical Imaging*, 29(2):246–259.

Wargovich, M., Brown, V., and Morris, J. (2010). Aberrant crypt foci: The case for inclusion as a biomarker for colon cancer. *Cancers - Biomarkers: Oncology Studies*, 2:1705–1716.

Weeratunga, S. and Kamath, C. (2004). An in vestigation of implicit active contours for scientific image segmentation. In *Visual Communications and Image Processing Conference*. IST/SPIE Symposium Electronic Imaging.